Investigations on the lubrication mechanism of surface-attached hydrogels

Maryam Bahrami

UNIVERSITÉ DE STRASBOURG

ÉCOLE DOCTORALE Physique et Chimie-Physique

Institut Charles Sadron (CNRS UPR22)

THÈSE EN COTUTELLE présentée par :

Maryam BAHRAMI

soutenue le 10 Juillet 2020

pour obtenir le grade de **Docteur de l'université de Strasbourg**

&

Docteur de l'université de Freiburg

Discipline/Spécialité : Mécanique des Matériaux

Investigations on the lubrication mechanism of surface-attached hydrogels

THÈSE dirigée par :

M. LE HOUEROU Vincent	Professeur, Université de Strasbourg
M. RÜHE Jürgen	Professeur, University of Freiburg

RAPPORTEURS :

Mme. CAYER-BARRIOZ Juliette	Directrice de Recherche, Ecole Centrale de Lyon
M. EBERL Chris	Professeur, Fraunhofer IWM

Investigations on the lubrication mechanism of surface-attached hydrogels

Dissertation

zur Erlangung des Doktorgrades
der Technischen Fakultät
der Albert-Ludwigs Universität Freiburg im Breisgau

vorgelegt von

Maryam Bahrami

(M.Sc.)

Freiburg im Breisgau, 2020

This research was carried out between December 2015 and November 2019 under the joint supervision of Prof. Dr. Jürgen Rühe in the group of Chemistry and Physics of Interfaces from the University of Freiburg and Prof. Dr. Vincent Le Houérou from the Tribology of Polymers group in Institute Charles Sadron (ICS) from the University of Strasbourg, France.

Dean: Prof. Dr. Rolf Backofen

Examination Committee:

First referee: Prof. Dr. Jürgen Rühe

Second referee: Prof. Dr. Vincent Le Houérou

Examiner: Dr. Juliette Cayer-Barrioz

Chair: Prof. Dr. Chris Eberl

Date of Defense: 10.7.2020

Contents

List of Abbreviations

AFM	Atomic force microscope
CHic	C-H insertion crosslinking
COF	Coefficient of friction
DMT	Derjaguin-Muller-Toporov theory [1]
EHL	Elastohydrodynamic
JKR	Johnson-Kendall-Roberts theory [2]
MABP	4-methacryloyloxy benzophenone
PDMAA-co-MABP	Poly(dimethyl acrylamide-co–methacryloyl oxybenzophenone)
PE	Poroelastic
PVE	Poroviscoelastic
PVP	Polyvinylpyrrolidone
SFA	Surface force apparatus
WLF	Williams-Landel-Ferry theory [3]

List of Symbols

a	Contact radius
a_{12}	Shift from state 1 to 2
a_p	Shift factor
A	Fit parameter
b	Kuhn length
B	Empirical constant
C_∞	Characteristic ratio
D	Distance
E	Elastic modulus
E_{eff}	Contact modulus or effective elastic modulus
f	Friction coefficient between polymer chains and water
f_0	Free volume at pressure P_0
f_1	Free volume in state 1
f_2	Free volume in state 2
f_p	Free volume at pressure P
F_A	Adhesion
F_d	Deformation force
F_D	Drag force
F_{ext}	Chain stretching force
F_f	Friction force
$F_{lateral}$	Lateral force
F_N	Normal force
F_{po}	Pull-off force
F_p	Polymer deformation force
g	Correction function
G	Shear modulus
h_1	Initial thickness in dry state

h_2	Thickness in swollen state
H	Hamaker constant
k	Permeability
k_B	Boltzmann's constant
K	Hydraulic conductivity
l	End to end vector
l_{max}	End to end vector at a fully stretched chain
n	Deformation index
N	Number of monomers
N_c	Number of segments between crosslinks
p	Pressure
Pe	Force characteristic ratio
p_{max}	Maximum pressure
R	Radius
S	Volumetric swelling
S_{sa}	Volumetric swelling factor of surface-attached networks
S_{uc}	Swelling factor of unconstrained network
T	Temperature
v	Velocity
v^*	Transition speed
V	Volume
$V_{lateral}$	Lateral voltage
W	Half width of friction loop
W_A	Work of adhesion
X	Geometric factor
Z_0	Equilibrium distance according to LJ potential
α	Calibration factor
α_s	Linear elongation or swelling factor
α_{sa}	Linear elongation of surface-attached network
α_{uc}	Unconstrained linear elongation
β	Compressibility
δ	Penetration depth

δ_{max}	Maximum penetration depth
δ_r	Relaxation depth
$\dot{\delta}$	Compression rate
Δ	Offset of the friction loop
ε	Strain
η	Viscosity
μ	Coefficient of friction
μ_{tb}	Tabor parameter
ν	Poisson's ratio
ξ	Polymer mesh size
σ	Stress
τ	Relaxation time
φ	Volume fraction
φ_0	Volume fraction of unswollen polymer occupied in the prepared state.
ϑ	Bond angle

1 Introduction

1.1 Friction in nature

Natural systems have frequently served as a model for the development of technical systems mainly because of their high efficiency, durability, and their ability to adapt themselves to new environmental situations [4–6]. Investigations on biological systems span from understanding the structure and properties to the modeling of such systems with the purpose of developing bio-mimetic and bio-inspired systems. A remarkable number of studies have been conducted to understand the architecture, properties, and mechanisms of the interactions of natural systems in mechanical contact with each other. This question is essential for all movements of biological systems. In most cases, locomotion should require as little energy dissipation as possible and accordingly, the evolutionary process has led to specialized surfaces with reduced friction to avoid wear and minimize energy loss. On the other hand, sometimes increased friction is desired to improve attachment and grip or controlled friction to realize either attachment or detachment, depending on the situation [4]. A few examples in nature, where friction is adjusted to meet the requirement of the living organism for different purposes, are insect feet [7], plant leaves [7,8], gecko feet [9], snakeskin [6,10], and synovial joint of mammals [11]. Increased friction by surface structures to facilitate attachment can be found, for example, in Gecko [4,9,12]. For Gecko at times a strong adhesion to the ground they walk on is highly desired, especially visible when they move on a vertical wall. In contrast, structures on the sharkskin can reduce friction and drag of a shark moving through the water, and this way enhances the efficiency of locomotion [5,10,13]. Furthermore, many fish can produce skin secrets, which are water-soluble, to damp the turbulence and reduce friction. As explained in all the previous examples, friction is controlled through surfaces with specialized topography and chemistry [14]. The complexity of these surfaces and the ability to regenerate themselves make mimicking their behavior quite challenging.

Friction is an energy dissipative process. The origin of energy dissipation can be classified into two categories. One category is related to energy dissipation as a function of chemical interactions where molecular non-covalent interactions need to be broken when two objects slide against each other. In the other case, energy dissipation is due to the breakage of

permanent chemical bonds, which results in resistance into motion leading to plowing, deformation, heat, etc. [15].

Two surfaces can interact through different mechanisms, which leads to resistance against the separation of two surfaces and high adhesion or friction. The different mechanisms are depicted in Figure 1-1. Van der Waals interaction, which occurs as an attraction between atoms, molecules, or surfaces through permanent or induced dipoles (Figure 1-1a), is one of the very common mechanisms. Attachment of some of the insects, such as spiders, mainly relies on the van der Waals interaction [4,6]. Another mechanism through which two surfaces can interact is through the establishment of chemical bonds between the surfaces (Figure 1-1b), which leads to stronger adhesion than the van der Waals forces, as atoms of two materials share or exchange electrons. For instance, mussels can stick to rocks by forming chemical bonds [16]. When the surfaces are wet, in the presence of a thin liquid film, capillary forces appear (Figure 1-1c). However, if the interacting surfaces are fully immersed in liquid, there is no capillary interaction. Capillary forces are used for water uptake of plants and small animals. Mechanical interlocking (Figure 1-1d) is another mechanism to keep two surfaces together [4,6,17]. When interlocking occurs, the separation of the surfaces requires deformation of the surfaces. This mechanism is, for example, used in the wing locking system of beetles. Suction (Figure 1-1e), which is a self- explanatory mechanism, is a method used by Clingfish to stick to smooth and rough surfaces [18,19]. Interdiffusion polymers is an example of diffusion where the polymers can generate a permanent and strong bond (Figure 1-1f). Separation of deeply interdiffused surfaces requires very high energy and breakage of covalent bonds. Electrostatic and magnetic interactions are not among the common interactions (Figure 1-1g-h) [4], as for such interactions, special requirements have to be met. For electrostatic interactions, strongly charged surfaces are required, and for magnetic interactions, two magnetic dipoles are needed. Both electrostatic and magnetic interactions are well known and widely used in robotics.

Among all the introduced interactions, energy dissipation of vdW, capillary, suction, magnetic, and electrostatic interactions are in the category of interactions where breakage of non-permanent bonds are required, and all the rest are in the category where breakage of permanent bonds are necessary. Adjusting interactions can help engineers to customize surfaces according to their need for high or low friction surfaces.

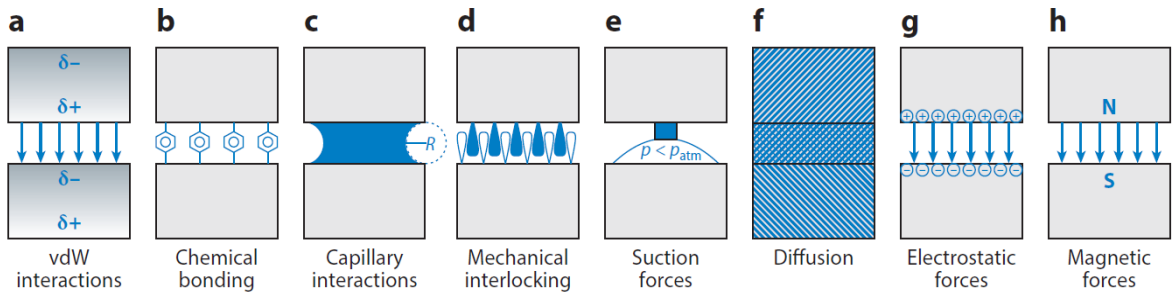

Figure 1-1 Types of interactions that can occur between two surfaces in contact with each other [4,6].

1.1.1 High friction surfaces in nature

Animals in nature, such as insects, spiders, and lizards, are capable of having fast locomotion and strong adhesion. The occurrence of strong adhesion and fast locomotion in one system leads to apparently contradictory requirements of the contacting surfaces [10,20]. As an example, in Gecko feet, van der Waals forces result in strong adhesion, however, such a strong interaction force is not desirable once locomotion and detachment are required. Additionally, these surfaces must meet the requirement for self-cleaning in order to maintain their functionality [20]. Animals can attach to surfaces by means of three different mechanisms: (1) mechanical interlocking of rough surfaces, (2) soft smooth adhesion by meniscus or increased contact area, and (3) adhesion through hairy structures as a result of van der Waals forces [12,20,21]. Most of the animals have two of these attachment mechanisms to ensure sufficient adhesion. For instance, bees with claw and smooth pad or geckos with claw and setae pad [12]. Attachment pads of a beetle, fly, spider, and gecko are shown in Figure 1-2 [22]. The relation between the animal size and the feature size in their attachment pads is shown in Figure 1-2. As can be seen, the size of hairy structures in the attachment pads becomes smaller, and the number of structures increases as the animal becomes larger [22]. Among all creatures that have the ability to stick to vertical or even overhanging surfaces or ceilings, geckos have the biggest size, and therefore they have drawn the attention of many researchers [10,20,22]. Geckos are able to create high frictional forces and strong adhesion with surfaces as a result of the hierarchical structures on their toes, even on upright walls or the ceiling of buildings [5]. Gecko attachment and detachment from any surface realizes through the hierarchical structure of their skin comprising of lamella, setae, and spatula [5,22]. Every seta of geck's toes consists of hundreds of spatula. The van der Waals forces between these fine structures and the surface can result in high adhesion and friction between the gecko feet and the surface.

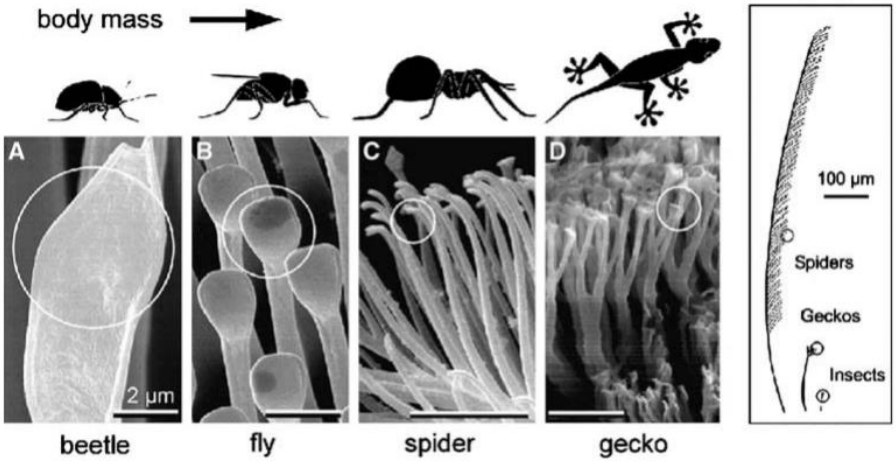

Figure 1-2 Attachment pads of a beetle, fly, spider, and gecko; showing the direct relation between the animal size, the structure size, and the number of structures on the attachment pads [22].

Although high friction is sometimes targeted, in most cases, the main challenge is to achieve sufficient friction reduction either by minimizing the contact area or by application of a lubricant.

1.1.2 Biolubrication

Nature provides solutions to wear and high friction by introducing surface roughness and/or water-based lubricants [5,23,24]. Snakeskin exemplifies surfaces where surface patterns maintain the optimization of friction [25]. To generate propulsion during locomotion, high friction is required, while to slide along the substrate, low friction must be generated. Thus, to facilitate effective locomotion, the ventral body has anisotropic frictional properties, which originates from structures of different scales [26].

Water serves as an excellent lubricant in nature as it has low viscosity and can be easily sheared. However, it has weak load-bearing capacity at high pressures [24]. At high loads, it squeezes out from the gap resulting in direct contact between the two surfaces and thus higher friction. The lubrication properties of water are thus usually improved in nature through the addition of components such as mucins, aggrecans, and polysaccharides [27]. These components increase the load-bearing capacity of water by steric and electrostatic repulsion or through rendering the viscosity of the lubricant anisotropic so that in the direction of the load, the viscosity is high while it is low in the shearing direction. Such a behavior is due to a (shear-

induced) liquid crystalline orientation of the lubricant molecules in the friction gap. Moreover, they reduce friction through adsorbing to the surface. The foot mucus secretion of snails, which contains water and 3-4 percent glycoprotein, is one of those examples where water serves as a lubricant [28]. A similar mechanism provides the ability to achieve low friction and significant load-bearing capacity in aqueous media in human joints.

Synovial joints are one of the most attractive lubricated systems in nature that has been vastly investigated by researchers [5,14,24,29,30]. Synovial joints provide astonishing lubrication properties and longtime durability lasting the human lifespan and undergoing millions of loading cycles. The loading conditions in synovial joints change from stationary to migrating contact, depending on the type of activity [14]. Despite the different loading conditions during different activities, healthy synovial joints represent a very low coefficient of friction in the range of 0.001 to 0.01 [23]. Pressure in these joints can reach a value of 5-6 MPa and a maximum value of 18 MPa in the hip joint during descending the stairs [24].

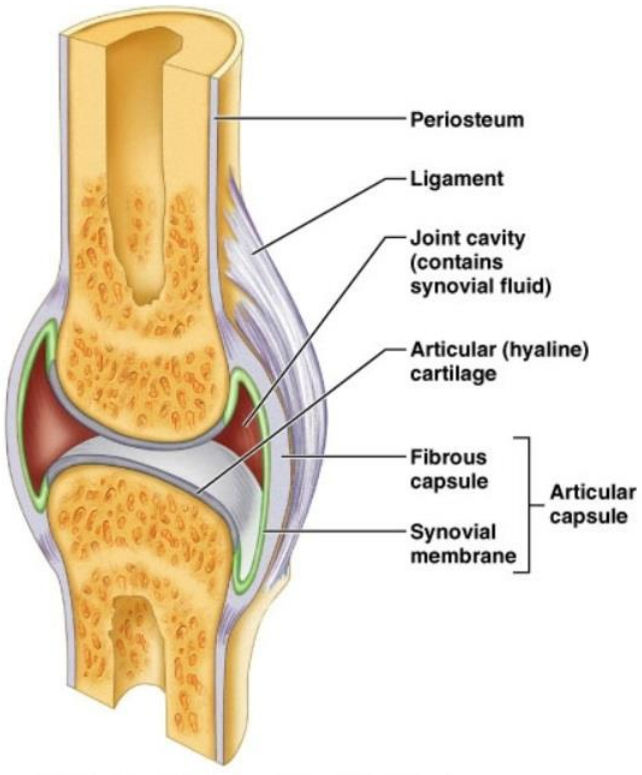

Figure 1-3 Schematic illustration of a synovial joint and its major components [31].

The main components of these joints are articular cartilage and synovial fluid, as presented in Figure 1-3 [5,24,30]. Articular cartilage is a soft material which is supported by

the bone and protect the bones from direct contact in order to decrease friction and wear during sliding [5,14,30]. The thickness of articular cartilage depends on its location in the body. The thickest cartilage is located in the lower part of the human body as the load is highest there. The thickness measured for cartilage found in the human ankles and knees is ranging from 1.00 mm to 1.62 mm and 1.69 mm to 2.55 mm, respectively [24]. The thickness of the cartilage in the hip is between 1.35 and 2.0 mm [32]. The measured Young's modulus varies from 12 to 50 MPa [28].

The solid matrix of cartilage is mainly composed of collagen and proteoglycans. This tissue contains about 80% water. Articular cartilage has a multilayered structure in which the orientation of fibers, water contents, and type and concentration of proteoglycans change through the depth, as shown in Figure 1-4[30,33]. As can be seen, collagen fibers are oriented parallel to the surface of the very top layer of the cartilage. Close to the bone, collagen fibers are large and perpendicularly oriented, similar to polymer brushes whose lubrication behavior will be discussed in further detail in section 1.3.

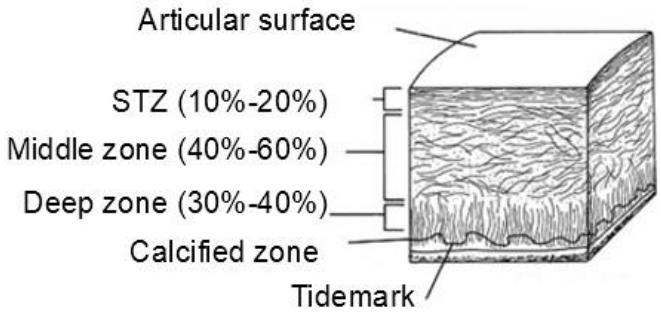

Figure 1-4 Multilayered structure of articular cartilage [33].

Recent studies classified the different lubrication modes in articular cartilage as boundary, interstitial, and mixed lubrication [34]. The lubrication mechanism of articular cartilage depends on the interactions between the solid matrix (i.e., collagen-proteoglycan network) and the fluid phase (i.e., interstitial fluid) [29,34–40]. During interstitial lubrication, the interstitial fluid, which makes 70-80 % of the cartilage, supports a large fraction of the load as the fluid phase is incompressible. The low friction can be obtained as long as the fluid phase supports the load [34,40]. However, the flow of the interstitial fluid inside the tissue can generate a drag force and lead to friction. The fluid phase supports the load until it is squeezed out into the joint space [34]. As the load on the solid phase increases, the interstitial fluid starts

to exude from the solid matrix to the friction gap [34]. At a certain point, all the load might be carried by the solid phase [37], however, the solid matrix is not easy to compress due to the repulsive force between the negatively charged proteoglycans. Furthermore, the mutual interpenetration of the solid matrix of the cartilage on the opposing surfaces is restricted to a narrow interfacial region; thus, the interface is maintained as a highly fluid layer as a result of the hydration layer surrounding the proteoglycans [41]. The friction generated in articular cartilage in such a case is mainly due to interactions and shearing of the solid phase (boundary lubrication). Under boundary lubrication condition, synovial fluid, which is made of long-chained proteins, hyaluronic acid, and phospholipids, assures the effective lubrication. Therefore, the extraordinary performance of synovial joints is obviously not the result of a single component but the synergy between all components, i.e., the synovial fluid and articular cartilage.

1.2 Tribology

Tribology is the science dealing with friction, lubrication, and wear of the contacting surfaces that are moving relative to each other. As a consequence, tribology is a system behavior, not a single material property [42,43]. As the surface interaction controls every moving object's performance and lifetime, tribology attracts ever-growing attention. To study the tribological behavior of a system, rheological properties of the lubricant, mechanical and chemical properties of the two contacting surfaces must be considered.

Although the application of lubricants has begun long ago in history, Leonardo Da Vinci was the first who has introduced the concept of friction into the scientific literature. He distinguished different types of friction and differentiated between sliding and rolling friction [42]. Indeed, Leonardo stated the two basic laws of friction even before Newton defined the concept of force. Later on, Amonton verified his observations and rediscovered the first two classical laws of friction. According to the two first laws, the friction force is proportional to the applied load and independent of the apparent contact area [42]. Coulomb added the third law declaring that the friction force does not depend on the velocity during sliding [42]. He also made a distinction between static and kinetic friction [42–44]. These basic laws of friction are quite valuable in understanding the behavior of many different tribological scenarios; however, they do not hold for all cases. Introducing a single model that can describe any frictional system remains elusive due to complexities and interactive variables that affect the frictional behavior

of systems [43]. In spite of the situation that tribology utilizes sliding and rolling components to a large extent, almost one-third of the world's energy resources, which is currently in use, is estimated to be wasted due heat dissipation caused by friction or due to wear which leads to the need of replacement of worn parts [42]. Research in tribology aims for minimization and elimination of losses resulting from friction and wear. The direct outcome of reduced friction and wear will be higher efficiency, better performance, fewer breakdowns, and significant savings [42].

1.2.1 Friction and adhesion

When a solid body moves on another, a resistance force appears in the opposite direction of the movement, which is called friction force. If the solid bodies are brought into contact at rest, and a tangential force is applied subsequently, the required force to initiate the motion is called static friction force. The static friction is the result of the adhesion between the two opposing surfaces. The tangential force needed to maintain the relative motion is named kinetic friction force [42]. The static friction force is either higher than or equal to the kinetic friction force. The first rule states that the friction force (F_f) is directly proportional to the normal load (F_N). By increasing the normal load, the surface asperities of the opposing surfaces get in further contact. The first law of friction is given in eq. (1-1):

$$F_f = \mu F_N \tag{1-1}$$

where μ is the coefficient of friction, F_f is the friction force, and F_N is the normal force.

All solid surfaces possess a certain surface roughness. Only very few surfaces, such as cleaved mica or graphite, are atomically smooth. When the asperities come into contact, they have to be elastically or plastically deformed to initiate and maintain the motion. In this case, a part of the energy will be dissipated as heat [45]. Bowden and Tabor suggested that for two metallic surfaces sliding against each other, high pressures lead to welding of some asperities that have to be sheared to start the motion. Later, it was proposed that the interfacial adhesion between asperities is sufficient to result in friction. Regardless of the deformation type (elastic or plastic), breaking adhesive bonds during motion requires energy [46]. The total friction force (F_f) can be written as the sum of the force needed to shear adhered junctions (F_A) and the force needed to supply the energy of deformation (hysteresis) (F_d) that can be induced by plastic

deformation and viscoelastic losses. The two main components of friction are shown schematically in Figure 1-5 [46].

$$F_f = F_A + F_d \qquad (1\text{-}2)$$

Deformation is a consequence of energy loss associated with internal damping within the viscoelastic body during sliding. For polymers, particularly elastomers, F_d has a significant contribution to the friction force because of a large internal viscous dissipation [47,48]. As considerable molecular conformation can occur without breaking of covalent bonds. In Figure 1-6, the influence of damping loss on the friction is shown for a P.T.F.E sample [48]. As can be seen, COF and damping loss follow the same behavior confirming that damping losses due to sliding of the chains over each other seem to be the main source of friction even at high strains for elastomers[48].

The adhesive frictional force component (F_A) is a surface effect; thus, it depends on the interfacial shear strength and the real contact area [47–49]. Both forces in eq. (1-2) depend on the physical and chemical properties of the surfaces in contact, the load, and the sliding velocity. Indeed, the friction force is an interplay between all these components [46].

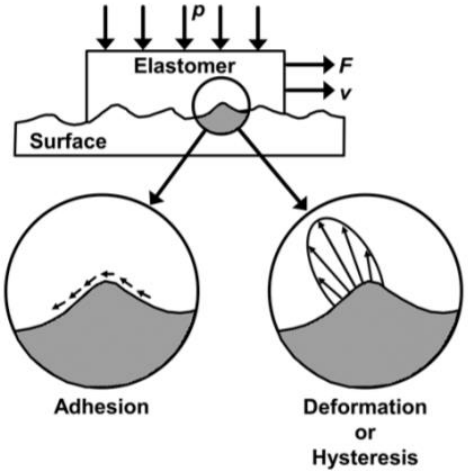

Figure 1-5 Force components of friction force for a rubber sliding on a rough surface [19,50].

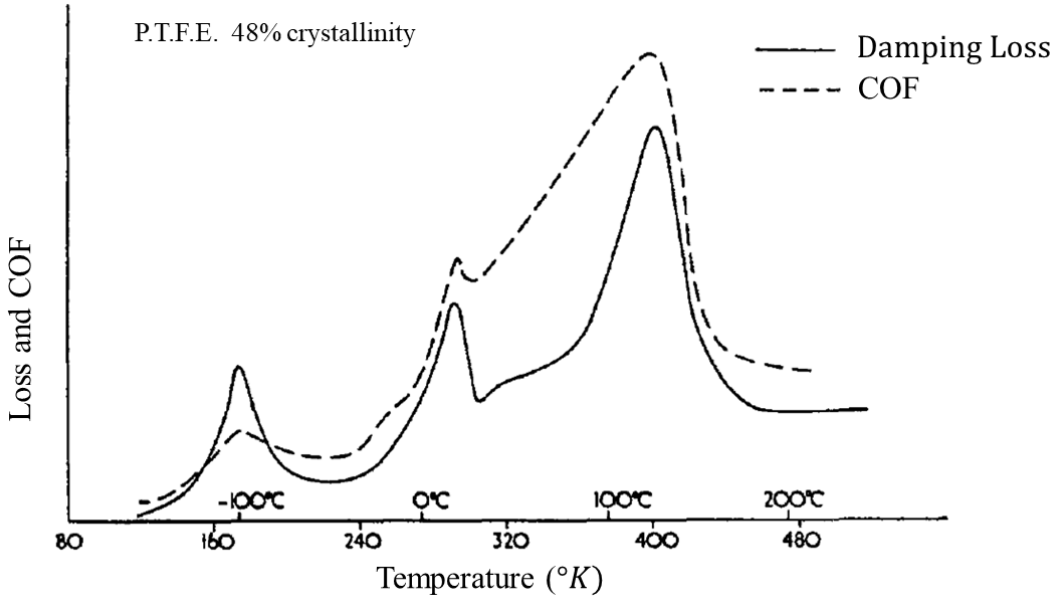

Figure 1-6 Damping loss and coefficient of friction as a function of temperature for P.T.F.E. with 48 % crystallinity [48].

Adhesive contacts are the result of physical or chemical interactions. A chemical interaction includes covalent, electrostatic, and metallic bonds; and physical interaction involves the formation of the hydrogen bonds and van der Waals interactions, which are much weaker than the chemical interactions because, in such secondary bonds, there is no electron exchange or formation of joint molecular orbitals [42]. There is always a van der Waals interaction between two surfaces in close proximity. Thus, to start the motion, the interaction forces have to be overcome. The fracture occurs in the weakest regions, either at the interface or in one of the mating bodies. After shearing the existing adhesive junctions, new contacts are formed. The adhesive forces can be as strong as the forces between the molecules themselves. In such a case, the shearing process may actually tear out fragments of the materials [42].

1.2.2 Lubrication and Stribeck curve

Thin layers of gas, liquid, or solid are usually introduced between two solid surfaces in contact to facilitate the movement of one surface on another [51,52]. A few ppm of contaminants may be sufficient to reduce friction dramatically. Thick films of liquids or gases would further reduce friction as it is much easier to shear into a fluid film than to shear a solid-solid contact [42]. Lubricant films in the friction gap are often very thin, with a thickness ranging from 1 to 100 µm, and their lubrication mechanism is difficult to be observed in-situ

[52]. The principal limitations of, in particular, liquid lubricants are the loss of load-carrying capacity at high temperatures and potential degradation abilities [51].

The lubrication state changes depending on the lubricant thickness; however, this thickness has to be compared to the surface roughness to determine the accurate lubrication state [51,52]. Friction experiments on bearings by Stribeck exhibited different lubrication regimes [53–55]. Typical Stribeck curves describe a relation between the coefficient of friction (μ), viscosity of the lubricant (η), normal load (F_N) and velocity (v) with the lubrication regime. According to the Stribeck curve (shown in Figure 1-7), lubrication can occur in three various regimes. These regimes are boundary (region I), mixed (region II), and hydrodynamic lubrication (region III). A dimensionless number ($\eta v/F_N$), which is called Sommerfeld number, determines in which regime the system operates [51–55]. The three main lubrication regimes are:

I) Boundary lubrication: in this case, the thickness of the lubricating film (h) between the sliding surfaces is smaller than their surface roughness (R), which means asperities are in direct contact. This lubrication regime occurs at system conditions of low fluid viscosity, small relative velocity, and/or high normal load. In this regime, the surfaces are engaged in direct contact. Thus, the topography and chemistry of the surface (energy of adhesion) are the most determinant parameters. The real contact area is much smaller than the apparent contact area [51,52,54–56].

II) Mixed lubrication: this lubrication regime occurs between boundary lubrication and hydrodynamic lubrication regimes in the Stribeck curve, as shown in Figure 1-7. In this case, asperities are partially in contact and partially separated by a fluid film. By increasing applied load or slower sliding (smaller Sommerfeld number), the friction coefficient increases as the fluid film becomes thinner and more asperities come in contact. Such a rise in the friction coefficient is also related to the viscosity increase in some regions at the contact area under the high contact pressure. Increasing the applied load or decreasing the sliding speed (reduction of the Sommerfeld number) makes contact between the asperities stronger. Consequently, the film thickness becomes smaller than the height of surface asperities, and then lubrication shifts to the boundary lubrication regime [51,52,55].

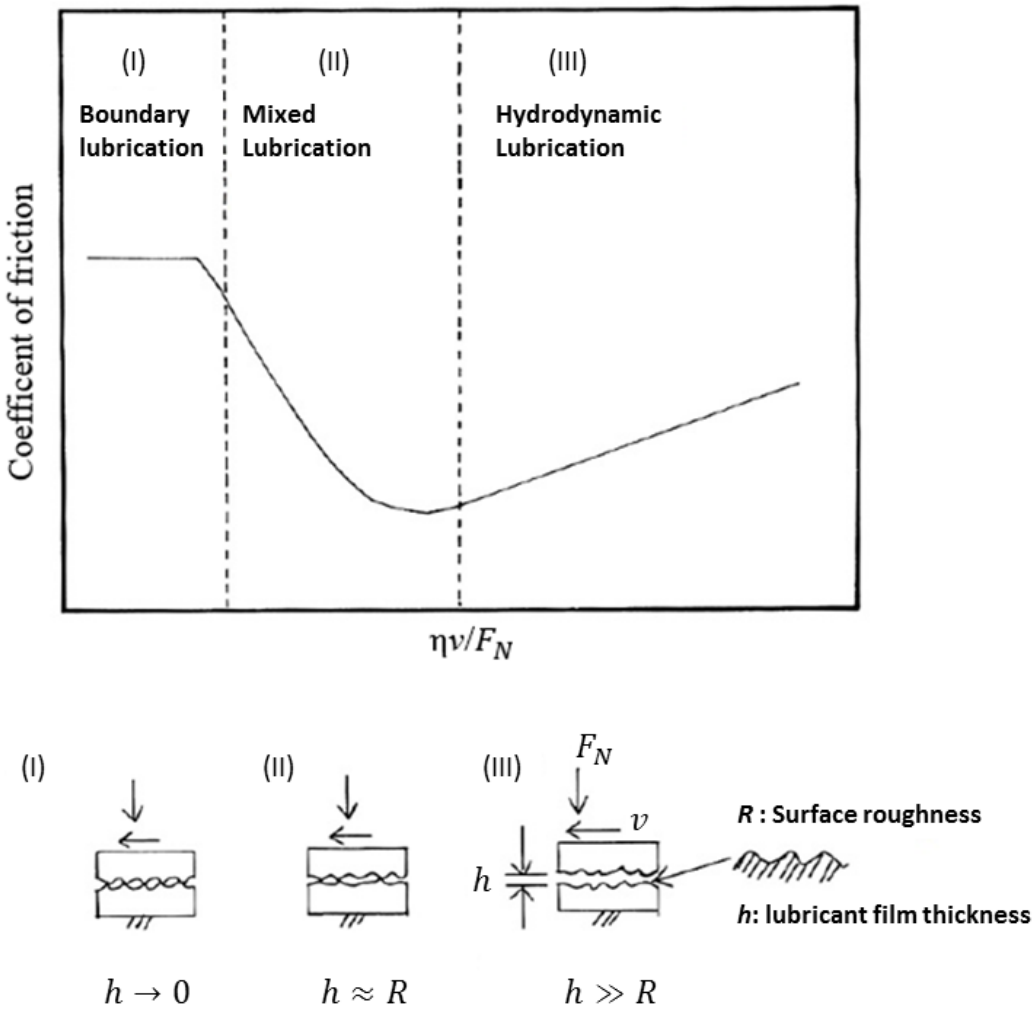

Figure 1-7 Stribeck curve showing lubrication regimes observed in fluid lubrication; friction coefficient as a function of Sommerfeld number [56].

III) Hydrodynamic lubrication: when the sliding speed or viscosity of the lubricant is high enough or the normal load is relatively small, in the lubricant film a hydrodynamic lift force is generated which separates the surfaces. In the presence of a film with thickness much larger than the size of asperities (R), the surfaces are completely separated and do not interact directly. The lubrication behavior in this regime is determined by the rheological properties of the fluid film separating the two surfaces. The viscosity of the fluid (internal friction of the fluid) is the most important parameter. By increasing the load or decreasing the viscosity and/or velocity, the Sommerfeld number ($\eta v/F_N$) is reduced. The decrease of Sommerfeld number leads to a thinner fluid film, and a lower coefficient of friction until it reaches a minimum value [51,52,54,55].

The typical friction coefficient range is given for different lubrication regimes in Figure 1-8 [51]. As can be seen, the highest values of COF appear in dry friction, when no lubricant is involved. The dry friction values are given for pure metal and oxide films, as these values might be different depending on the material. The COF decreases by adding a lubricant to the contact. The lowest values of COF occur in mixed and hydrodynamic lubrication regimes, where the contact surfaces are separated partially or completely by the lubricant film, respectively.

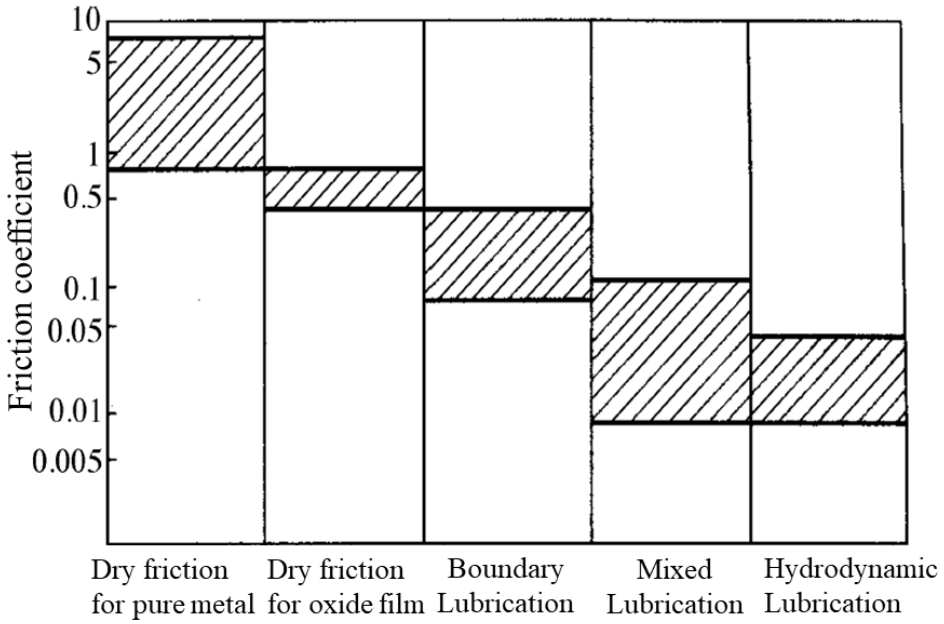

Figure 1-8 Typical friction coefficient range for different lubrication regimes [51].

1.2.3 Thin film lubrication

A lubrication regime, known as thin film lubrication, might appear in some of the lubricated contacts, where lubricant has an anisotropic viscosity. A physical model has been proposed for the thin film lubrication, in which the thin film of the lubricant consists of three different layers namely: the adsorption film, the orderly liquid film, and the viscous fluid film as illustrated in Figure 1-9 [57]. In this lubrication regime, the gap size is in the range of several nanometers to tens of nanometers, and the lubricant film is dominated by molecular behavior in different regions. Close to the solid surface, the film consists of two layers. The first layer is the adsorbed film formed during the static contact. The other one is the orderly liquid film formed during lubrication [51]. The thickness of the adsorption film is only several molecular layers of the lubricant that are connected firmly to the surface [57]. The absorbed film shows boundary lubrication characteristics, so it can also be called as the boundary lubrication film. As the central layer shows elastohydrodynamic lubrication characteristics, it is known as

elastohydrodynamic lubrication film [51]. The ordered liquid film is located in the interface of the viscous fluid film and the adsorption film [44].

The changes in the thickness ratio of these three layers determine the transition of lubrication regimes. If the solid surfaces are far from each other, the fluid layer will be thicker to accommodate hydrodynamic effects. However, if the two solid surfaces are so close to each other, a boundary lubrication regime will appear [57].

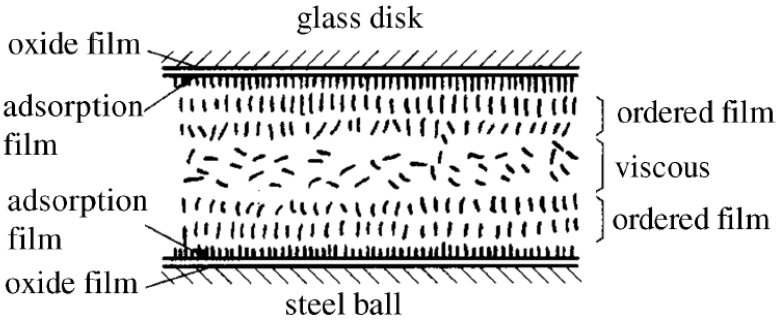

Figure 1-9 Multilayers of a thin film lubrication model consisting of ordered film, adsorbed film, and a viscous layer [51].

1.2.4 Contact mechanics models

Contact mechanics models can be classified as non-adhesive contact and adhesive contact models. Regarding the non-adhesive contact model, which is the Hertz model, it is assumed that there are no adhesive interactions between the contacting surfaces. In the latter case, including Derjaguin-Muller-Toporov theory (DMT), Johnson-Kendall-Roberts theory (JKR), and Maugis-Dugdale theories, adhesion occurs at contact. In the following different theories are briefly discussed [2].

1.2.4.1 Hertz theory

The Hertz theory describes the stresses and strains for smooth, non-conforming surfaces in contact for both static and quasi-static loading. The Hertzian contact usually refers to the contact between two elastic spheres of different radii (non-adhesive contact), as shown in Figure 1-10. In Hertz theory, several assumptions are made [45–48]. The strains are considered to be small so that they can be described by the linear theory of elasticity. The contact area is much smaller than the characteristic dimensions of the contacting bodies. The bodies in contact can be considered as an elastic half-space. The interaction involves only pressure acting normal to the planar contact area (frictionless contact).

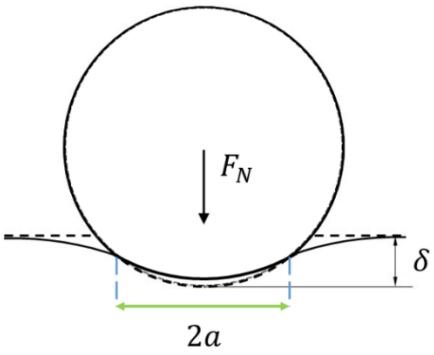

Figure 1-10 Contact between two elastic bodies with negligible adhesion (Hertz theory).

Hertz's solution for the indentation of an elastic half-space by a sphere relates the indentation depth or distance of mutual approach (δ) to the applied normal load (F_N) through eq. (1-3) [2,58,59]:

$$\delta = \frac{a^2}{R} = \left(\frac{9F_N^2}{16RE_{eff}^2}\right)^{\frac{1}{3}} \tag{1-3}$$

Here R is the radius of the indenting sphere, a is the contact radius and E_{eff} is the contact modulus, defined by eq. (1-4):

$$\frac{1}{E_{eff}} = \frac{1-\nu_1^2}{E_1} + \frac{1-\nu_2^2}{E_2} \tag{1-4}$$

where E and ν are Young's modulus and Poisson's ratio, with the subscript 1 indicating the material of the indenter and subscript 2 that of the half-space being indented, respectively.

The relation between the contact radius (a), applied normal load (F_N) and the contact modulus (E_{eff}) is as below:

$$a^3 = \frac{3F_N R}{4E_{eff}} \tag{1-5}$$

The maximum pressure between two surfaces, according to Hertz theory, can be obtained as follows [2,58,59]:

$$p_{max} = \frac{3F_N}{2\pi a^2} = \frac{1}{\pi}\left(\frac{6\pi E_{eff}^2}{R^2}\right)^{\frac{1}{3}} \tag{1-6}$$

Hertz model does not account for adhesion between the probe and the sample. The adhesive forces result in a larger contact radius than that calculated by the equation, as shown above. In addition, the adhesive forces change the indentation depth δ, and the elastic energy stored in the system as well.

1.2.4.2 JKR, DMT and Maugis-Dugdale theories

Models, which also take the occurrence of adhesive contacts between the bodies into account are the JKR (Johnson-Kendall-Roberts), DMT (Derjaguin-Müller-Toporov) and Maugis-Dugdale model:

1) JKR model considers adhesive contact by assuming a balance between the stored elastic energy and the loss in surface energy. Taking into account the adhesive interactions, the contact area under a given load is larger than the one predicted by the Hertz theory (schematically shown in Figure 1-11) [60]. As a result of strong attractive forces, the spherical region within the contact area deforms toward the flat surface and produces necking behavior [2]. The work of adhesion (W_A) can be described as:

$$W_A = \gamma_1 + \gamma_2 - \gamma_{12} \qquad (1\text{-}7)$$

Here γ_1 and γ_2 are the adhesive energies of the contacting bodies and γ_{12} is the interaction energy. The contact radius formed according to the JKR theory can be obtained by.:

$$a^3 = \frac{3R}{4E_{eff}}\left(F_N + W_A\pi R + \sqrt{6W_A\pi RF_N + (3W_A\pi R)^2}\right) \qquad (1\text{-}8)$$

If the work of adhesion (W_A) set to zero in the above equation, the resulting equation will be the same as in Hertz theory (eq. (1-5)).

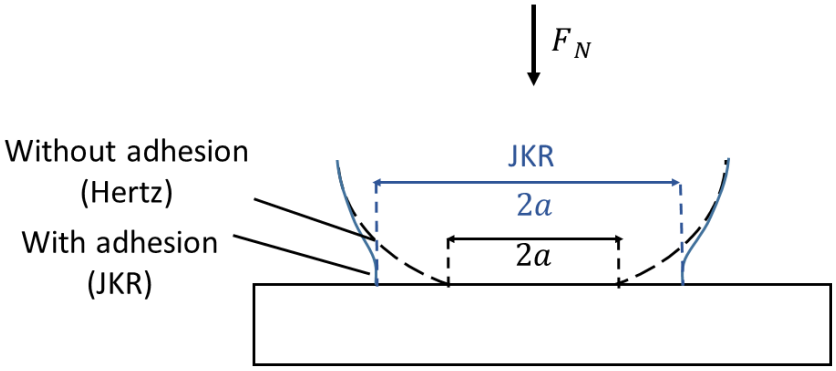

Figure 1-11 Schematic comparison of the Hertz and JKR models.

2) DMT model assumes that the adhesive forces do not change the contact area significantly. Adhesive forces within the contact area are neglected so that the contact area can be assumed to be equal to Hertzian (see Figure 1-12). However, the adhesive forces between the indenter and surface produce a contact area larger than the Hertz model. Thus, this model can accurately describe materials with large moduli [61]. According to DMT theory, attractive forces between the bodies have a finite range and act outside the contact zone where the surfaces are a small distance apart [60]. The contact radius from DMT theory is:

$$a^3 = \frac{3R}{4E_{eff}}(F_N + 2W_A\pi R) \tag{1-9}$$

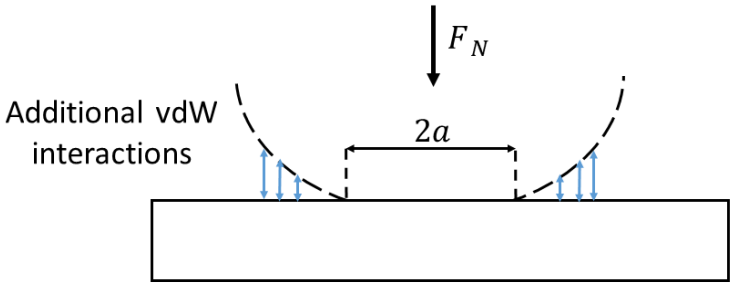

Figure 1-12 DMT theory assuming the same contact area as Hertz with attractive interactions outside the contact area.

3) Maugis-Dugdale model applies in between the previously mentioned two models [62]. This model considers surface traction distribution to be the contribution of the Hertz contact pressure and Dugdale adhesive stress. It is assumed that the molecular attraction force acts with a constant intensity only within a ring zone at the contact area border up to a specific separation distance.

Adhesive contact between large spheres with high surface energies and low elastic moduli can be described better by the JKR theory, whereas the adhesive contact between the smaller spheres with low surface energy and high elastic moduli can be predicted by the DMT model [63].

Numerical solutions to the contact problem by considering the Lennard-Jones potential illustrated that the two models (i.e., JKR and DMT) correspond to the two different ends of a spectrum of a non-dimensionless parameter called Tabor parameter [63]. Thus, the so-called Tabor parameter can quantify which contact model represents the adhesive contact better for a specific contact configuration. It is based on a ratio between the energy for deformation of the

contacting body and the energy of interaction at the contact area. It can be calculated using the equation below [2,58,61]:

$$\mu_{tb} = \left(\frac{RW_A^2}{E_{eff}^2 Z_0^3}\right)^{\frac{1}{3}} \quad (1\text{-}10)$$

In the above equation, R is the radius of curvature of the indenter, W_A is the work of adhesion per unit contact area, E_{eff} is the contact modulus and Z_0 is the equilibrium distance of the surfaces in the Lennard Jones potential.

Tabor suggested that when the Tabor number is large ($\mu_{tb} > 1$), the necking of the sphere is also large, and the attractive forces outside the contact area can be neglected, thus the JKR model is appropriate. In contrast, when the necking is negligible ($\mu_{tb} <1$), the attractive forces outside the contact area are dominant [63]. In this case, the DMT model describes the contact behavior better [64].

The different theories are compared schematically in Figure 1-13 [61] concerning the forces occurring during an indentation test. It can be seen that following Hertz theory, indentation depth and contact force are zero at the initial contact point and at the separation point. However, in JKR, DMT, and MD theories, adhesive or attractive interactions are present. The major difference between DMT and JKR theories is the relation between the contact area and the applied normal load. In the DMT theory, at the point of initial contact and separation point contact area is assumed zero (similar to Hertz), but the contact area is never zero in the JKR model [61].

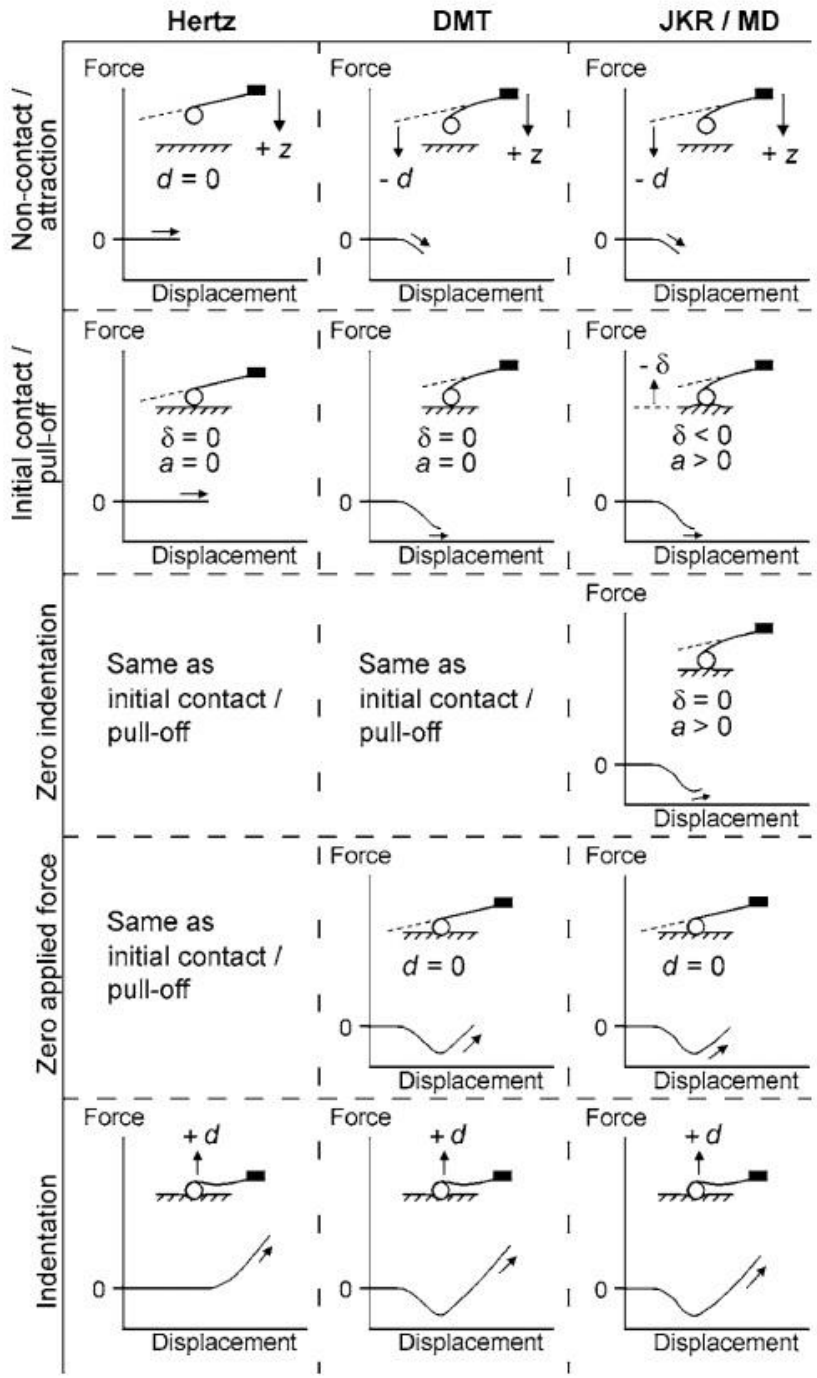

Figure 1-13 Schematic comparison of different contact mechanics models on their force-distance curve [61].

1.3 Polymer brushes for reduced friction

Inspired by synovial joints, many systems based on polymer bearing surfaces such as polymer brushes have been investigated [41,65,74,75,66–73]. Polymer brushes are polymer chains that are anchored by one end to a substrate and extend out into the surrounding medium

due to steric repulsion and osmotic pressure. Polymers with different chemical structures, compositions, and functionalities can be tethered to the substrate surface via physisorption or chemical bonding, as illustrated in Figure 1-14 [74].

Formation of brushes by physisorption occurs by having polymer chains that are attracted to the substrate by one end while the other end interacts very weakly with the substrate. Chemical bonding of polymer brushes onto the substrate provides a stronger attachment to the substrate. Chemical bonding of polymer brushes can be done by "grafting-to" or "grafting-from" approaches [74].

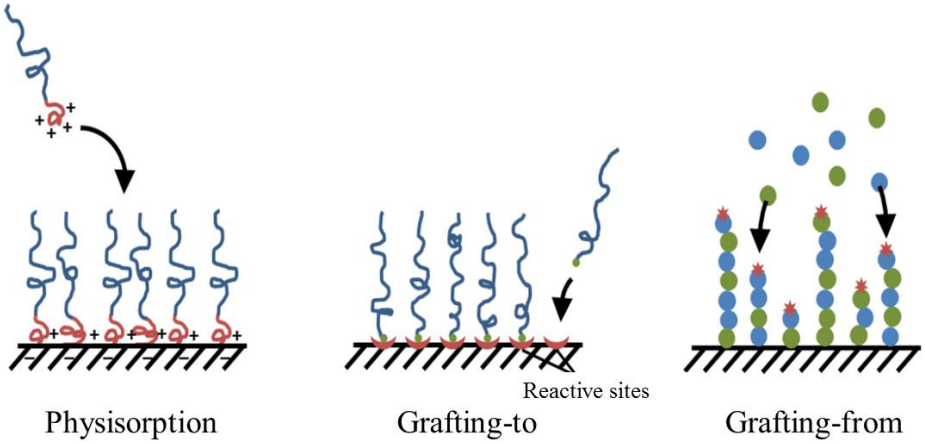

Figure 1-14 Different tethering mechanisms for surface modification by polymer brushes [74].

Polymer brush coated surfaces exhibit very low friction in a good solvent [41,65,75,66–71,73,74]. Klein *et al.* have extensively studied the frictional properties of brushes using surface force apparatus (SFA) [41,65,70,71,73]. Strong repulsive forces of entropic origin largely prevent the interpenetration of polymer chains opposing surfaces. Previous studies have shown that the segment density of adsorbed polymers decays rapidly with distance from the substrate (Figure 1-14b). For the polymer brushes, the monomers are repelled by the surface. Thus, for the brushes, a slowly decaying parabolic function was observed (Figure 1-14a) [76]. It has been suggested that the repulsive forces accommodate the formation of a thin fluid film between opposing brushes, which leads to friction reduction [23,66,70]. Some studies have been carried out to investigate the effect of different parameters like the chain length, grafting density, chain stiffness, and the solvent state on the tribology of polymer brushes [77].

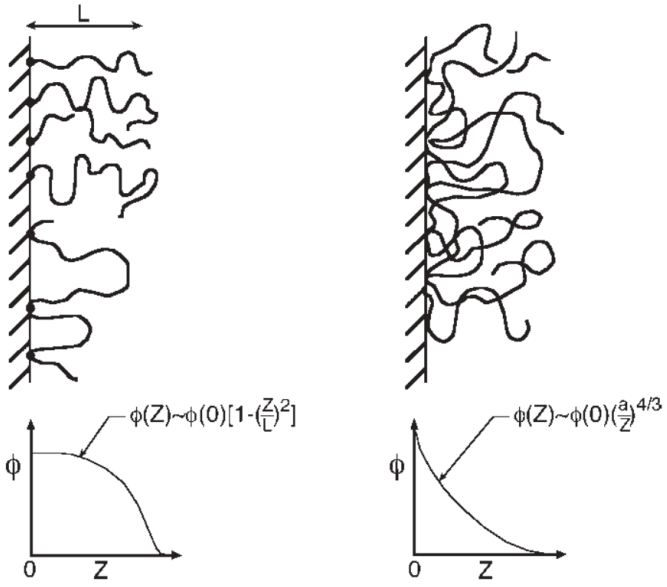

a) b)

Figure 1-15 Segment density profiles of a) brushes (end grafted and pseudo brushes) b) adsorbed polymers [23].

In further detail, the origin of low friction between brush bearing surfaces is thought to be the occurrence of the following phenomena [23]. As two polymer brush coated surfaces are compressed, a very small interdigitation happens [41]. Due to configurational entropy effects, it is favored for the two brush coated layers to be compressed than to interdigitate [23]. The repulsive interactions help with the formation of a thin layer of the fluid at the interface, which is very easy to shear, leading to small friction. With these two mechanisms, neutral brushes can serve as efficient lubricants, although at high pressures, significant interpenetration occurs (Figure 1-17a), and the frictional drag rises correspondingly. The three influential mechanisms can be seen in Figure 1-16 [23].

For adsorbed polyelectrolytes, the efficiency of lubrication is mainly reduced because of bridging effect, as illustrated in Figure 1-17b. The bridging occurs since the monomers tend to adsorb each other and minimize the free energy. During sliding, the bridges are stretched, and the frictional drag increases, leading to inefficient lubrication at high pressures [23].

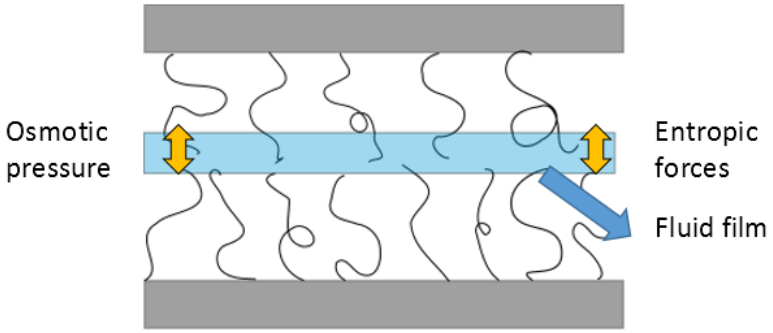

Figure 1-16 Friction reduction mechanism of two brush bearing surfaces.

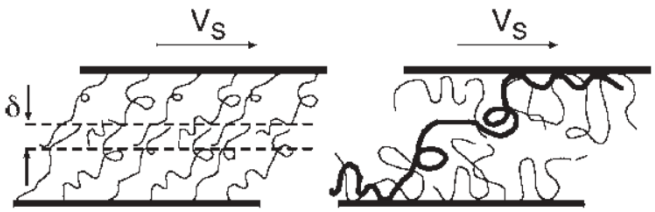

a) b)

Figure 1-17 Interaction between two sliding surfaces at high pressures coated by a) brushes-interpenetration (δ) occurs at high pressures between brushes b) adsorbed polyelectrolytes-bridging may appear [23].

Raviv *et al.* have investigated the lubrication of surfaces coated by polyelectrolyte brushes. Polyelectrolyte brushes were generated on the hydrophobized mica surfaces by the diblock copolymer of poly(methyl methacrylate)-block-poly(sodium sulfonated glycidyl methacrylate) copolymer (PMMA-b-PSGMA). The surface attachment takes place through hydrophobic PMMA moieties to form end-tethered layers of charged PSGMA moieties [71]. Polyelectrolyte brushes can still be efficient at higher pressures (black triangles in Figure 1-18) [78]. The friction coefficient measured for polyelectrolyte brushes was on the order of 0.001 or lower at pressures of a few hundreds of kPa [71]. In the case of charged brushes, efficient lubrication is not only the consequence of excluded volume but also higher osmotic pressure due to the presence of mobile counterions in the brush layer and the electrostatic double-layer arising from the brush [23,78]. At the highest pressures, the entropic considerations are not sufficient to avoid interpenetration. It is the hydration layer surrounding the interpenetrated charged monomers that provide low friction by polyelectrolyte brushes [78]. As the pressure was increased further, the brush layers were torn off from the substrate [71].

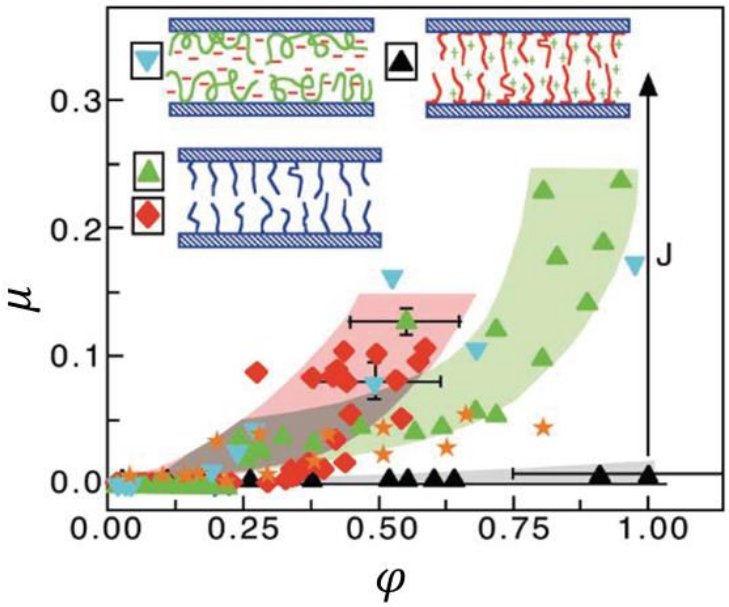

Figure 1-18 Coefficient of friction as a function of the volume fraction. At low compressions, neutral brushes (diamonds and light upright triangles), adsorbed neutral polymers (stars), and adsorbed polyelectrolytes (light inverted triangles) are efficient lubricants, only the polyelectrolyte brushes (black upright triangles) are efficient at the highest compression [23,78].

1.4 Tribology of Hydrogels

Hydrogels are hydrophilic networks that are chemically or physically crosslinked [79–81]. They can take up water and swell to a large extent [79]. The ability to absorb water is the result of hydrophilic functional groups attached to the polymer backbone and/or a hydrophilic backbone, while their resistance to dissolution is due to the crosslinks between the network chains [80]. The crosslinked network helps the hydrogel to retain its shape when stress is released resembling solid-state properties, while water stored inside the network can flow in response to an applied load through the permeable network of the hydrogel [82]. Hydrogels are classified into chemical and physical gels. Polymer chains of chemical gels are connected to each other by covalent bonds, whereas physical gels are formed by physical interactions. Consequently, chemical gels are mechanically more stable than the physical ones [80].

Being bicomponent, with low compliance, and in some cases, stimuli-responsive, hydrogels are unique materials for medical applications. Hydrogels are suitable candidates for drug delivery [64,83], actuators, and sensors [84] and scaffolds in tissue engineering [14,85–87]. The stimuli can be the change in the temperature, pH, mechanical forces, electric charges,

magnetic forces, and the presence of solvents or ions [80]. Despite fascinating properties, hydrogels can only be used in the human body if the prolonged contact with the surrounding tissue, interactions with them, and their biocompatibility are considered [64].

Hydrogels (polymer brushes as well) are increasingly used to mimic the slippery nature of biological interfaces such as joints and eye [36,71,83,88–90]. In such contacts, there is no clear boundary between the solid and liquid phases. Understanding the lubrication mechanisms of surfaces with combined solid and fluid character is challenging as the fluid contribution to lubrication has to be captured. Studying the frictional behavior of hydrogels is helpful for understanding the low friction mechanism observed in biological systems, and might be useful in finding novel approaches in the design of low-friction systems.

1.4.1 Elastic, viscoelastic and poroelastic materials

When no force is exerted on a material, the neighboring atoms are in equilibrium, meaning that the attractive and repulsive forces are balanced. When an external force is applied, atoms have to move either apart or come closer to balance the external force. The relation between the interatomic force and interatomic distance is shown in Figure 1-19 [91]. When the displacement of atoms is small, the atoms can go back to their initial position. This type of reversible deformation is called elastic deformation, whereas irreversible displacement of atoms leads to a permanent deformation termed as plastic deformation. As the applied load exceeds the yield stress point, the deformation changes from elastic to plastic [92]. The difference in the stress-strain curve is shown for different types of material deformation in Figure 1-20. Within a small range of deformation (elastic deformation), the relationship between force and deformation is mostly linear [91].

For linear elastic materials, the stress-strain relation is linear, as described by Hook's Law (eq. (1-11)). These materials deform elastically, which means that they retain their initial shape upon unloading [91].

$$\sigma = E\varepsilon \tag{1-11}$$

Here σ is the stress, ε is the strain, and E represents the elastic modulus of the material, also known as Young's modulus. For elastic materials, the stress response to the tension/compression depends only on the strain, as deformation and relaxation occur at time scales much shorter than that of the measurement [91].

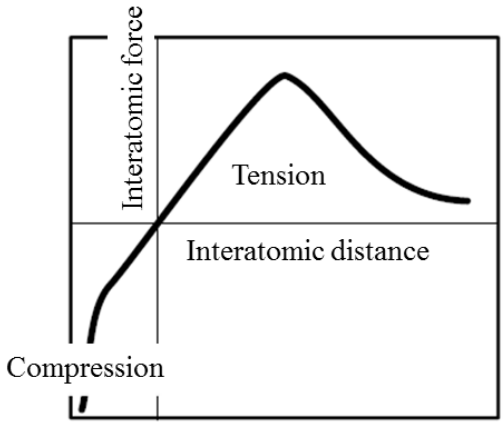

Figure 1-19 Interatomic distance and force relation under tension and compression [91].

An immediate consequence of the viscoelasticity is that the deformations under stress are time-dependent [91]. For many soft materials, including most hydrogels, the elastic response is accompanied by a time-dependent deformation [93]. In Figure 1-20, different types of stress-strain curves that can happen to different kinds of materials are presented. In an elastic material, there is no energy dissipation. In contrast, for viscoelastic materials, energy is being dissipated when a load is applied and removed, resulting in hysteresis in the stress-strain curve. The area of the loop is equal to the energy loss during the deformation and recovery.

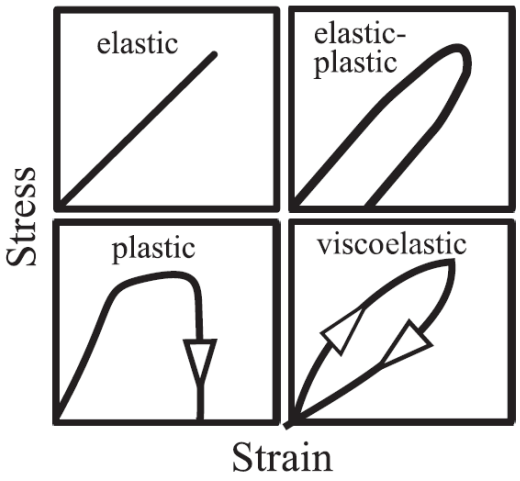

Figure 1-20 Stress-strain curve for different types of material behavior [91].

The stress-strain relationship for viscoelastic materials can be described by different models, such as the Maxwell Model and Kelvin-Voigt Model [94]. Viscoelastic behavior has elastic and viscous components that are modeled using springs and dashpots, respectively. In order to predict the viscoelastic behavior, each model is described by different arrangements of springs and dashpots [58]. In the Maxwell model, the spring and the dashpot are connected in series. In

this configuration, both elements undergo the same stress. The strain rate equation for the Maxwell model is given in eq. (1-12). In this equation, η is the viscosity of the material [3,91,95].

$$\frac{d\varepsilon}{dt} = \frac{1}{E}\frac{d\sigma}{dt} + \frac{\sigma}{\eta} \qquad (1\text{-}12)$$

The spring and dashpot are connected in parallel in the Kelvin-Voigt model, where both elements are subjected to the same strain but different stress. The equation for the stress in the Kelvin-Voigt model is [91,96]:

$$\sigma = E\varepsilon + \eta\frac{d\varepsilon}{dt} \qquad (1\text{-}13)$$

Poroelasticity is a term used to explain the interaction of the fluid phase and solid phase in a porous media. By applying a load, the fluid phase filling the pores must be displaced as a result of the change in the volume fraction of the pores. The solid phase deforms under the load simultaneously [95,97,98].

Likewise, in response to changes in mechanical forces, two concurrent molecular processes occur in gels: the conformational change of the polymer network and the migration of the solvent through the network. As a result of these two processes, gels can be considered as viscoelastic and poroelastic materials. Viscoelasticity and poroelasticity of gels can be characterized by two properties: the viscoelastic relaxation time and the diffusivity of the solvent through the network [95]. For a gel with a large pore size (mesh size) and low viscosity solvent, upon compression solvent can be squeezed out of the gel, and the mechanical response is determined by the polymer matrix [28,95]. In contrast, the response is dominated by the solvent pressurization inside the pores in case of fine pores or viscous solvents. Two models were developed for biphasic materials composed of a porous solid phase and an incompressible fluid phase as: biphasic poroelastic model (PE) and biphasic poroviscoelastic model (PVE) [28].

PE is initially proposed to explain the lubrication mechanism of articular cartilage [99]. In the PE model, the solid phase is assumed to be linear elastic. Upon compression, the PE model predicts an increase in normal stress due to solid deformation and fluid pressurization [28]. After reaching the maximum normal stress and while keeping the imposed displacement

constant, the structure relaxes to an equilibrium stress state as the fluid phase drains out through the pores. Figure 1-21 shows the change of the normal stress in a poroelastic material by the time [28]. During the compression phase, the normal stress rises continuously, and at the relaxation phase, due to the drainage of the fluid, it decreases by time and reaches an equilibrium state.

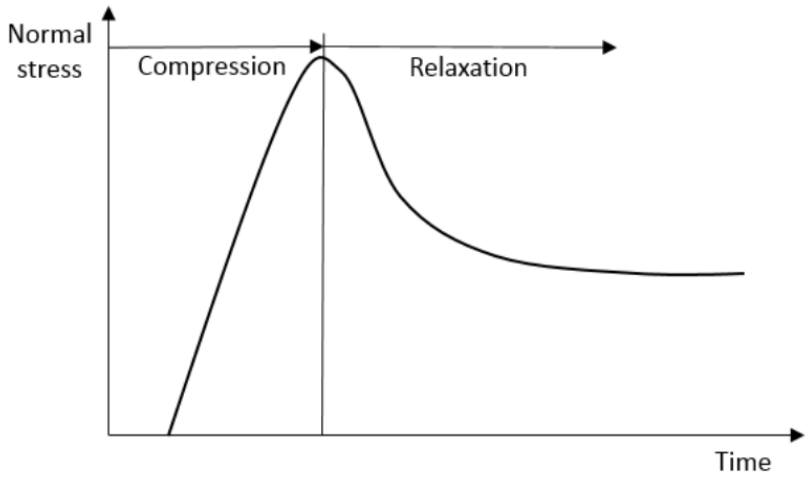

Figure 1-21 The change of the normal stress on a poroelastic material versus time [28].

Since the fluid phase can drain quickly in a highly permeable material, the viscoelasticity effect becomes negligible. However, for the gels with lower permeability, a much lower rate of fluid exudation imposes viscoelastic behavior on the material. For such cases, the PE model might not be the appropriate model to describe the physics. Hence, the poroviscoelastic (PVE) model, which assumes a viscoelastic solid phase and a viscous fluid phase, fits better [28].

1.4.2 Overview of previous studies

The friction of a large number of materials obeys Amonton's law, in which the friction force is related linearly to the normal force. The biphasic[1] nature of hydrogels differentiates them from most of the materials, leading to deviation from Amanton's law. The lubrication of hydrogels is the combined outcome of the mechanics, fluid lubrication, and surface properties. So far, there is no general theory concerning the relationship between hydrogel mechanics and frictional behavior. Such a discrepancy arises from the complexity of the friction in biphasic

[1] In this context, the word biphasic refers to hydrogels with a mobile phase (water) and immobile phase (polymer matrix). The mobile phase itself can be categorized as the free water and the bound water. In hydrogels, there are obviously no phase boundaries. This is sloppy use of the term. However, this term is commonly used for hydrogels in literature.

systems, where mechanical properties are controlled by parameters such as deformation rate, applied load, permeability, confinement, and contacting surfaces (i.e., hydrogel-hydrogel contact or hydrogel-stiff slider contact).

Gong *et al.* described the frictional behavior of a hydrogel sliding against a solid countersurface by a repulsion-adsorption model based on a polymer-solid interfacial interaction (Figure 1-22) [100,101]. If the interaction of the polymer network and the solid surface is repulsive, the polymer network will be repelled. Contrary to this, the polymer network will be adsorbed to the solid surface if the interaction is attractive. In the repulsive case, the friction is due to the lubrication of the hydrated water layer of the polymer network at the interface, which predicts that the friction should be proportional to the sliding velocity. In the attractive case, the friction of a gel is caused by elastic deformation of the adsorbing polymer chain and lubrication of the hydrated layer of the polymer network. The first contribution is the same as the adhesive friction [100].

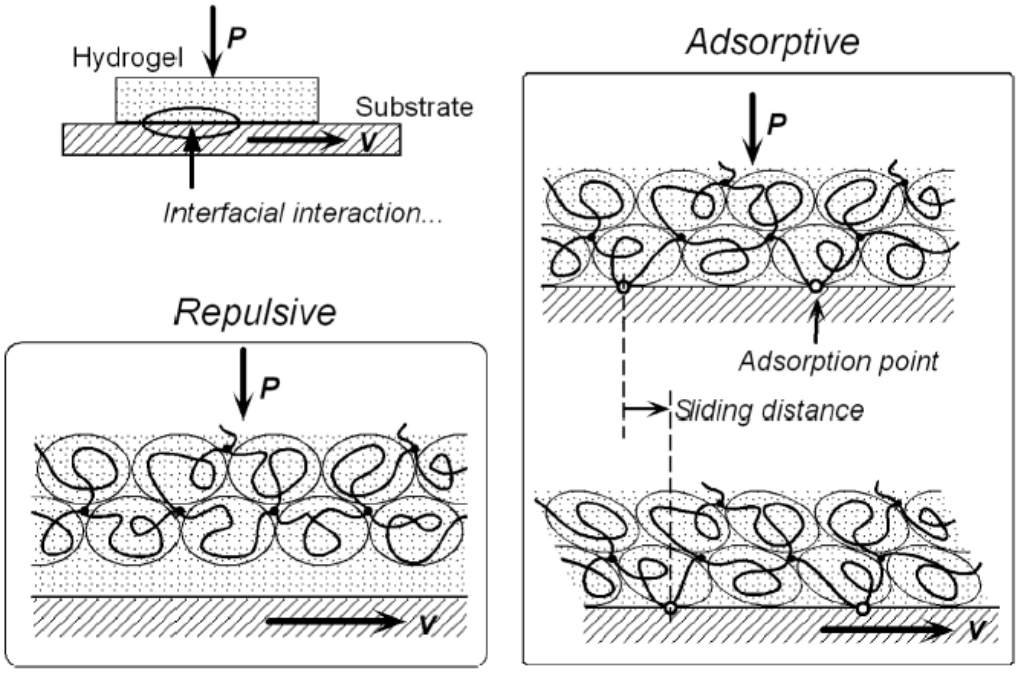

Figure 1-22 Schematic presentation of the repulsion-adsorption model for a hydrogel in contact with a solid countersurface [100].

In the adhesive interaction case, the friction originates from the surface adhesion and hydrated lubrication. Surface adhesion is dominant at low sliding velocities, and hydration lubrication becomes the major mechanism at high velocities. Plotting friction as a function of sliding speed, gives an S-shape curve as illustrated schematically in Figure 1-23. Indeed, in this

curve, a transition in friction is observed which depends on the mesh size and polymer relaxation time. For a repulsive configuration, the friction is mainly due to lubrication by the hydrated water layer. The friction shows a monotonic increase with the sliding velocity arising from its hydrodynamic nature [102].

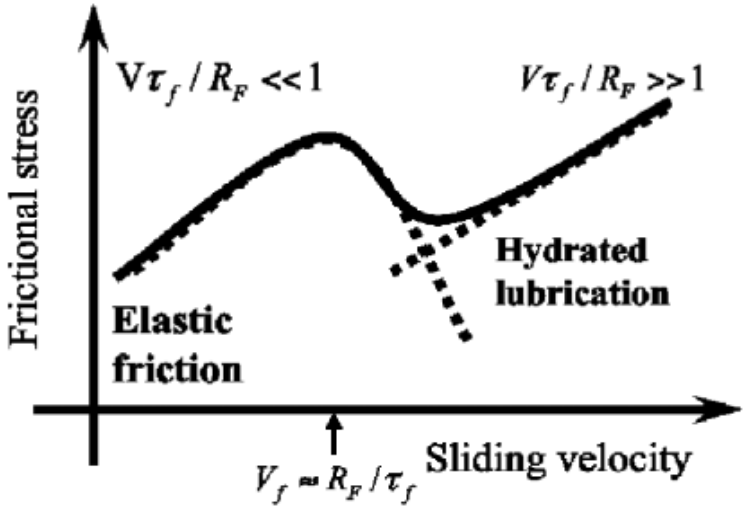

Figure 1-23 Schematic curve for the friction of a gel that is adhesive to the opposing surface [102].

The frictional behavior of gels is determined by the nature of the two opposing surfaces [88,103]. Dunn *et al.* explored three types of contact: (1) a hemispherical glass slider moving across a flat hydrogel (migrating contact), (2) a hemispherical hydrogel slider sliding on a flat glass (stationary contact), and (3) a hemispherical hydrogel against a flat hydrogel countersurface. It was shown that the coefficient of friction in the migrating contact is strongly speed-dependent but weakly time-dependent. For a situation with stationary contact, the friction coefficient is strongly time-dependent but weakly speed-dependent. In contrast to the previous two cases, the self-mated interface has a lower dependence on sliding speed and time [88,104].

It was suggested that for the "*Gemini*" (self-mated) interface the contact contains significant interfacial water. The contact area is determined by permeability and the elastic modulus, both of which are mainly controlled by the mesh size of the hydrogel network [88,89,104,105]. The mesh size controls how fast water can be pushed through the network under a given load and defines the elasticity of the gel. The significance of the polymer mesh size in determining the friction of the "*Gemini"* hydrogel interface leads to mesh-confined lubrication, in which mesh size is the single parameter influencing the lubrication behavior [89].

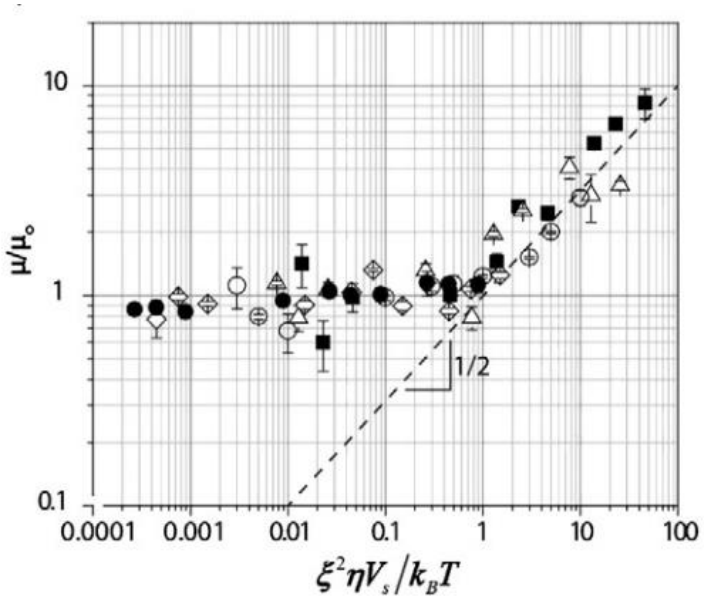

Figure 1-24 Friction coefficient as a function of sliding speed for five different polymer mesh sizes collapsing in a single universal curve that illustrates the transition in friction behavior from the speed-independent to the speed-dependent friction regime. In this curve coefficient of friction is divided by the friction coefficient in the speed-independent regime (μ_0) [89].

In a series of experiments by changing the mesh size of the polymer and sliding speed, it was found that larger mesh size results in lower friction coefficients. Moreover, friction coefficients were lowest for the slowest sliding speeds. In a hydrogel, the polymer relaxation time is given by eq. (1-14) [89]:

$$\tau = \frac{\xi^3 \eta}{k_B T} \qquad (1\text{-}14)$$

where ξ is the polymer mesh size, η is the viscosity of water, k_B is the Boltzmann's constant, and T is the temperature [35]. As can be seen from the friction tests, the coefficient of friction appears to be speed independent at slow sliding speeds. At a transition speed, the COF starts to increase by increasing the sliding speed. It has been suggested that the transition occurs when the relaxation time (τ) is equal to the time it takes for the surface polymer chains to go over one mesh size. Thus, the transition speed can be calculated by replacing τ in eq. (1-14) with ξ / v^*. Then, the transition speed is $v^* = \frac{k_B T}{\xi^2 \eta}$. When the sliding speed is rescaled using the transition speed by dividing sliding speed (v_s) by the transition speed (v^*), the resulting x-axis will be a dimensionless number. The dimensionless number is shown in the x-axis of Figure 1-24. The y-axis is normalized by dividing all the COF values by the COF in the speed-independent

regime (μ_0). After normalizing the data from the samples with different mesh sizes, all datasets collapse to a single curve [89].

1.4.3 Surface roughness and frictional properties

Pitcher of the carnivorous plant Nepenthes is an example of a textured slippery surface in nature that has evolved organs for attracting, capturing and digesting small animals. Studies on the surface morphology of peristome revealed that it carries regular microstructures consisting of radial ridges, which is shown in Figure 1-25 [106]. A homogeneous liquid film wets the surface of the peristome and makes it slippery for insects so that the prey slides into the pitcher [8,106]. Previous studies have illustrated that surface topography, when combined with water, is the main parameter to reduce the attachment of insects on plant surfaces [8]. The surface roughness in articular cartilage is also reported to play an important role in the healthy performance of this tissue [107].

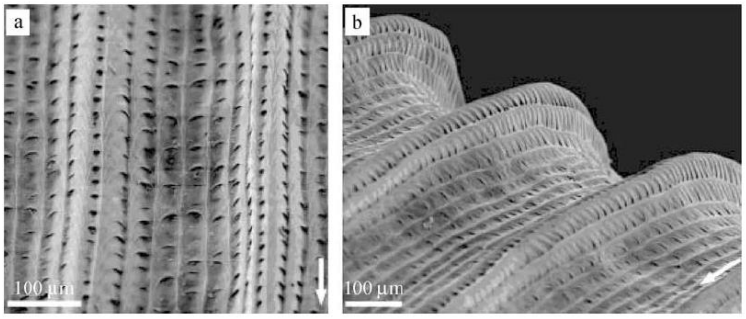

Figure 1-25 SEM images of peristome showing radial structures toward the pitcher [106].

Inspired by the examples available in nature, Yashima *et al.* have investigated the influence of surface roughness on the friction of hydrogels [108]. Samples with various surface roughness (2 µm, 4 µm, 9 µm, and 21 µm) have been achieved by glass templates with specific surface roughness. Frictional resistance between the samples and glass has been measured by changing the sliding speed.

According to the experimental results shown in Figure 1-26, hydrogels with rough surfaces show higher friction in comparison to the one with a flat surface [108]. The friction of samples with rough surfaces reduces with velocity, while the flat sample exhibits an elastohydrodynamic (EHL) transition.

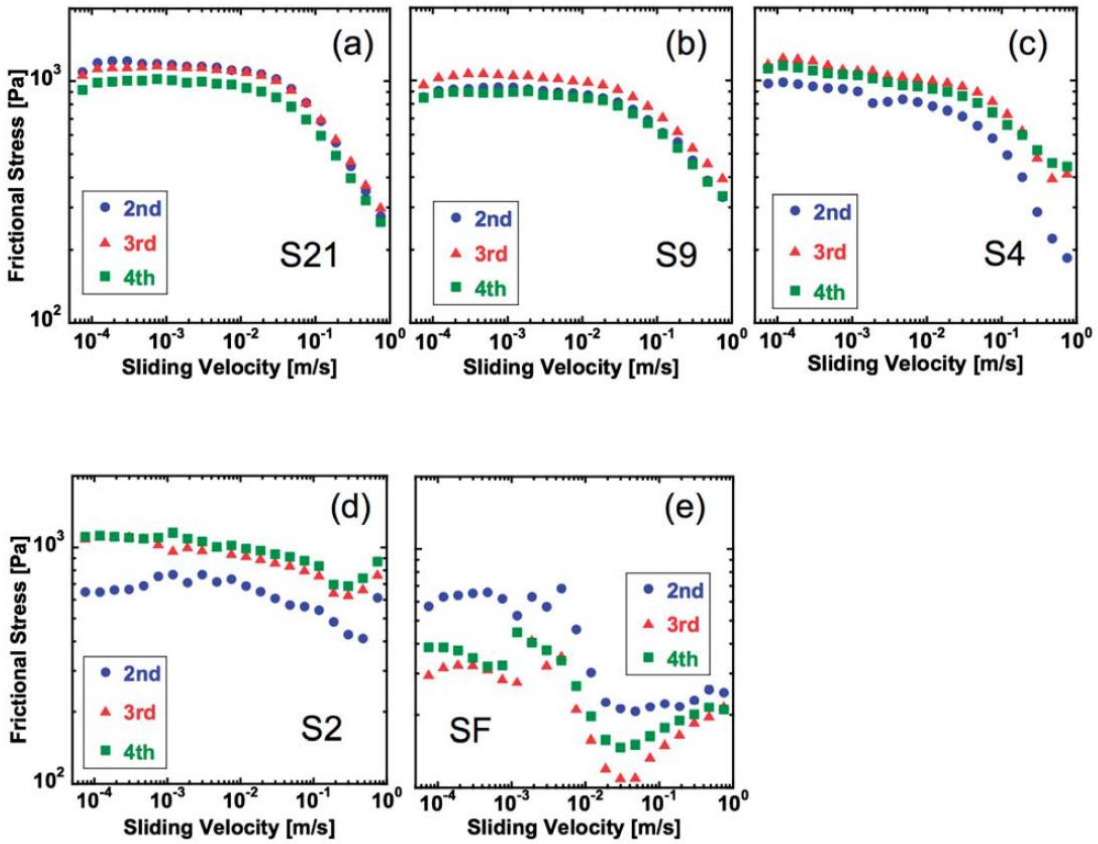

Figure 1-26 Frictional stress as a function of sliding speed for samples with different surface roughness a) 21 µm b) 9 µm c) 4 µm d) 2 µm and e) flat sample [108]. The three different colors on the plots show the 2nd, 3rd , and 4th test results on each sample.

Initially, lower friction is expected for rough hydrogels as a result of a smaller contact area; however, the observations contradict this assumption. In this study, observations by confocal laser microscope showed that a thin water layer is trapped in the case of a flat sample due to heterogeneous dewetting, although water can drain easily when the surface is rough. Additionally, the apexes of rough samples can make direct contact with the glass surface and result in high friction [108].

1.5 Surface-attached hydrogels

Surface modification is a method widely used to get desirable properties and functionalities on surfaces. Surface treatments can be achieved by different processes to change the surface energy of the material, adhesion, wetting, absorbing, or releasing properties. Methods such as deposition and lamination usually give noncovalently bonded coatings that are prone to wear over time [109]. Surface properties modification might be achieved by tailoring surface roughness by means of abrasion or sandblasting even though these methods

result in surface damage that introduces micro-cracks. Surface activation via atom bombardment, plasma treatment and laser treatments operating costs are very high [74]. Thus, attaching the thin polymers layers to a solid substrate is highly desirable to modify surface properties and enhance the stability of the thin layers [110]. One of the main problems associated with hydrogels is the adhesion between the deposited layer and the substrate, as these layers swell in contact with water. Upon swelling, shear stress will be induced within the plane of the surface and cause delamination. To solve this problem, the hydrophilic polymer chains can be covalently anchored to the substrate surfaces [111].

1.5.1 C, H-Insertion Crosslinking (CHic)

C, H insertion crosslinking (CHic) is a novel crosslinking method in which crosslinking and covalent attachment to the substrate occur simultaneously, as reactive groups are incorporated into polymer chains by a copolymerization reaction. When the substrates do not have C-H groups, prior to polymer deposition and grafting self-assembled monolayers such as silanes, thiols, and phosphonates are formed that can bind to the reactive groups present on glass, silicon, gold, aluminum, and titanium surfaces [111]. The copolymer containing reactive groups can be deposited on substrates by different coating methods such as for example, dip coating, spin coating, and doctor blading. The reactive groups of the copolymer can be activated either thermally or photochemically, as illustrated in Figure 1-27 [111]. A very common reactive group to be used in the CHic reaction is the benzophenone unit. Benzophenone groups are easy to incorporate into the polymer and upon UV activation, they can be excited to a biradicaloid triplet state, which has a very long lifetime and leads to a straightforward crosslinking reaction[110].

4-methacryloyloxy benzophenone (MABP) photoactive groups were frequently copolymerized with N,N-dimethyl acrylamide. After UV irradiation, the active groups generate biradicals and abstract hydrogen from nearby C-H groups depicted in Figure 1-28. The generated carbon radicals can recombine with either neighboring polymer chains or the substrate forming a network that is attached to the substrate. As the crosslinker content is increased, the swelling ratio of the network is reduced, which is caused by the hydrophobic nature of the crosslinker and the increased crosslinker density[110–113].

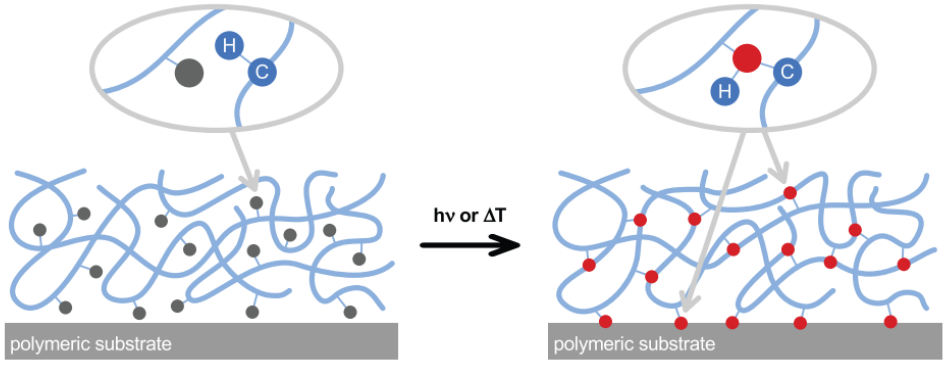

Figure 1-27 Schematic presentation of a C-H insertion crosslinking reaction [111].

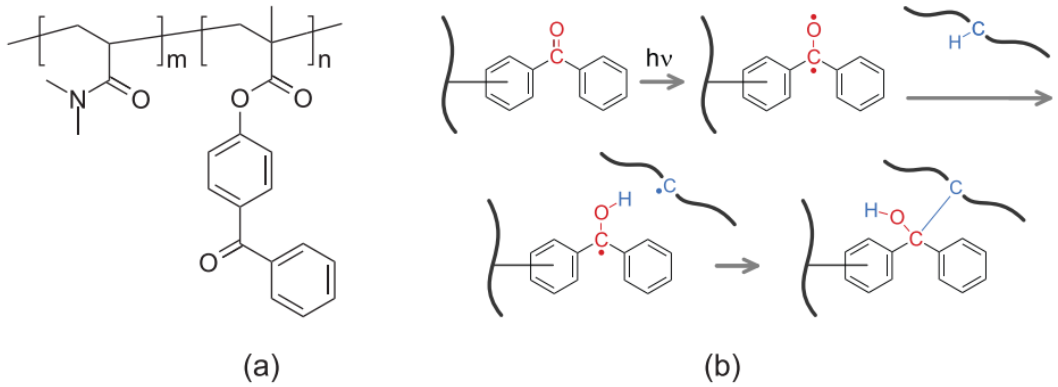

Figure 1-28 (a) Chemical composition of poly(dimethyl acrylamide)-co-MABP. (b) C,H insertion reaction of polymers with benzophenone [111].

1.5.2 Anisotropic swelling of surface-attached networks

The most important feature of surface-attached polymer networks is their anisotropic swelling, as they are covalently bonded to the substrate. Swelling can only happen normal to the substrate due to their limited thickness compared to surface substrate dimensions. A relationship has been proposed by Toomey *et al.* as a modification of the model by Flory-Rehner theory to estimate swelling of surface-attached hydrogels by knowing the swelling of unconstrained ones. For a one dimensional system, swelling is as given in eq. (1-15) [114]:

$$\alpha_s = \frac{h_2}{h_1} \qquad (1\text{-}15)$$

Here α_s is the swelling ratio perpendicular to the surface. h_2 and h_1 represent the film thickness in swollen and dry state, respectively.

An unconstrained polymer network can swell isotropically in all dimensions, meaning swelling ratio is equal in all directions ($\alpha_x = \alpha_y = \alpha_z$), where α_i is the linear increase in length in the i direction. Hence, the volumetric swelling (S) is equal to ${\alpha_s}^3$. It was found that the surface-attached networks swell less than the unconstrained gels at the same crosslinker content. Using the volumetric swelling degree (S), which is ${\alpha_s}^3$, the degree of equilibrium swelling for unconstrained (α_{uc} and S_{uc}) and surface-attached (α_{sa} and S_{sa}) polymer network can be obtained by the following equations:

$$\alpha_{uc} \approx \left(\frac{1}{\varphi_0 N_c}\right)^{-\frac{1}{5}} \qquad S_{uc} \approx \left(\frac{1}{\varphi_0 N_c}\right)^{-\frac{3}{5}} \tag{1-16}$$

$$\alpha_{sa} \approx \left(\frac{1}{\varphi_0 N_c}\right)^{-\frac{1}{3}} \qquad S_{sa} \approx \left(\frac{1}{\varphi_0 N_c}\right)^{-\frac{1}{3}} \tag{1-17}$$

In eq. (1-16) and (1-17), N_c is the number of segments between crosslinks and φ_0 represents the volume fraction of unswollen polymer occupied in the prepared state.

The linear swelling degree of surface-attached networks depends more on the crosslink density compared to the unconstrained network. Accordingly, the surface-attached networks experience higher osmotic pressure, which is partially relieved by further stretching in its swelling direction perpendicular to the surface, thus leading to a higher linear swelling than the unconstrained network. From equation (1-16) and (1-17), the relation between the volumetric swelling degree of surface-attached and unconstrained network can be predicted by eq. (1-18):

$$S_{sa} = S_{uc}^{5/9} \tag{1-18}$$

2 Goals and concept

Synovial joints exhibit low friction under varying load conditions and can undergo millions of loading cycles without wear and failure [5,30]. In joints, both countersurfaces (i.e., bones) sliding against each other are covered by cartilage, which is a soft cushion-like tissue [23,30,87]. The spectacular frictional properties are due to an interplay between the cartilage and the synovial fluid. Articular cartilage, although being complicated in its structure, is a two-component material consisting of a soft matrix and interstitial fluid (mainly composed of water).

Previous studies on lubrication of surfaces bearing charged brushes show that these surfaces can provide extremely low friction [71]; however, charged brushes are susceptible to fragmentation of the chains through "entropic death" [67,115], so that they can be detached from the substrate [23]. Additionally, thicknesses of brushes are rather small compared to the size of typical roughness features, which results in limitations in the application of brushes as lubricants.

Hydrogels are composed of a flexible polymer matrix and a high percentage of water, which is very similar to articular cartilage. In many studies, it has been shown that swollen hydrogels with high water content can result in well-lubricated surfaces. In spite of the many studies on the tribology of hydrogels, the lubrication mechanism is not currently fully understood. The lubrication of hydrogels cannot be explained by the conventional Stribeck curve [116], as they consist of an immobile polymer network and a mobile fluid moving through (and out of) it ("biphasic nature") [117]. Influence of load and sliding speed onto the frictional properties has been investigated extensively, although leading to considerable discrepancy both in the experimental results and in the interpretation of the data [101,118,119]

One of the reasons for such inconsistency is that most of the previous studies have been carried out between a hydrogel sample and a solid impermeable slider [117,120–124]. In such a case, the interaction between the two opposing surfaces and chain entanglement between subchains of the swollen polymer networks may play a significant role. Therefore, it is expected that the friction behavior of two identical hydrogel surfaces sliding against each other will differ largely from that of a solid slider sliding on a swollen gel. In more recent cases, friction systems have been studied, where the surfaces sliding against each other are both covered with hydrogels [88,89,104,105,116]. It has been shown that friction is indeed significantly lower when identical permeable counter-surfaces are in contact [88].

Furthermore, the frictional properties of free hydrogels cannot be compared with the constrained surface-attached ones. Major difficulties associated with soft hydrogels is their handling and stability. These problems can be eliminated by covalent bonding of the gel to a stiff substrate, which can prevent delamination of the strongly swollen layers, especially during compression and shearing. The difference between the bulk and surface-attached hydrogels arises from the dissimilarity in their swelling behavior [114]. Similar to brushes, surface-attached layers can extend only in a direction (i.e., away from the surface) normal to the substrate. Stretching away from the surfaces influences different properties of the polymer networks such as swelling behavior, mechanical properties, and whether they can be penetrated by large molecules in a contacting environment [88]. The strong configurational entropy effect prevents the interpenetration of the chains of two contacting hydrogel surfaces. Frictional properties of such layers need further investigations specifically under strong compression as the layers show extensive deswelling and the transport of water within the network during the deswelling/swelling processes plays an important role in lubrication of such a system.

The main goal of this thesis is to understand the lubrication behavior of surface-attached hydrogel coated surfaces, as understanding the lubrication mechanism is the key to future advances toward modification of the lubrication by means of hydrogels. In order to achieve this goal, we first examine different properties of surface-attached hydrogels that can influence frictional properties such as elasticity, permeability, and adhesion. To study the lubrication properties, we record the adhesion of the two layers at low loading and low shear rate and then investigate the friction coefficient at high loading (i.e., close to the pressure range occurring in synovial joints) and rather high shear rates. For surface-attached layers, the thickness is also an important parameter. Therefore, we study the influence of layer confinement, which is penetration depth to thickness ratio, by performing friction tests on different thicknesses. The lubrication mechanism of surface-attached hydrogel pairs is explained in light of the biphasic theory.

The next question that is targeted to be addressed in this thesis is if the lubrication of the surface-attached hydrogels can be altered by introducing surface patterns. Previous studies have pointed out the importance of the surface roughness on frictional properties of contacting surfaces [45,108,125]. It has been shown that the lubrication regime can be altered according to the surface roughness [108]. Thus, we investigate further whether deliberately induces surface roughness can result in changes in lubrication behavior. Presumably, reduction in the contact area and presence of the interfacial water on textured hydrogels must result in lower

friction, and therefore, better lubricating surfaces. We carry out friction tests on textured hydrogels to study the effect of pattern size, direction, and shape on the friction.

Finally, it would be interesting to move closer to the biological example (i.e., synovial joint). We want to elucidate how the properties of the aqueous phase influence friction behavior. When surface-attached hydrogel pairs are in contact, water squeezes out of the interfacial gap in contacting surfaces due to its low viscosity. Thus, we would like to elucidate whether a high viscosity solution can increase the load-carrying capacity and improve the lubrication of surface-attached hydrogels or not. The strategy followed here is to take a polymer, which is easily water-soluble PVP (poly(vinylpyrrolidone)), to increases the viscosity without adding any further interactions between the hydrogels and the solution, as PVP is a neutral polymer.

Finally, first experiments are performed to mimic the lyotropic properties of the synovial by adding molecules to the water, which can orient in the shear field. Lubricating steel surfaces using C8 (octyl β-D-glucopyranoside), which is a water-soluble and environmentally friendly substance, shed light on the very interesting lubrication properties of this substance [126]. By increasing the shear rate, the molecular alignment of the surfactants in the interfacial gap facilitates sliding. The anisotropic viscosity realizes a high load-carrying capacity but exhibits low viscosity in the shear direction [126]. Accordingly, friction tests are performed on a system with surface-attached hydrogel pairs lubricated by C8 to study if the lubrication can be further improved by applying this additive to the water.

3 Lubrication of surface-attached neutral hydrogels

3.1 Surface-attached hydrogels

In most of the systems, friction is usually generated from adhesion and deformation [49,50]. Adhesion arises from a formation of adhesive junctions between countersurfaces by van der Waals or Columbic interactions. When two highly hydrated surfaces are in contact, due to the presence of water, adhesion is substantially low. This could be one of the important reasons that twin hydrogel surfaces show profoundly low adhesion [88].

In this study, poly(dimethyl acrylamide-co–methacryloyl oxybenzophenone) is used to produce the surface-attached hydrogel layers. This polymer has been chosen as it contains photoreactive benzophenone groups. Benzophenone is inert in the absence of light and it attaches to C-H bonds in different chemical environments [110]. Detailed synthesis and sample preparation are explained in the experimental chapter.

3.1.1 Swelling properties

Bulk hydrogels can swell isotropically in all directions, whereas thin surface-attached layers can only swell in one dimension perpendicular to the substrate, as shown in Figure 3-1. Entropic barrier against entanglement and interpenetration of the chains coming from outside leads to a very low adhesion between two surface-attached hydrogels even under strong compression.

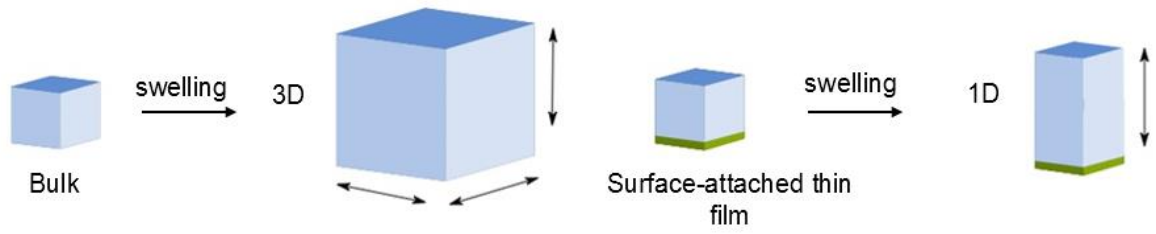

Figure 3-1 Isotropic swelling of bulk hydrogel versus anisotropic swelling of thin surface-attached layers [127].

When two surface-attached networks are brought into contact, as illustrated in Figure 3-2b, the dangling end of the chains at the interface either have to interpenetrate or deform. Strong stretching of the chains in such surface-attached systems prevents an interpenetration of the network by chains coming from the outside, especially when the network and incoming polymer exhibit no strong enthalpic interactions (e.g., Coulomb or hydrophobic interactions)

[111]. When additional chains are brought into this layer, this will force the polymer sub-chains in the network to become even more stretched and lead to an entropy loss. Such an entropy loss, however, cannot be compensated by any energy gain as the system is chosen such that enthalpic interactions are excluded. Therefore, the addition of large molecules will cause only a limited entropy of mixing, leading to the formed energy barrier, which prevents the attachment of any large molecules [111,128]. Indeed the exclusion of large molecules by surface-attached hydrogels is counter-intuitively even stronger than that of polymer brushes. In Figure 3-2a, a schematic comparison of the density profile of brushes and surface-attached networks is depicted. The segment density of brushes changes by varying grafting density and molecular weight of brushes. As the distance from the substrate increases, the segment density possesses a parabolic decay with an exponential tail. The segment density of surface-attached networks depends on the crosslinker density. In comparison to brushes, the density profile of surface-attached networks stays constant up to a larger distance from the substrate and then decreases suddenly, similar to a delta function. The very small interdigitation and delta-like segment density profile of the surface-attached polymer networks, rendering them attractive candidates for the generation of low friction surfaces [111,112,114,128].

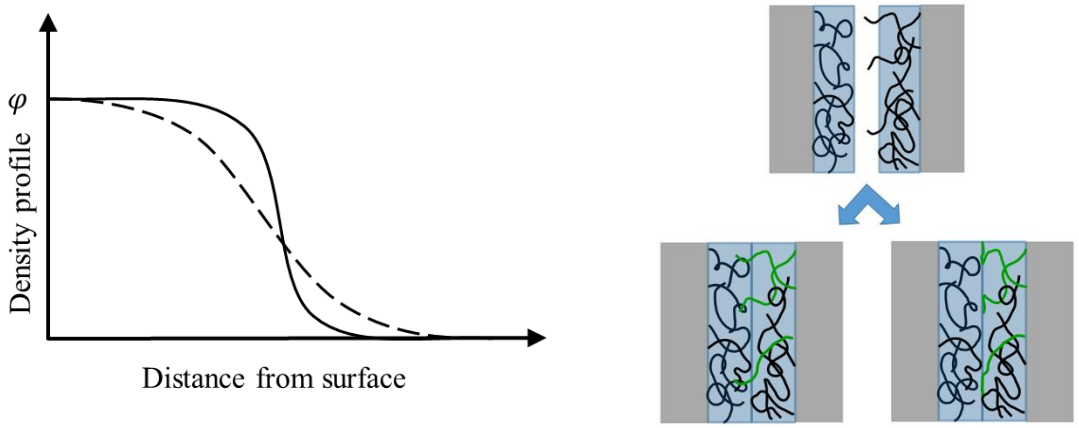

a) b)

Figure 3-2 a) Schematic comparison of the profile density as a function of distance from the surface for surface-attached hydrogels (slid line) [112] and brushes (dashed line) [23] b) Possible interaction of two surface-attached networks. Chains with dangling ends (depicted in green) either have to interpenetrate or deform.

3.1.2 Thickness measurement

The thicknesses of samples were measured by an atomic force microscope (JPK Nanowizard 4) and (Dektak XT Brucker) profilometer. For this purpose, samples were scratched to generate a step and the step height was measured. The thickness could be measured

in the dry state and in the swollen state in water by AFM in AC mode (tapping mode) when the thickness is smaller than 15 µm. An example of such a measurement is shown in Figure 3-3. The red curve and the black curve in this figure present two different cross-sections of the measured profile. As can be seen, the values in the figure are not absolute values. Therefore, the thickness has to be obtained by calculating the height difference. The dry thickness for this sample is about 11.9 µm.

Thicknesses above 15 µm were recorded using the profilometer. However, due to the contact of the cantilever of the profilometer with the sample and softness of the hydrogel samples, only dry thickness could be recorded by the profilometer. In order to avoid any damage to the sample, the force of the cantilever tip was adjusted to a low value (10 mg). The thickness was averaged over two different measurements on two different tracks. To obtain the thickness in the swollen state for a thick sample, we have used a method explained in section 3.1.3.

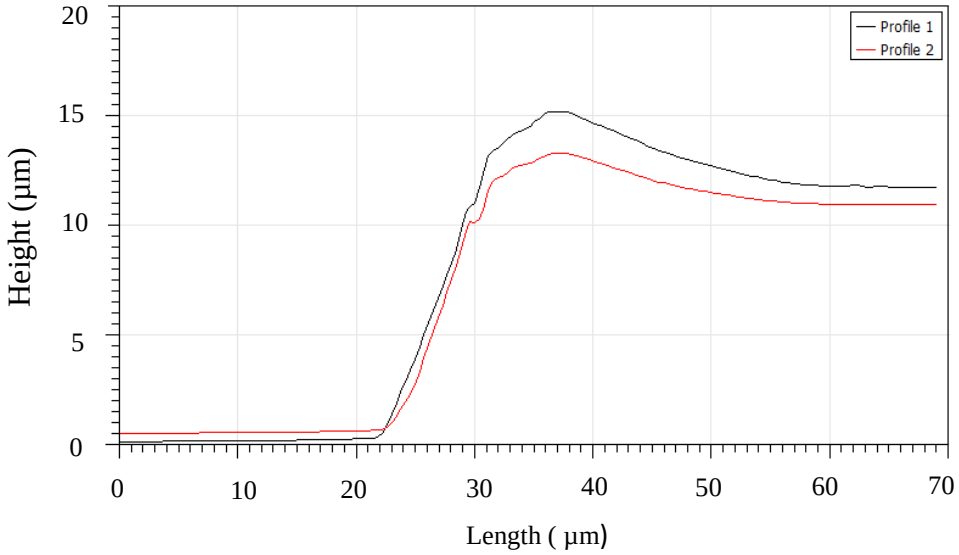

Figure 3-3 Two cross sections of the measured step height with AFM in AC mode in dry state on PDMAA-1% MABP sample. Thickness of this sample is about 11.9 µm.

3.1.3 Swelling ratio and kinetics measurement

Due to the limits that were described in the previous section, to get the wet thickness, a glass slider with a radius of 25.94 mm (Edmund optics) was brought into contact with the dry sample at a contact force of 3 mN in nanoscratch setup (CSM nanoscratch Anton Paar GmbH), as illustrated schematically in Figure 3-4. Then water is added to the dry polymer while the slider is still in contact with the dry sample surface. As the sample swells, the contact force was kept constant, so as the applied pressure thanks to the large contacting sphere, and the deflection

of the cantilever was recorded. The extent of water uptake of the network layer can be expressed by the swelling ratio, which is defined for a surface-attached gel as the ratio of the wet thickness to the dry thickness ($S = h_2/h_1$). The increase in the thickness of the sample with 13.6 µm dry thickness after adding water was 61 µm so that a wet thickness of 74.6 µm was recorded. The swelling ratio *S* for the hydrogel layer is thus *S* = 5.4. Accordingly, the amount of water in the network is given by the ratio of the change in the thickness by the wet thickness. Thus, in the present case, the hydrogel contains about 82% water. The time needed for complete swelling of the samples measured in this work was 20- 40 minutes, depending on the thickness and crosslinker density.

For the PDMAA-1%MABP, the recorded swelling ratios are ranging from 4.5 to 5.4, while this value is lower for the hydrogel with 5% crosslinker density as the crosslinker agent (MABP) is hydrophobic in its nature. Besides, the higher crosslinker contents give a network with a higher density, which has a lower swellability. The swelling ratio for PDMAA-5%MABP is about 2.5.

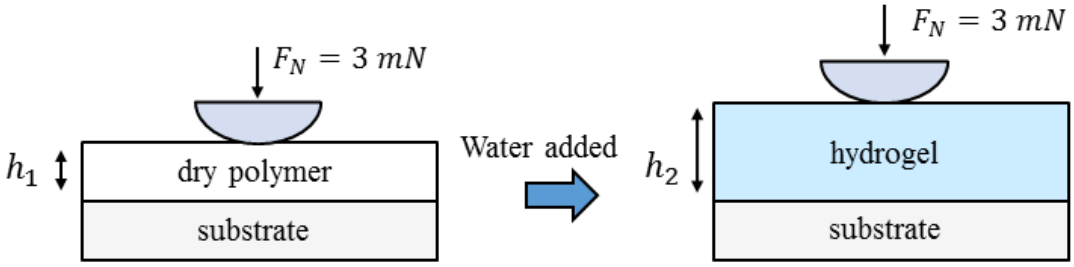

Figure 3-4 Schematic depiction of the swelling ratio measurement – the cantilever deflection is measured while the contact force is kept constant.

The swelling process of a polymer gel is a kinetic process composed of mass transport due to diffusion of water and mechanical deformation of the network [129]. During swelling, there is a competition between two forces: the force that leads to the solvation of the polymer chains (mixing energy) and the force that avoids the stretching of chains (elastic energy) [130]. Different parameters such as the polymer network structure, mechanical deformation, solvent-polymer interaction, can change the duration and intensity of the swelling process [131]. The swelling of surface-attached gels seems to be a two-step process until it reaches saturation, which can be seen in Figure 3-5. In this figure, thickness change is shown as a function of time for a sample with 10.2 µm dry thickness. Firstly, the swelling rate is almost constant (14.4 nm/s), and the thickness change continues almost linearly as a function of time. After some

time, the swelling process seems to happen faster until it saturates. The final thickness of this sample is 46.2 µm which means the swelling ratio is about 4.6. Sample with 74.6 µm thickness has a swelling rate of 16.9 nm/s. At the beginning of the swelling process, small elongation of the polymer chains can happen easily, but, further stretching becomes more difficult; however, transport phenomena becomes easier. As water diffuses into the polymer network, it creates an osmotic pressure. Initial swelling at the surface then creates space for additional water. This phenomenon might be the cause of the non-Fickian diffusion process.

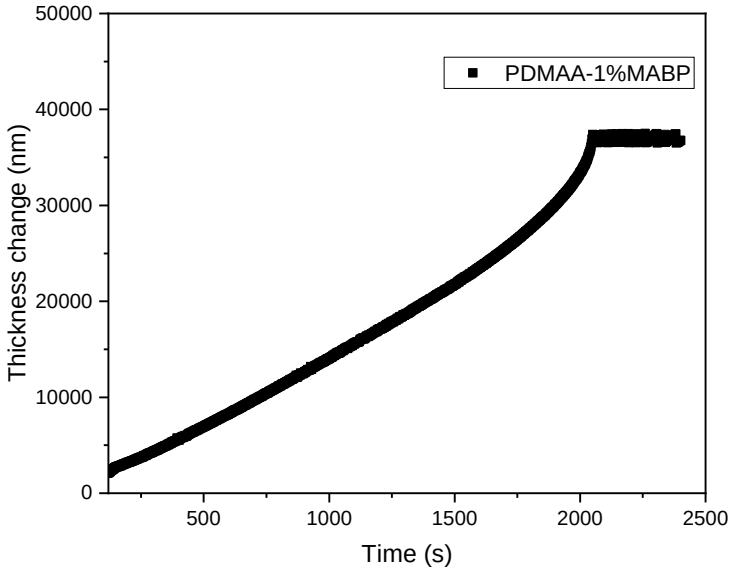

Figure 3-5 Swelling kinetics in terms of sample thickness change as a function of time for a sample with 1% crosslinker density and 10.2 µm dry thickness.

3.1.4 Surface topography of surface-attached hydrogels

One of the factors that can influence friction between surfaces is the surface topography. Some examples of such surfaces available in nature were already discussed in the introduction chapter. Therefore, it is worthwhile to study the surface topography of surface-attached flat samples. When samples are exposed to water, during the swelling process, buckling or wrinkling of the gel may take place. This phenomenon has been studied by many researchers experimentally and theoretically [132–135]. When the gel layer is constrained to a stiff substrate, it can swell freely only in the direction perpendicular to the substrate, but not in the plane of the substrate. The in-plane constraints of deformations generate the in-plane compressive stresses leading to creases and wrinkles on the surface [132–135].

We have investigated the distance and the depth of these structures using AFM and optical microscope. The results are demonstrated in Figure 3-6 and Figure 3-7, respectively. AFM images were obtained in AC mode (tapping mode) by a standard non-contact cantilever with a sharp tip (ACL-W cantilever from APPNano Company).

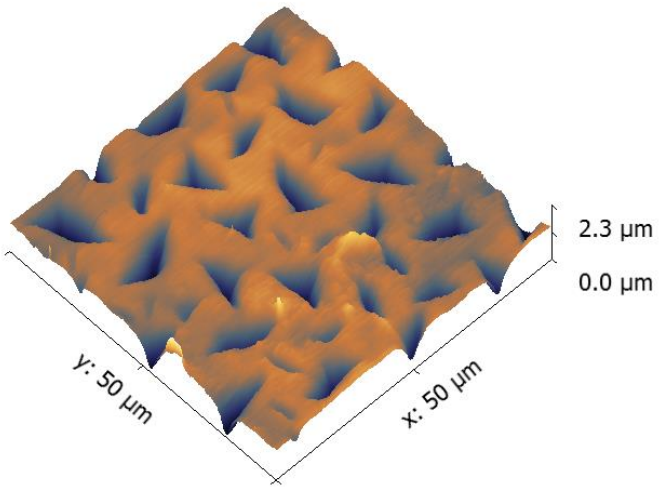

Figure 3-6 Surface profile of a sample with 10.2 µm dry thickness and 46.2 µm wet thickness obtained by atomic force microscope with the scanned area size 50 × 50 μm^2.

To study the relation between the surface wrinkling phenomenon and sample thickness, we chose six samples with different thicknesses (2.7 µm, 4.7 µm, 10.2 µm, 13.6 µm, 23.3 µm, 20.6 µm). Figure 3-7a represents the layer thickness of 2.7 µm (dry thickness) for which no wrinkles were observed. However, for the other samples, wrinkles were found on the wet hydrogel surfaces. It can be seen clearly that as the thickness increases, the wrinkles become larger and the distance between them gets larger. This observation is consistent with the proportionality of the wrinkles period and the thickness of the hydrogel layer described by Schweikart *et al.* [136]. In order to measure the periodicity of the wrinkles, the distance between two consecutive wrinkle centers was measured. The results given in Table 3-1 are the average of five measurements for each sample. Although the size of wrinkles and their distance increase for thicker samples, the depth of the wrinkles does not change considerably. The maximum depth of the wrinkles is 2.4 µm. Accordingly, when the penetration depth is larger than this value, the surface patterns are already flattened and might have a minor influence on the frictional properties.

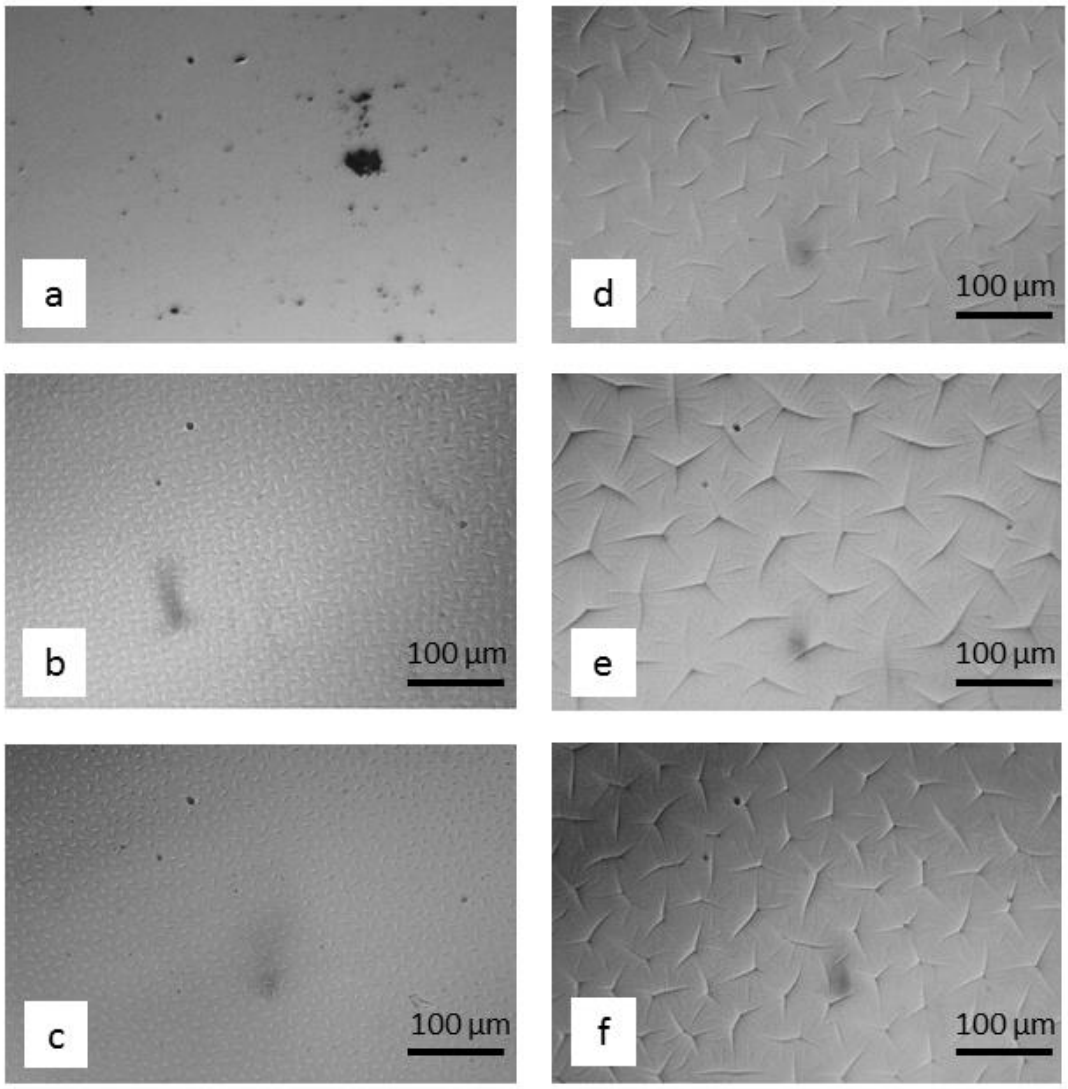

Figure 3-7 Optical images of samples with different thicknesses: a) 2.7 µm, b) 4.7 µm, c) 10.2 µm, d) 13.6 µm, e) 23.3 µm, and f) 20.6 µm.

Table 3-1 Influence of thickness on the wrinkling periodicity.

Sample	Dry thickness (µm)	Wet thickness (µm)	Wrinkle distance (µm)
b	4.7	24.5	16.8
c	10.2	46.2	14.7
d	13.6	74.6	42.6
e	23.3	96.8	62
f	20.6	98.8	52.2

3.1.5 Swelling pressure measurement

Swelling pressure is the pressure that has to be applied to the hydrogel to deswell it from the swollen state to the completely dry state or the counter-pressure when a dry polymer starts to uptake water and becomes swollen. To measure this pressure, we carried out a compression test using a tensile test machine (Zwick Z 2.5 (Zwick GmbH, Germany)). The principle of the measurement setup used for this experiment is depicted in Figure 3-8a. The compression rate was kept very small (60 µm/min) to eliminate the effect of flow rate on our measurement and make sure that the gel is equilibrated during compression.

As a reference, the compression test was performed without the hydrogel sample to record the internal friction of the syringe. This value was then subtracted from the force we recorded while compressing the gel.

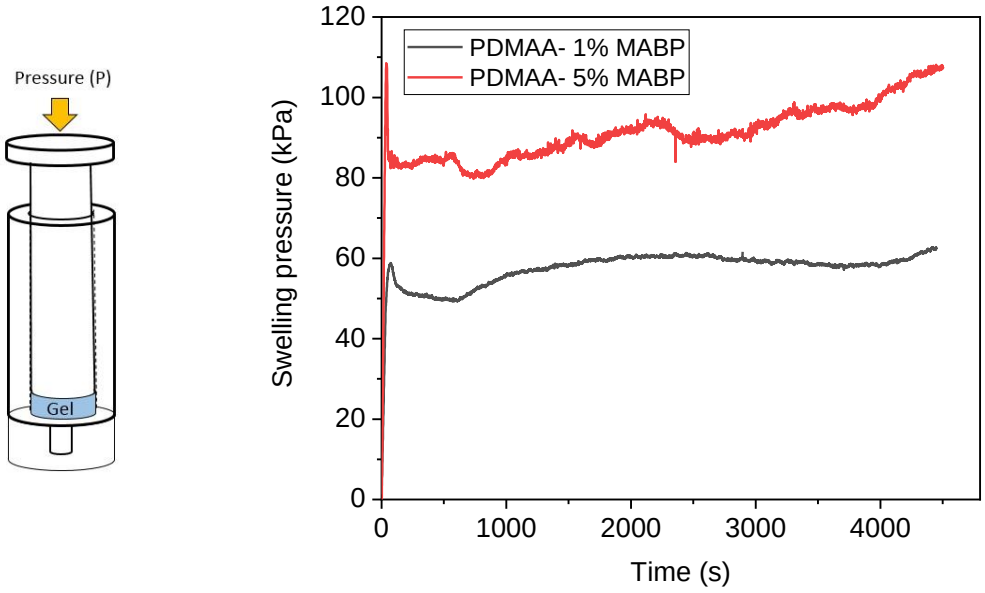

a) b)

Figure 3-8 a) Swelling pressure measurement setup, a syringe compressing the fully swollen gel up to the dry state thickness b) Swelling pressure of PDMAA-1% MABP and PDMAA-5% MABP as a function of time.

Since thick samples are required for the swelling pressure experiment, bulk hydrogels were prepared by molding the polymer solution in a PTFE mold. The thicknesses were measured in the dry and fully swollen states. The hydrogel samples were fully pressed until their thickness reached the dry state thickness. During the test, the sample was compressed at a constant speed, and the pressure to squeeze out the water was recorded. In Figure 3-8b, the

results of the swelling pressure experiment are presented for two different crosslink densities. Swelling pressure was about 60 kPa and 90 kPa for PDMAA-1% MABP and PDMAA-5% MABP, respectively. The hydrogel with higher crosslinker density showed higher swelling pressure; however, the difference is only about 30 kPa. It must be taken into account that the samples used in the swelling pressure experiments were bulk hydrogels, which must differ from the surface-attached ones.

3.2 Indentation tests for elastic modulus measurements

Nanoindentation tests are usually performed to extract elastic modulus and hardness of the specimen material from load-displacement curves. Load-displacement curves are obtained by recording force and penetration depth as the load is applied from zero to a maximum force and then from maximum force back to zero [59].

To determine the elastic modulus of our hydrogel samples, an atomic force microscope (JPK Nanowizard 4) was used in contact mode (force mapping mode). The AFM cantilevers (CP-CONT-PS-A) used in these measurements were ordered from NanoAndMore Company. Colloidal cantilevers have a polystyrene bead with a diameter of 1.98 μm attached to them. Sharp cantilever tips might induce local strains that far exceed the linear material regime and ultimately might even plow into the gel. Due to the smallest stress and strain concentrations, a spherical indenter geometry was preferred. Moreover, the spherical indenter was needed to reduce the penetration depth and thereby minimize any substrate effects on the measured elastic moduli. All the indentation tests were carried out in water. The obtained sensitivity and spring constant from the calibration of the cantilever was 33.2 nm/V and 0.42 N/m, respectively.

Figure 3-9 illustrates a typical force-distance curve. As can be seen, when the cantilever is far from the surface, there is no interaction force. As it approaches the sample, electrostatic forces and long-ranged interactions may occur. As the tip gets very close to the surface, van der Waals and capillary forces start to act on the cantilever. If the interaction is strong, the cantilever may jump into contact and finally start to penetrate the sample where interactions become repulsive. As the cantilever is retracted from the surface, a pull-off effect due to adhesion could be observed. Finally, the interaction force will become zero as the tip gets further from the sample surface. In our measurements, since all the system is immersed in water, there is no capillary force.

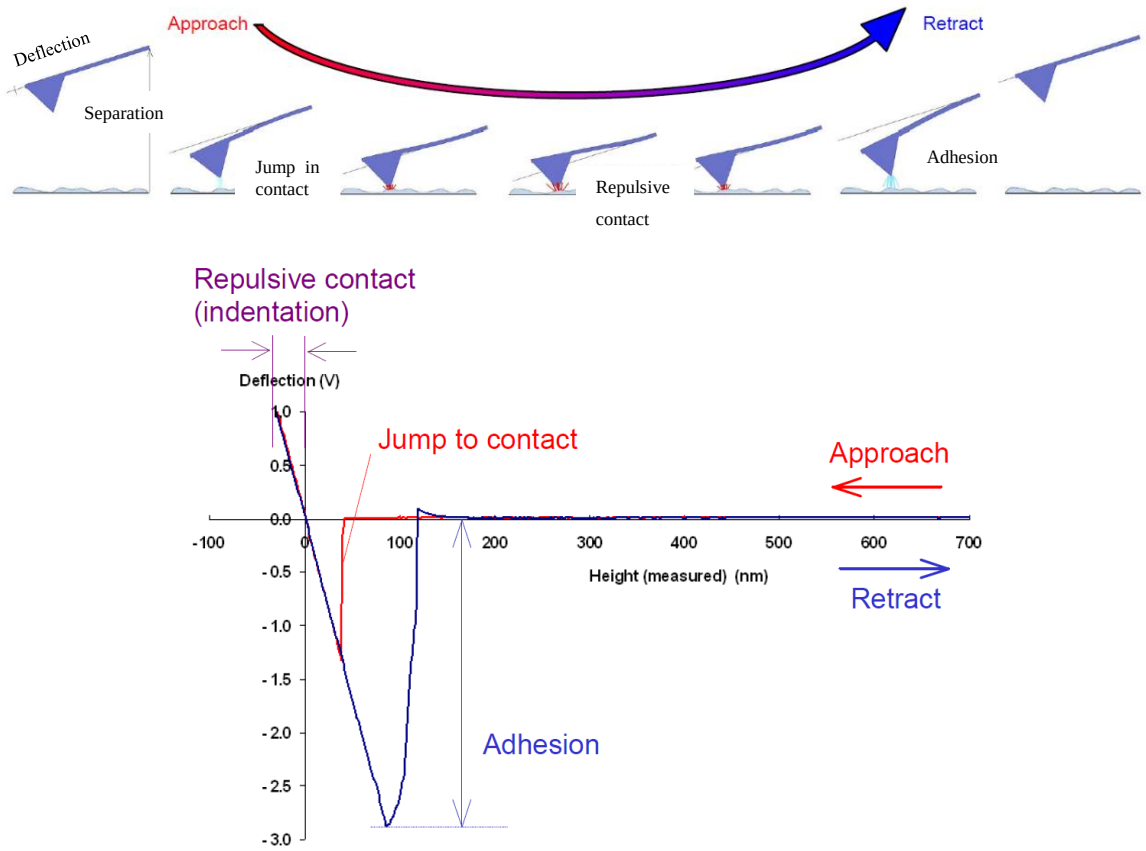

Figure 3-9 Typical tip-sample interaction and resulting force-distance curve [137].

3.2.1 Influence of confinement on elastic modulus measurement

In a homogeneous material, one expects to measure only one value of an elastic modulus, although, for several reasons, experimental results may result in a variation of the modulus with indentation depth. For the measurement of the elastic modulus, any indentation will result in some influence from the substrate, since the elastic deflections of both the substrate and the film contribute to support the load. However, because of the localized nature of the indentation stress fields, more support comes from the film than the substrate. It is best to perform a series of indentations from a very low load to a reasonably high load and then plotting modulus versus indentation depth. Extrapolation to a plateau at shallow indentation depth should result in a value of modulus for the film [138].

For thin surface-attached layers, the stiff substrate can influence the elastic modulus measurements as well. The depth of the zone, which is influenced by the applied stresses, is called relaxation depth (presented in Figure 3-10). When the relaxation depth is smaller than

the thickness ($\delta_r < h$), no thickness dependence of the elastic modulus should be observed. The relaxation depth larger than the thickness ($\delta_r > h$) leads to higher apparent modulus. If the sample is thick enough in comparison to the penetration depth, compressed layers can relax properly. However, in a thin layer, the deformed network does not have the chance to relax properly. In order to avoid any influence of thickness, the indentation test was performed on the thickest sample with a wet thickness of 74.6 µm by applying a very small load of 5.5 nN. Indentation speed was also kept small (1 µm/s) so that there is no effect of water flow during the indentation tests. As the contact area is very small and indentation speed is low, we assume that the sample is in a relaxed state during the indentation.

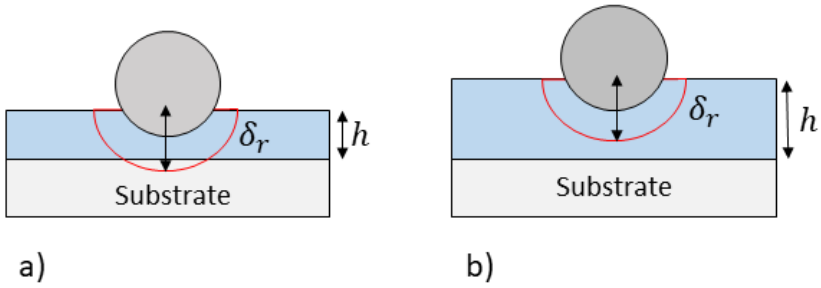

Figure 3-10 Relaxation depth in comparison to the thickness of the hydrogel layer. a) Relaxation depth larger than thickness b) Relaxation depth smaller than thickness.

Force-indentation curves were recorded on three different spots of each sample on an area of 100×100 µm^2. For each spot, 64 force-distance curves were recorded. An example of a force curve for PDMAA-1%MABP with 74.6 µm thickness is given in Figure 3-11. As can be seen, the approach and retract curves overlap, indicating a completely elastic behavior. The elastic modulus was obtained by fitting the Hertz equation to the force-indentation curve since no adhesion occurs and the behavior is elastic. The indentation depth for the measurement shown in Figure 3-11 is about 250 nm, which means the penetration depth is only around 0.3 % of the thickness. In such a small penetration depth, the influence of the substrate should be negligible. The average measured elastic modulus for PDMAA-1%MABP with a 74.6 µm thickness is 49 $\pm$ 20 kPa.

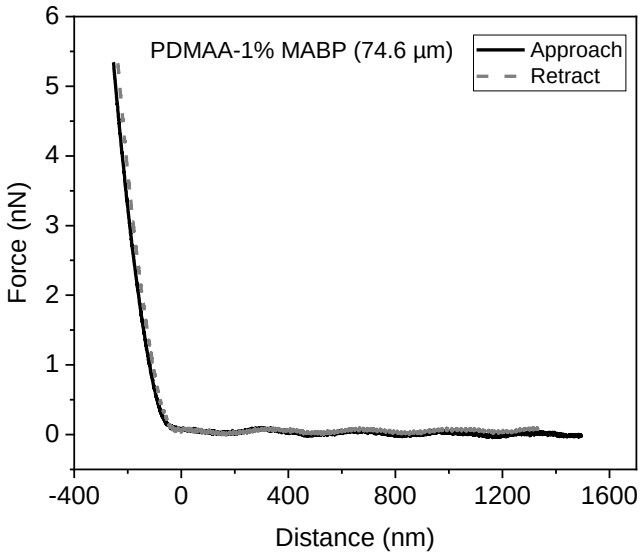

Figure 3-11 Force-distance curve from indentation test by AFM on a sample (PDMAA- 1% MABP) with 74.6 µm wet thickness.

In order to investigate how the substrate may affect the measurement of elastic modulus, a stiffer colloidal cantilever (CP-NCH-PS-C-5 NanoandMore GmbH) with a spring constant of 42 N/m is used so that the indentation test can be performed at higher penetration depths. For this purpose, indentation tests were performed on a thin sample (10.8 µm), which provides the possibility to check the influence of high confinement. As the thickness of the sample is reduced, the force required to indent up to a specific depth increases and consists of the apparent stiffening effect classically observed. In Figure 3-12, the apparent elastic modulus was given as a function of applied load and penetration depth. When penetration depth to thickness ratio (confinement) is below 3%, no influence of substrate was observed. However, the effect becomes prominent after this point, and the measured elastic modulus is higher than the elastic modulus of the hydrogel itself. For penetration depth above 300 nm, the apparent elastic modulus increases as the indenter penetrates further. As the confinement reaches 0.1, the apparent elastic modulus increases to around 3 MPa.

It should be noted that the Hertz theory assumes a half-space elastic bodies in contact with a flat surface. Figure 3-12 evidences a clear deviation from Hertz theory in case of confined thin samples since the substrate stiffness influences the relationship between the indentation depth and stress field. The few theoretical models available for finite thickness samples in literature are inconvenient because they require extensive numerical computations due to the geometric nonlinearity. The complication of these models avoids their use for routine analysis of force-displacement curves [139]. An example of these theoretical models is given in eq. (3-

1), where Green's function is derived for a thin sample bonded to the substrate. This function is used to estimate indentations. Finally, the integral equations are satisfied by a computed, effective pressure profile acting on the Hertzian contact area [139].

$$F = \frac{16E}{9} R^{1/2} \delta^{3/2} \left[1 + 1.133 \frac{\sqrt{R\delta}}{h} + 1.283 \left(\frac{\sqrt{R\delta}}{h}\right)^2 + 0.769 \left(\frac{\sqrt{R\delta}}{h}\right)^3 + 0.0975 \left(\frac{\sqrt{R\delta}}{h}\right)^4 \right] \quad (3\text{-}1)$$

The term outside the bracket in the above equation is the Hertz solution and the terms inside the bracket are the corrections required for a confined sample. However, in this equation, it is assumed that the maximum strain does not exceed 10% ($\delta < 0.1\ h$), where material still has linear behavior [139].

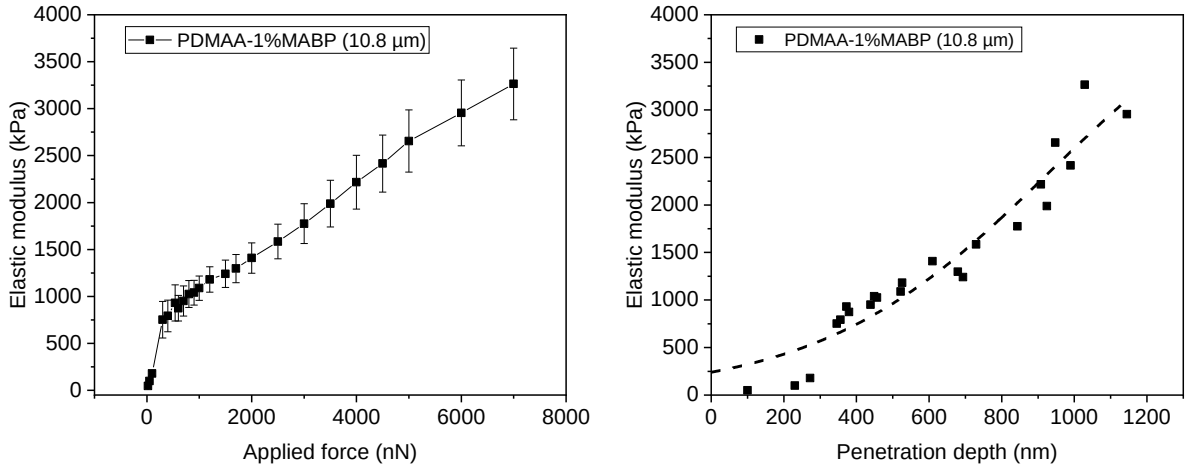

a) b)

Figure 3-12 Influence of confinement on measured elastic modulus a) Measured elastic modulus as a function of applied load in the indentation test by AFM b) Measured elastic modulus for different penetration depths.

The indentation tests on the thin sample (10.8 µm) show that for small indentation depth (below 3 % of the thickness), there is no influence of the substrate. During the indentation test on the thick sample with a thickness of 74.6 µm, the indentation depth was about 0.3 %, which is ten times smaller than the measured threshold. Therefore, the measured elastic modulus for this sample (49 ± 20 kPa) can be considered as the elastic modulus of the hydrogel with 1% crosslinker density.

3.2.2 Influence of crosslinker density on elastic modulus

The mechanical behavior of a hydrogel strongly depends on the strength of bonding. Hydrogels with covalent bonding tend to show elastic behavior, as the crosslinks hold the polymer chains tightly together while hydrogels with secondary bonds show a viscoelastic behavior due to the mechanism of breaking and rearrangement of the crosslinks. Thus, the type and density of bonding between the polymer chains can significantly influence the properties of the resulting hydrogel.

The influence of the crosslink density on the compressive behavior was investigated by applying 5 nN load with a colloidal probe of AFM on samples with similar thickness around 70 µm but different crosslinker contents (0.5%, 1%, and 5%). It can be seen from the force-distance curves shown in Figure 3-13, the sample with higher crosslink density is more difficult to compress, so the indentation depth gets smaller for the given applied load by increasing the crosslinker density. Higher crosslinker density results in a denser network, which means the distance between the crosslinks is shorter (smaller mesh size). An increase in crosslinker density results in higher polymer volume fraction and lower water content/swelling ratio. As a result of the smaller mesh size, the mobility of the polymer network and bound water decreases, consequently, that the hydrogel becomes stiffer.

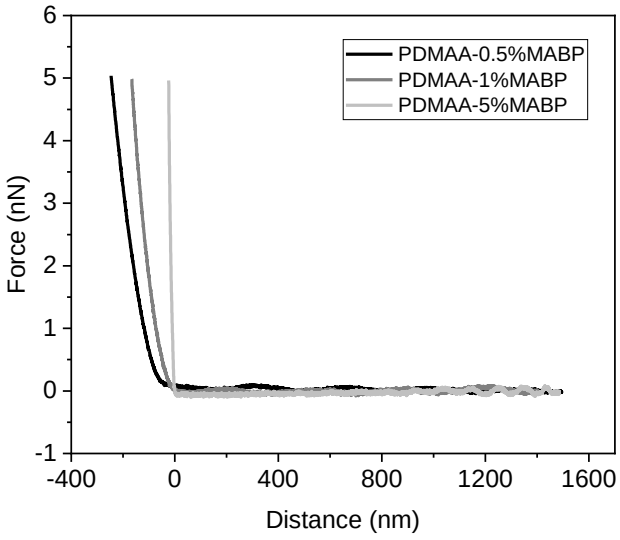

Figure 3-13 Force-distance curve obtained from AFM indentation tests for three different crosslinker densities (0.5%, 1% and 5% MABP). Samples have similar thicknesses around 70 µm.

Elastic modulus obtained from indentation tests by AFM for the three crosslinker densities are given in Table 3-2. Comparing measured elastic moduli for different crosslinker densities shows that five times increase in the amount of crosslinker leads to an elastic modulus which is 8 to 10 times stiffer. For a semi-dilute hydrogel composed of flexible polymers, the elastic modulus is proposed to scale with the network mesh size as $E \sim \xi^{-3}$ [140,141]. The ratio of the mesh size for 1% and 5% crosslinker density can be calculated from the ratio of swelling ratios measured in section 3.1.3. This ratio predicts an elastic modulus of the 5% MABP that it is eight times higher than that of 1%MABP. Consequently, mechanical and transport properties of hydrogels can be easily tuned through adjusting the ratio of monomers and crosslinker units. The relatively high scattering of the measured elastic modulus can be the result of inhomogeneous distribution of the crosslinker.

Table 3-2 Elastic modulus of hydrogels with three different crosslinker densities.

Polymer	**Elastic modulus**
PDMAA-0.5% MABP	38.4±9 kPa
PDMAA-1% MABP	49.2 ±20 kPa
PDMAA-5% MABP	734.1±296 kPa

3.3 Pull-off test

As was discussed in chapter 1, adhesion plays an important role in high friction of surfaces. Therefore, it is of great significance to study adhesion between surfaces before investigating friction. The pull-off force is the force needed to separate two surfaces. The pull-off test has become a convenient method to characterize adhesion between two surfaces at the micro- and nanoscales using cantilever-based force sensors, such as an AFM. For the pull-off test, the indenter is first brought into contact with the sample, and then a force is applied to indent into the material. After achieving a maximum specified force, the indenter pulls away from the sample at a specified retraction speed. During this process, the nano-indenter device continuously measures displacements and forces, and the pull-off force can be measured. The pull-off force is taken as the minimum on the retract curve, as presented in Figure 3-9. Since hydrogels are compliant materials and the pull-off test is performed with an indenter with a large radius, JKR theory is the proper model to describe in case any adhesion occurs. According to the JKR theory, the pull-off force is [2]:

$$F_{po} = -\frac{3}{2} W_A \pi R \qquad (3\text{-}2)$$

Here R is the radius of curvature of indenter and W_A is work of adhesion.

In our experiments, we used AFM and the nano-indenter setup to measure the pull-off force between two hydrogel coated surfaces.

3.3.1 Adhesion between two hydrogel coated surfaces

As one of the components contributing to friction, adhesion has to be measured and compared to the friction force. Adhesion is expected to be rather small as the measurements were performed in an aqueous medium between two highly hydrated surface-attached hydrogels.

The pull-off tests were performed on two different scales. On the micro-scale, this force was determined by an atomic force microscope. The AFM pull-off tests were carried out between hydrogel pairs by a colloidal cantilever with a hydrogel coated polystyrene bead (1.98 µm diameter). During the AFM pull-off test, it was observed that the pull-off force is almost zero (i.e., the contact can be considered as Hertzian) for both PDMAA-1%MABP and PDMAA-5%MABP as these layers are basically bound water and the probability of chain-chain interaction is very low due to the negligible interpenetration as discussed in 3.1.1.

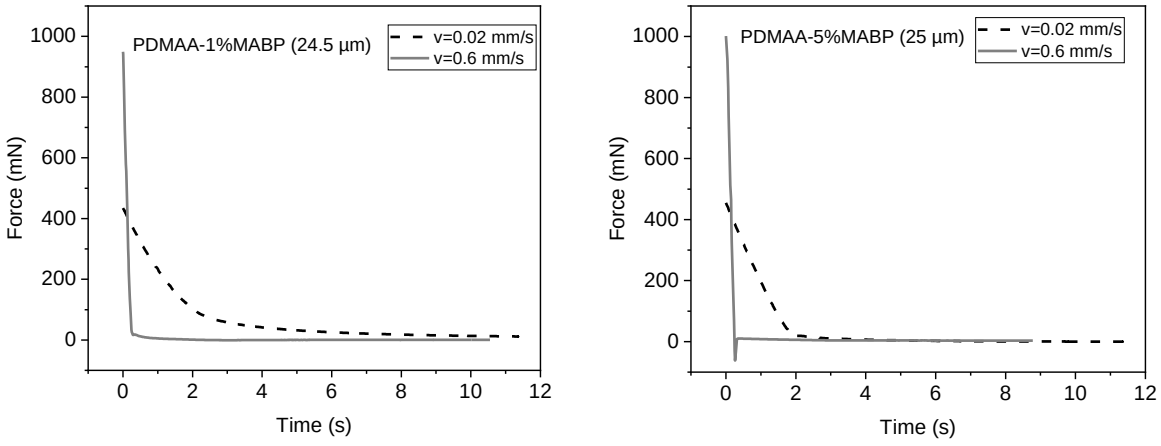

a) b)

Figure 3-14 a) Pull-off test performed with nanoscratch setup on PDMAA-1%MABP at F_N = 400 mN, v = 0.02 mm/s and F_N = 1000 mN, v = 0.6 mm/s b) Pull-off test with nanoscratch setup on PDMAA-5%MABP at F_N = 400 mN, v = 0.02 mm/s and F_N = 1000 mN, v = 0.6 mm/s.

Nevertheless, adhesion may become noticeable when the contact area gets larger. Thus, the pull-off tests were performed on a larger scale by a nano-scratch with a glass indenter of 25.94 mm radius coated with hydrogel. The normal force was applied, the surfaces were kept in contact for 5-10 seconds, and then the indenter was retracted at two different speeds.

We measured the pull-off force at different retract speeds (v = 0.02 mm/s and v = 0.6 mm/s) and different normal forces for PDMAA-1%MABP and PDMAA-5%MABP. It can be seen in Figure 3-14a that the pull-off force is zero for PDMAA-1%MABP in both cases where the normal load and retract speed are different.

The pull-off force is only observed for PDMAA-5%MABP at high retract speed (v = 0.6 mm/s) and normal load (F_N = 1000 mN). In this case, the pull-off force is 62 mN and its value depends on the normal force (contact size) and retract speed. The penetration depth is about 12 µm. This means that the sample is compressed almost to its half thickness and most of the water in the hydrogel network is squeezed out. Thus, the interaction gets closer to the dry state, where adhesion between two dry polymer layers is stronger than the fully hydrated state. Considering the pull-off test results, this force only exists when the crosslinker density is high and the sample is strongly compressed.

3.4 Permeation test

Water permeation of hydrogels can be tuned by changing the crosslinker concentration in synthesis or copolymerization by means of more hydrophilic or hydrophobic monomers. Water in gels can be either bound to the polymer or free bulk water. Lower mobility of water in hydrogels can be the consequence of chemical interactions or frictional effects [142]. Due to attractive forces between water molecules and polymer matrix, the mobility of water through gel can be reduced. Frictional effects can be classified as physical size exclusion, hydrodynamic friction, and increased apparent viscosity of water [142]. Impermeable and slowly moving polymer chains can hinder the displacement of water that leads to a longer effective path length for diffusion. Moreover, the resistance of fluid flow in the polymer matrix (i.e., hydrodynamic friction) and higher apparent viscosity of water differentiates bound water from free water. Friction between polymer chains and water is considered to be the main parameter that controls the water permeation of hydrogels, being responsible for the slow flow rate of water across the hydrogel [143].

Darcy's law has been developed to describe the permeability of a fluid through a porous media. Darcy's law is given in eq. (3-3):

$$Q = \frac{kA}{\eta h} p \qquad (3\text{-}3)$$

In this equation, Q is the total discharge, k is the permeability, A is the cross-sectional area, p is the applied pressure, η is the viscosity and h is the thickness of the sample.

Darcy's law has been used by Fujiyabu *et al.* as a method to predict the friction coefficient between the polymer network and water. The value of the friction coefficient can be estimated by applying a hydrostatic pressure from the top of a hydrogel. Fujiyabu *et al.* measured water permeation speed through the membrane in their experiment [143]. Afterward, they calculated the friction coefficient between polymer chains and water using eq. (3-4).

$$f = \frac{p}{hv} \qquad (3\text{-}4)$$

In the above equation, p is the applied hydrostatic pressure, h is the thickness of the hydrogel sample and v is the permeation speed (Q/A). The coefficient of friction here, which is in fact (η/k), differs from the conventional dimensionless friction coefficient and has units of Ns/m^4 [143].

To measure the transport properties of water inside hydrogels, we used a setup presented in Figure 3-15a (similar to Darcy's experimental setup). Water permeation of swollen bulk hydrogels was measured by means of a syringe with a diameter of 8 mm (the same setup used for swelling pressure measurement). During this test, the compression velocity was 60 µm/min. The compression force was recorded as a function of time and displacement using a tensile test machine (Zwick Z 2.5 (Zwick GmbH, Germany)) with a constant compression rate. Figure 3-15b shows an example of the recorded force to obtain a constant flow rate as a function of time. To eliminate the influence of the internal friction of the syringe, the test is repeated without hydrogel as well and the recorded force was subtracted from the force we recorded with the hydrogel. In a water permeation experiment, a hydrogel sample is always in contact with water in order to allow it to completely swell it to an equilibrium state.

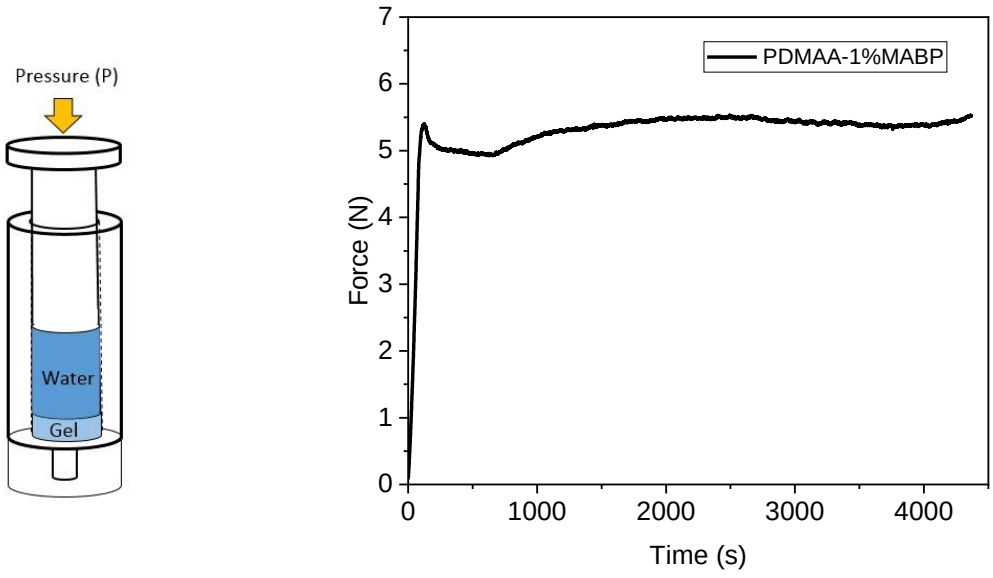

a) b)

Figure 3-15 a) Schematic drawing of experimental setup to measure permeability of hydrogels b) Example of the recorded force to obtain a constant flow rate as a function of time for PDMAA-1%MABP.

Hydraulic conductivity (*K*) is inversely proportional to the friction coefficient (f) presented in eq. (3-4). Since the viscosity of water in the hydrogel is different from that of the free bulk water, hydraulic conductivity is the property that describes how easily water can be displaced through the hydrogel. Hydraulic conductivity is the property of the whole system, including the porous medium and the flowing fluid. It is sometimes called 'permeability' in studies relevant to hydrogels and cartilage. The obtained hydraulic conductivity (*K)* (illustrated in Table 3-3) is lower for higher crosslinker density as the hydrogel with higher crosslinker density has a denser network and lower permeability.

Table 3-3 Hydraulic conductivity (*K*) of hydrogels with different crosslinking density.

PDMAA-1%MABP	PDMAA-5%MABP
3.53×10^{-14} m^4/Ns	2.5×10^{-14} m^4/Ns

The values obtained for the Hydraulic conductivity (permeability) of these hydrogels are almost in the same range as the value reported in the literature for the uppermost layer of articular cartilage (5.89×10^{-14} m^4/Ns) [37]. However, the permeability of this tissue changes through the depth to a value which is 10 times lower than the permeability of the top layer [37].

3.5 Creep test

In order to study the dynamics of hydrogel deformation, creep tests were performed. A comparison between the relaxation time measured in the creep test and sliding speed might be helpful in the explanation of the lubrication behavior. When a load is applied to a hydrogel sample, the overall deformation of hydrogels is the result of simultaneously occurring water displacement and polymer network deformation.

Creep tests on hydrogels were conducted by a nanoscratch (CSM) between the hydrogel pairs. During creep tests, the normal force was kept constant as the penetration depth was measured over time (shown in Figure 3-16). The penetration depth is expected to increase over time as it is controlled by the transport of water through and out of the network. Finally, the penetration depth should reach an equilibrium value.

The creep tests were performed for different normal loads for two different thicknesses of 1% crosslinker density to study the effect of confinement. Later, this test is repeated for 5% crosslinker to investigate the influence of crosslinker density on the relaxation time of the hydrogels.

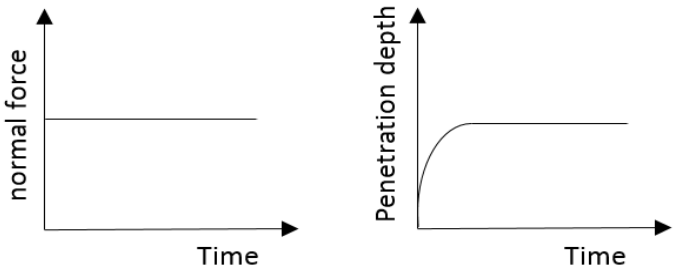

Figure 3-16 Normal force (left) and penetration depth (right) versus time during creep test.

3.5.1 Influence of confinement on relaxation time

Indentation in a hydrogel follows a stress relaxation process as the time progresses. Relaxation in response to the applied load in hydrogels is the result of two concurrent processes. The first relaxation process is a result of the conformational deformation of the polymer chains, and the other process is poroelastic relaxation, which is related to the transport of water out of the deformed region [144]. Under compression, chemical potential inside the gel changes, and the hydrogel reaches a new chemical equilibrium over time by exudation of the water. The

conformational relaxation process depends on the material stiffness under load and is independent of the contact area, while poroelastic relaxation strongly depends on the contact size. Therefore, poroelastic relaxation time can be controlled by the size of the contact area [97,144].

When the hydrogel layer is thick, the pressure distribution can be considered hemispherical under compression by a spherical indenter. In this case, the time required for the displacement of water will depend on the location of the water molecule. However, for a highly confined sample, the pressure distribution is rather uniform and cylindrical, which leads to an average shorter relaxation time as presented schematically in Figure 3-17 [144]. Time-dependent behavior of hydrogels might not be observed for highly confined samples since for such samples, the contact area is small.

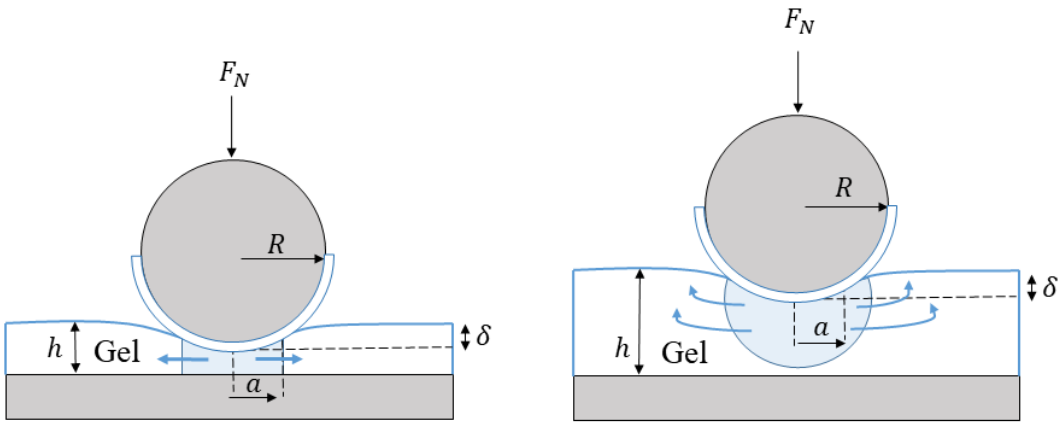

Figure 3-17 Influence of sample thickness/confinement on pressure distribution and relaxation time [145].

As the force is applied, due to the displacement of water, the penetration depth starts to increase gradually. During compression, there must be an initial linear response up to a critical value of strain. This linear region characterizes the deformation that can be sustained without water moving out of the network, and the system behaves elastically. Then, the transition to non-linear behavior occurs when the forces applied during compression are sufficient to overcome the resistance to water displacement, which is a function of the network permeability. After a specific time (relaxation time), the penetration depth reaches a constant value (δ_{max}), as presented schematically in Figure 3-16.

According to the creep tests performed between hydrogels, 60 - 80 % of the deformation happens immediately. The 20-40 % of the deformation occurs after a specific time, which

depends on the applied force, confinement, and water content of the hydrogel. For each applied normal force, the penetration depth is normalized by dividing the penetration depth to the maximum equilibrium value. It can clearly be seen in Figure 3-18 that when the applied force is higher, relaxation time is longer as a result of the larger penetration depth and contact area.

If we consider the Kelvin/Voigt model, which consists of a spring and dash-pot in parallel, the strain experienced by the spring is the same as that of experienced by the dash-pot. If a load is applied to the system, the spring will have the tendency to stretch, however it cannot react immediately since it is held back by the dash-pot. The relation between strain at a specific time and maximum penetration depth (strain) can be written as below:

$$\delta(t) = \delta_{\max}(1 - e^{\frac{-t}{\tau}}) \qquad (3\text{-}5)$$

In this equation, *t* is the time, δ is the penetration depth and τ is the relaxation time. By fitting equation (3-5) to our experimental result, the relaxation times are obtained for two different thicknesses (35 μm and 74.6 μm). The relaxation time, measured penetration depth, and calculated contact radius are given in Table 3-4.

Comparing the results presented in Table 3-4 for two different thicknesses of PDMAA- 1%MABP, one can see the difference in the relaxation time when the sample is thicker. This can be explained by the fact that the penetration depth is smaller for the thin sample due to the effect of the stiff substrate. Consequently, the relaxation time is shorter for a highly confined sample under the same normal load, which is due to the smaller penetration depth. For mostly the same penetration depth, relaxation time does not seem to be thickness dependent. So within the range of thickness we studied, the relaxation time is mainly determined by the penetration depth.

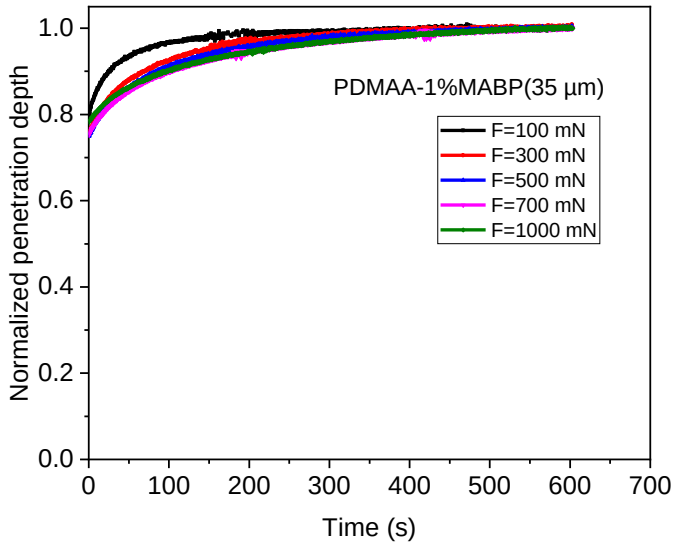

Figure 3-18 Normalized penetration depth versus time during the creep test on a sample with 35 µm thickness. Penetration depth was normalized by dividing the penetration depth by the maximum of each test.

Table 3-4 Creep test results for two samples with different thicknesses (35 µm and 74.6 µm).

Force	100 mN	300 mN	500 mN	700 mN	1000 mN
Relaxation time 35µm	47 s	79 s	98 s	110 s	129s
Penetration depth 35µm	11 µm	16 µm	19.5 µm	23.1 µm	27.8 µm
Contact radius 35µm	0.52 mm	0.63 mm	0.69 mm	0.75 mm	0.83 mm
Relaxation time 74.6 µm	79 s	81 s	103 s	129 s	160 s
Penetration depth 74.6 µm	16.3 µm	20.5 µm	25.4 µm	32.1 µm	43.2 µm
Contact radius 74.6 µm	0.63 mm	0.71 mm	0.80 mm	0.90 mm	1.04 mm

3.5.2 Influence of crosslink density on relaxation time

To investigate the influence of crosslinker density, relaxation tests were performed for 5% crosslinker density for a sample with about 35 µm thickness. According to Figure 3-19, relaxation curves differ only slightly for PDMAA-5%MABP by increasing load as the penetration depth does not change significantly. Relaxation time was obtained using the same equation (eq. (3-5)). By increasing the normal load from 100 mN to 1000 mN, relaxation time changes only from 65 s to 69 s. Penetration depth for this sample varies between 10 µm and 17

μm. As the applied load is increased for a higher crosslinker density, due to lower water content, penetration depth and relaxation time do not change significantly. Relaxation time is longer under 100 mN applied load for higher crosslinker density, which can be elucidated by lower permeability of these networks. However, relaxation time is almost constant and does not change noticeably by increasing the applied load. When applied load is increased ($F_N \geq 300$ mN), the relaxation time is larger for the low crosslink density sample. Swelling ratio measurements also demonstrated that the water content of PDMAA-5%MABP is almost half of the PDMAA-1%MABP. Since relaxation is directly related to the water content, a decrease in the relaxation time by decreasing displaced water volume (through the network) is an expected outcome.

The relaxation time of hydrogels with high water content (low crosslinker density) varies noticeably by penetration depth. This observation points out that the friction force might only be velocity dependent at high penetration depth for hydrogels with high water content.

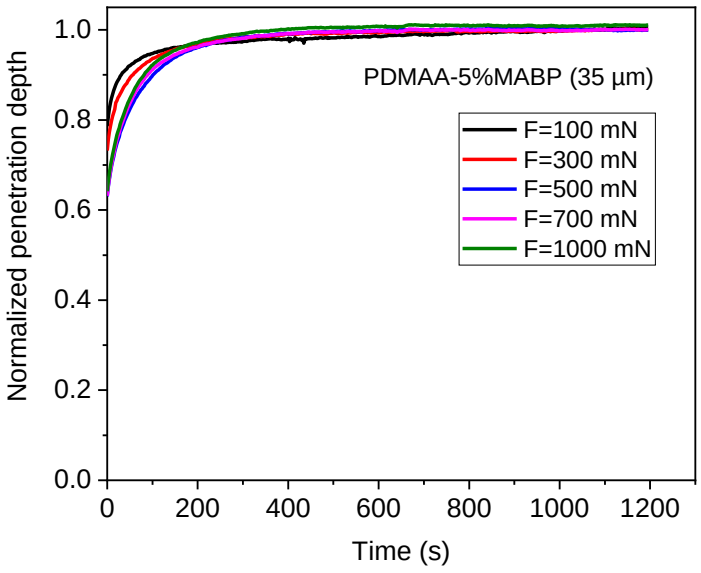

Figure 3-19 Normalized penetration depth versus time for a sample with 5% crosslinker (PDMAA-5%MABP).

Relaxation time measured during the creep test might be helpful in the prediction of the state of a hydrogel. The time required to move the contact about one contact radius can be calculated by eq. (3-6). If the time needed to translate about one contact radius (presented in Figure 3-20) is smaller than the relaxation time ($t < \tau$) then the hydrogel is not in a relaxed state during friction test, meaning that the water inside the network is not squeezed out

completely. While $t > \tau$ indicates the case when sliding happens slower than the relaxation rate. For instance, if we assume the case with relaxation time of 100 s and the contact radius of 1 mm, to have the hydrogel layer in a complete relaxed state, the sliding speed should be below 0.01 mm/s. It must be noted that migrating contact (friction test) might differ from the stationary contact (creep test).

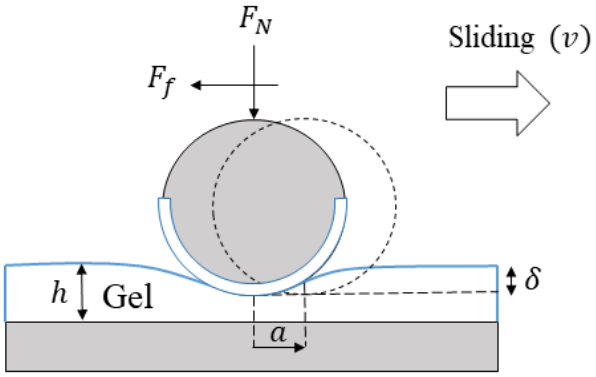

Figure 3-20 Schematic representation of the contact translation. A comparison between the time needed to translate the contact about one contact radius and relaxation time can determine if the gel is in relaxed state.

$$t = \frac{a}{v} \tag{3-6}$$

3.6 Friction test

As it was mentioned in Chapter 1, hydrogels can show low friction under specific conditions, especially when hydrogel pairs are in contact. Considering the fact that surface-attached hydrogels swell anisotropically and show entropic barrier against interdigitation, it is expected that two surface-attached hydrogel layers represent different lubrication behavior from that of free gels sliding against each other. In comparison to free-standing gels, surface-attached layers are more stable under high forces and shear rates due to the substrate supporting them and the chemical bond to the substrate. In order to study the frictional properties of surface-attached hydrogels, we have used two different techniques that are lateral force microscopy of the atomic force microscope (JPK nanowizard4) and nanoscratch testing setup. With AFM, large contact areas, high sliding speeds and high pressures are not achievable. Since the influence of water displacement (time-dependent

behavior) might only be observed when the contact area and penetration depth is large, we used the aforementioned two measurement setups to cross-scale friction.

3.6.1 Friction test with the AFM

One of the difficulties associated with friction measurement using AFM is the lateral force calibration of the cantilever as the lateral stiffness of the cantilever is unknown. So far, several lateral force calibration methods have been developed which are rather complex [146–149]. In this work, we used the improved wedge method proposed by Varenberg *et al.* [150], where commercially available calibration grating is used. This method is suitable for calibration of integrated and colloidal probes with any radius of curvature smaller than 2 µm [151].

The lateral force between the AFM tip and the surface can be recorded as a voltage. Frictional properties of the material can be calculated using a calibration factor that transforms the measured lateral signal to the lateral force. Then, the lateral force ($F_{lateral}$) can be obtained from the recorded lateral voltage signal ($V_{lateral}$) and the calibration factor (α) [146,150,151]:

$$F_{lateral} = \alpha V_{lateral} \qquad (3\text{-}7)$$

When the tip is sliding over the sample laterally, torsion appears on the cantilever. The calibration factor can be obtained by measuring a friction loop on a calibration grating by recording the lateral voltage signal when the probe scans the surface at a scan angle of 90° (demonstrated in Figure 3-21) [151]. The calibration grating is a KOH etched silicon wafer with well-defined sloped facets with an angle of 54.74° (TGF11 calibration grating (MicroMasch)). The friction loop was measured in water with AFM colloidal cantilever (CP-CONT-PS-A) from NanoAndMore Company with a polystyrene bead with a diameter of 1.98 µm. The polystyrene bead of the cantilever was coated by means of drop coating with a very thin layer of hydrogel.

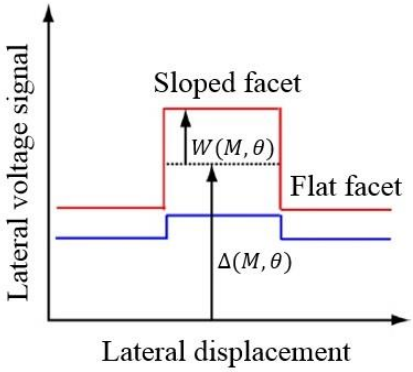

Figure 3-21 Schematic of the torsion loop for downhill (blue line) and uphill (red line) scan obtained on a sloped surface [151].

The half width (W) and offset (Δ) of the friction loop are functions of torsional moment and angle of the sloped facet. The measured calibration factor (α) changed between $4 \times 10^{-7} N/V$ and $6 \times 10^{-7}\ N/V$ for normal loads between 50 nN and 100 nN. The lateral signal was recorded for samples with the following thicknesses: 14.7 µm, 24.5 µm and 35 µm. Each measurement was performed on three different spots of each sample. During friction tests, the sliding speed was 10 µm/s. The applied force was changed from 50 nN up to 100 nN. The coefficient of friction is obtained by dividing the friction force by the normal load. The calculated friction coefficient values are plotted as a function of the applied force and pressure in Figure 3-22a and b, respectively. It can be seen that the coefficient of friction is lower for the thicker sample, but there is no substantial difference in the measured values for the three samples. Furthermore, there is no clear increasing or decreasing trend for COF as a function of applied load due to the very limited range of the force we can apply in AFM tests. Slightly higher values of COF for the thinner sample might be the result of higher confinement. For the same applied range of forces, penetration depth varies from 190 nm to 250 nm for the thin sample, while this range is from 200 nm to 400 nm for the thick sample. Confinement (penetration depth divided by thickness) for the thin sample is from 0.01 to 0.015 and 0.005 to 0.01 for the thick sample. The confinement is already low enough to have no influence on the results. Therefore, the difference might be due to slightly different stiffness and water content. Pressure (Figure 3-22b) is calculated using Hertz theory by substituting the penetration depth, applied load and radius of the PS bead, as no adhesion was observed. Friction tests with AFM are limited to small contact areas. Therefore, it is reasonable if we do not observe any obvious growing or reducing trend. Further friction measurements with the nano-scratch machine

provide the possibility to apply higher forces and measure friction in a broader range of sliding speeds.

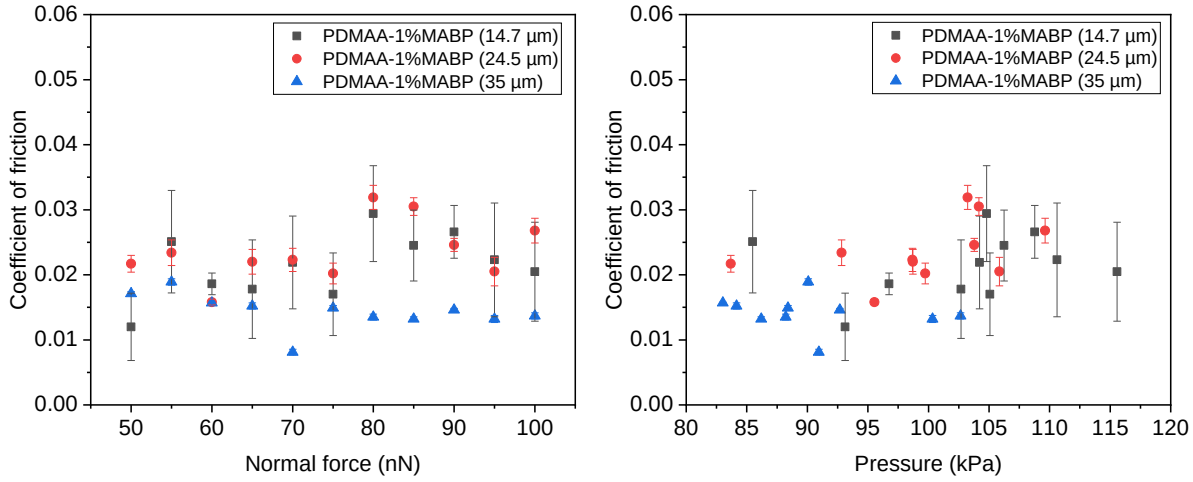

a) b)

Figure 3-22 Coefficient of friction versus applied normal load and pressure from the friction tests with AFM for three different thicknesses (14.7 µm, 24.5 µm and 35 µm).

3.6.2 Friction test using nanoscratch setup

The friction tests on the samples were carried out with a CSM nanoscratch setup (Anton Paar). A glass lens with a radius of 25.94 mm, coated with a thin layer of the same hydrogel (same coating process as described in the experimental chapter) was used as a slider. Both the slider and the sample were immersed in water during the friction test. The sample was moved perpendicular to the slider in one direction while the contact force was held constant (unidirectional friction test). The tangential force and penetration depth were measured continuously on a path 3 to 4 times longer than the contact diameter. The measurements were performed for five different contact forces between 100 mN and 1000 mN (100, 300, 500, 700, and 1000 mN), and the sliding speed varied for more than two decades in the range of 0.006-1.4 mm/s. The data recording rate was 100 Hz. Two displacement sensors (LVDT sensors) record the friction and normal forces through the stiffnesses of parts of the machine, as depicted in Figure 3-23a.

The coefficient of friction is obtained by dividing the tangential force by the normal force, however, this does not imply that the friction of hydrogels obeys Amonton's law. In these experiments, it was seen that there was no permanent deformation of the gels occurring during the friction tests. An example of the recorded normal force, friction force, and penetration depth

can be seen in Figure 3-23 (b), (c) and (d), respectively. The normal force and the friction force are almost constant after 0.3-0.5 mm sliding length as the test reaches a steady state. During each sliding test, the normal force and sliding speed were kept constant. In all the friction tests, unique slider was used to avoid the influence of variation of the thickness of hydrogel layer on the slider. All the presented data in the following sections represent an average of three measurements. Pre-scan and post-scan were performed with a small contact force (3 mN) to evaluate the profile before and after the friction test to check for any permanent deformation on the surface due to the friction process and assessing the penetration depth during sliding. To ensure that there is no extra force on the slider due to measurement in water in our friction tests, we did one test in pure water and the force was below the detection limit of the nanoscratch test setup.

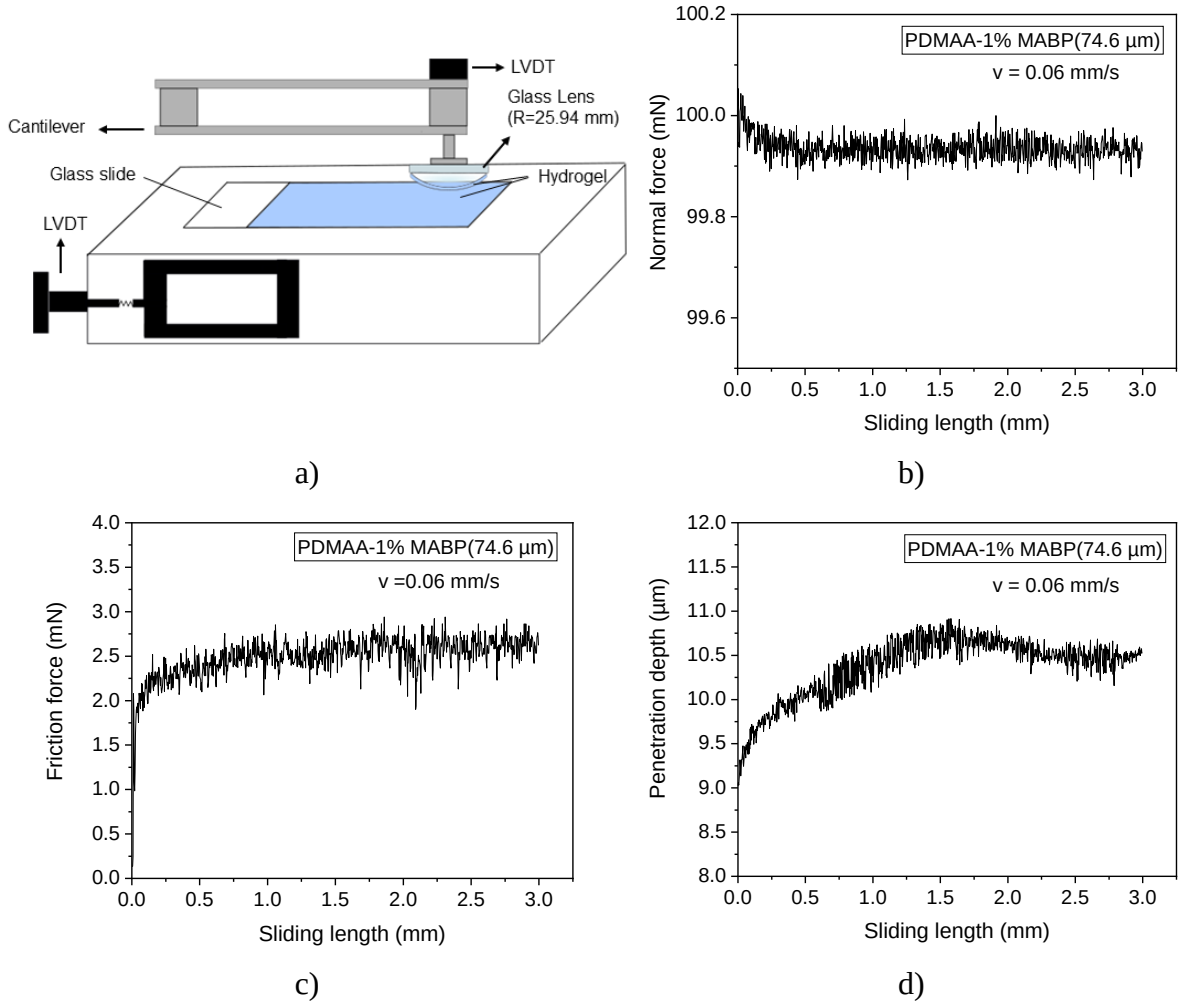

Figure 3-23 a) Schematic illustration of the experimental setup of the friction experiments b) Normal force (F_N) and c) Friction force (F_f) of 74.6 µm thick PDMAA-1% MABP layer under water d) Penetration depth measured by the displacement sensors; sliding speed v = 0.06 mm/s.

3.6.2.1 Adhesion induced friction

Although pull-off force measurements give an indication of the adhesion between two surfaces, the contact area between the indenter (slider) and sample under static conditions is different from that when sliding. Actually, all the contact points between the countersurfacs are not broken simultaneously, as it happens during pull-off under static (non-sliding) conditions. Moreover, the shear solicitation undergone by the interface and the surrounding bulk material during sliding differs largely from the normal contact configuration. Even though we have shown in section 3.3.1 that no measurable pull-off force exists between two PDMAA- 1% MABP pairs, we have tried to measure adhesion induced friction and contribution of adhesion to the friction force.

To elucidate the friction behavior of the swollen hydrogels, first, the contribution of the adhesion forces between the two hydrogel surfaces was investigated. Hence, the friction force was measured at low load (3 mN) and low speed (0.001 mm/s) with a setup shown in Figure 3-23a. Under the applied conditions, the hydrogels are almost not compressed and the penetration depth is almost zero. Therefore, any friction force observed is almost exclusively caused by the adhesion between the two hydrogel layers. In these experiments, the observed friction force was below the detection limit of the setup (< 3 µN), which confirms that the adhesion component is very small. Even though, due to experimental constraints, we cannot give a precise value, we can estimate that the coefficient of friction is below 0.001 when we take the resolution of the machine and the applied normal load into consideration. This is not surprising as essentially the two surfaces consist mostly of water with an easily shearable water-based interface. As the polymer subchains of the two gel layers do not penetrate each other, the surfaces show very little interaction. The adhesive interactions happen only at the very periphery of the surface between the dangling ends of the chains at the interface, as it is illustrated schematically in Figure 3-24 by purple.

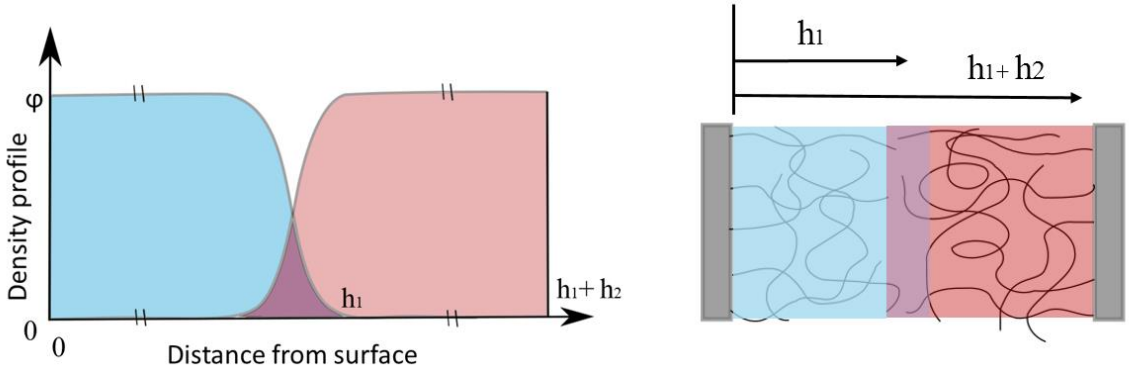

Figure 3-24 Profile density of the two surface attached surfaces in contact as a function of distance from surface. Interpenetration only happens at the very few nanometers of the surface (purple area) [128].

3.6.2.2 Influence of the film thickness on coefficient of friction

When we speak about surface-attached thin hydrogels, the thickness might play an important role in friction as a result of varying confinement, which is imposed by the hard substrate and spherical indenter. Under the same applied normal load, the volume that has to be deformed during sliding depends on the elastic modulus of the layer, confinement, and sliding speed. The friction force, which is the resistance of the material against deformation during sliding, is influenced by polymer relaxation time and diffusion time of water within the polymer network. Both relaxation of the polymer and water flow induce a time-dependent behavior in hydrogels lubrication. Consequently, the influence of the normal load, sliding speed and confinement was investigated by recording friction force for four samples with different thicknesses (35 µm, 47 µm, 52.8 µm, 74.6 µm). All the thicknesses are given in the swollen state. Friction tests were carried out for normal loads of 100, 300, 500, 700, and 1000 mN. For each normal load, friction force was recorded for sliding speeds from 0.003 mm/s up to 3 mm/s. The recorded friction force for each sample is presented at different loads and sliding speeds in Figure 3-25.

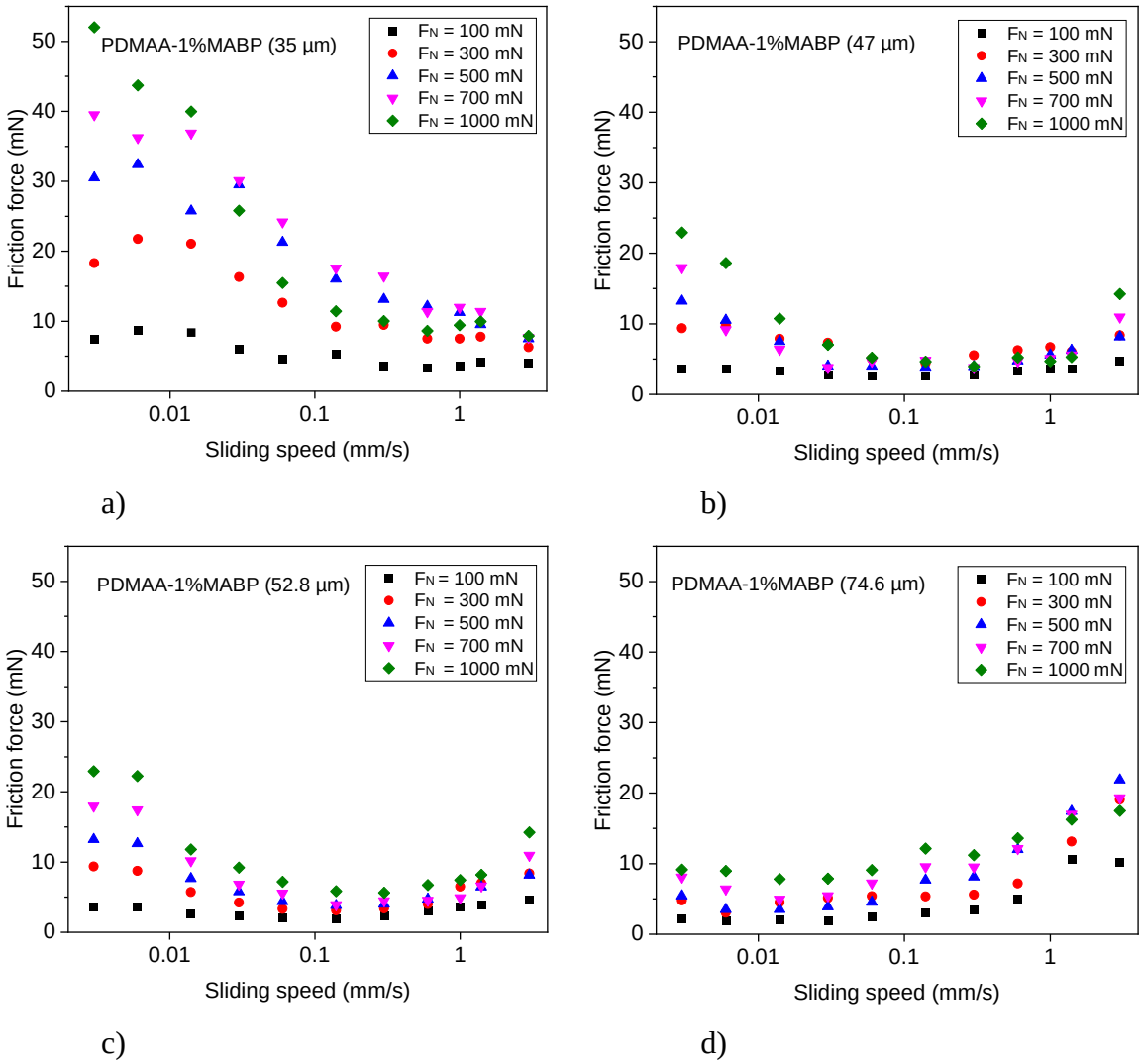

Figure 3-25 Friction force as a function of sliding speed for different thicknesses (a) 35 µm b) 47 µm c) 52.8 µm and d) 74.6 µm.

In Figure 3-26, the coefficient of friction (obtained by dividing friction force by normal force) is plotted versus sliding speed. It has to be noted that all the dashed lines in this thesis are guide to the eye. Different trends can be seen by changing the thickness. For the sample with a thickness of 35 µm, the friction coefficient decreases by faster sliding. As the thickness increases (47 µm and 52.8 µm), the friction coefficient decreases slightly and starts to increase after a specific sliding speed. For the thickest sample coefficient of friction rises continuously.

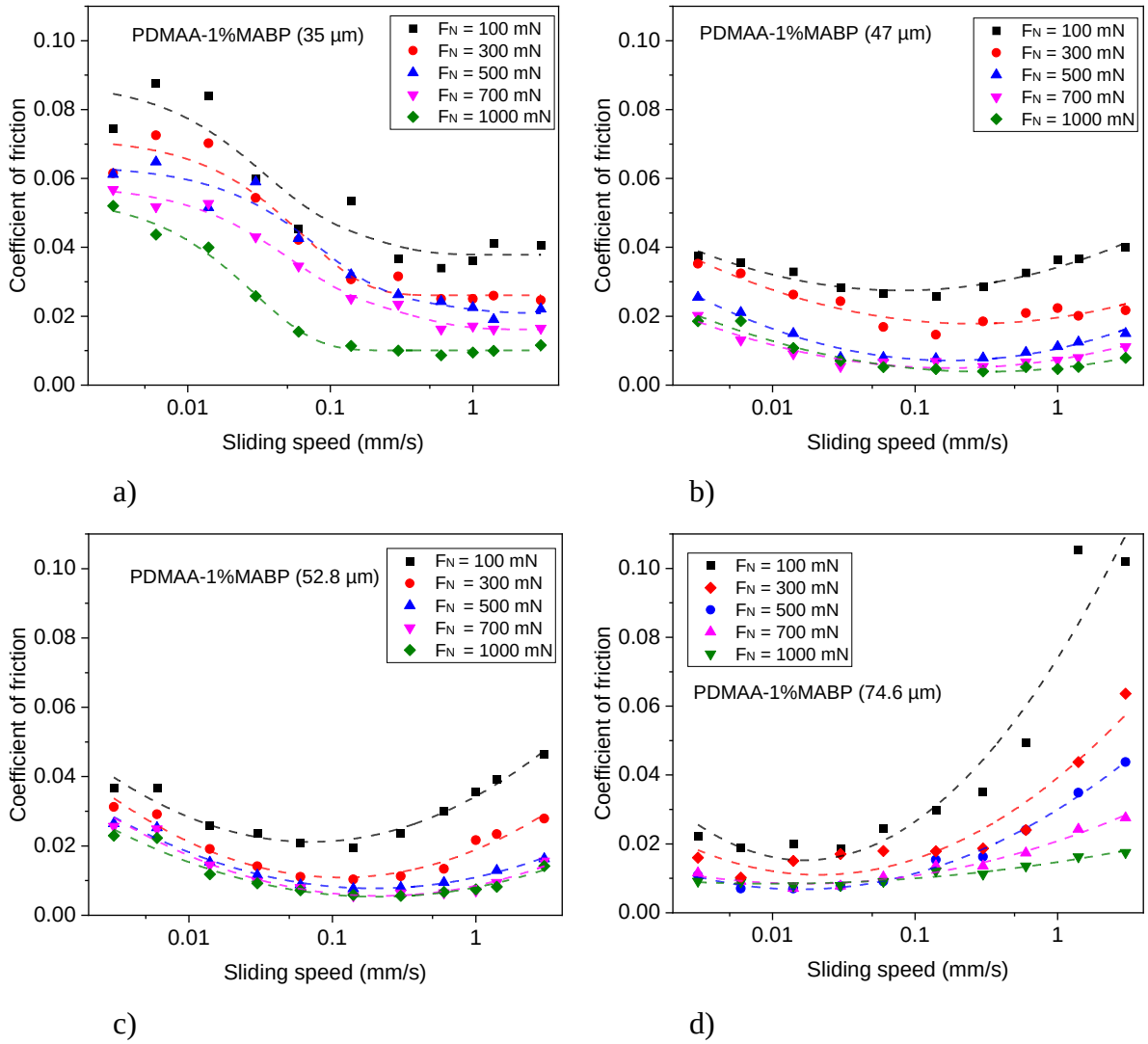

Figure 3-26 Coefficient of friction as a function of sliding speed for different thicknesses (a) 35 µm b) 47 µm c) 52.8 µm and d) 74.6 µm).

To understand the difference in the behavior of thin and thicker films we observed in the coefficient of friction, we compare the penetration depth of two extreme cases (thinnest sample 35 µm and thickest sample 74.5 µm). At slow sliding speed, the hydrogel can relax easily as the water can be displaced and polymer network can also conform. Thus, the penetration depth is larger at low sliding speeds. By increasing the sliding speed, penetration depth starts to decrease rapidly, since the water cannot be displaced completely. After a specific sliding speed, penetration depth stays almost constant. As can be seen in Figure 3-27, the difference in penetration depth for the maximum and minimum load of the thin sample is smaller than that of the thick sample. This illustrates the influence of the confinement, which is defined as the ratio of penetration depth and thickness. This value shows the extent to which the sample is compressed. As the thinner sample is highly confined, the penetration depth

cannot increase with the same factor as for the thicker sample. The apparent elastic modulus (contact stiffness) increases as the deformation zone propagates from the deformed area in the hydrogel to the substrate. Apparent elastic modulus depends on the properties of both layers and the confinement. As the confinement increases, the apparent elastic modulus of the layer becomes larger, which means that the layers become more difficult to deform.

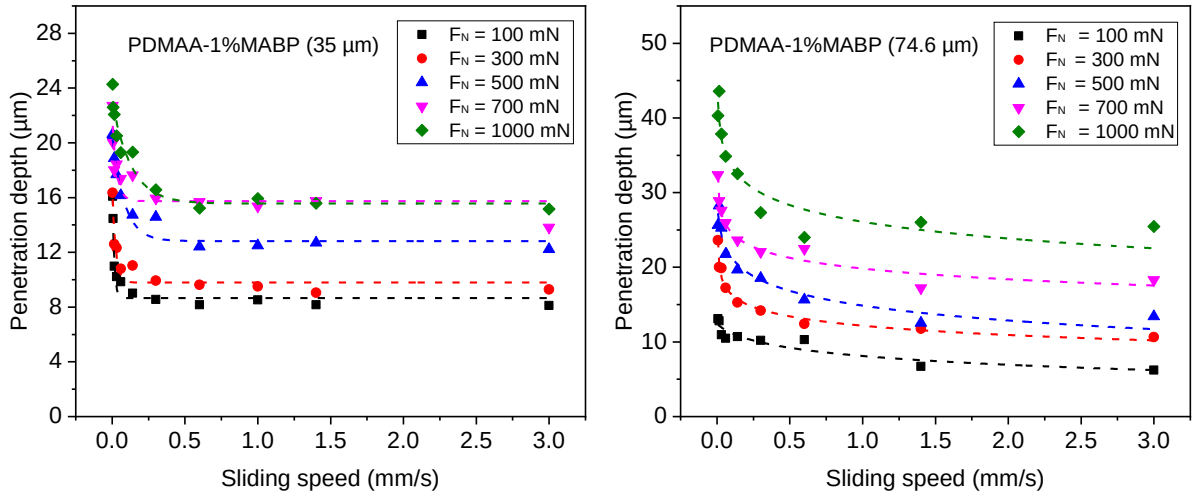

a) b)

Figure 3-27 Measured penetration depth as a function of sliding speed in a scratch test for two samples with different thicknesses (35 µm and 74.6 µm).

3.6.2.3 Nonlinearity of friction force

Despite the difference in how the coefficient of friction changes according to sliding speed for various thicknesses, the common observation in all plots of Figure 3-26 is the reduction of coefficient of friction at higher normal loads. Clearly, hydrogels exhibit a deviation from Amantons law [152,153]. This has been reported and attributed to the influence of adhesion [153], however, as shown above for surface-attached layers, adhesion is negligible. In Figure 3-28, the friction force is plotted versus the normal load for the 35 µm and 74.6 µm thickness samples. For the thin sample (35 µm), the friction force is almost the same at different sliding speeds when the normal load is small, but the difference becomes noticeable as the applied load increases. In addition, the friction force is higher at a slower shear rate due to the larger penetration depth. Friction force tends to possess a constant value as the sliding speed increase. In contrast to this case, for the thicker sample friction force seems to be essentially speed dependent rather than force dependent. The friction force appears as non-linear functions for both samples and at high loads, it reaches an almost constant value. As the friction force depends strongly on the volume that has to be displaced, this phenomenon should be due to the

limited compressibility of layers that is imposed on the system by different parameters such as osmotic pressure, stretchability of the chains, and confinement. The influence of these parameters will be discussed individually in the next chapter.

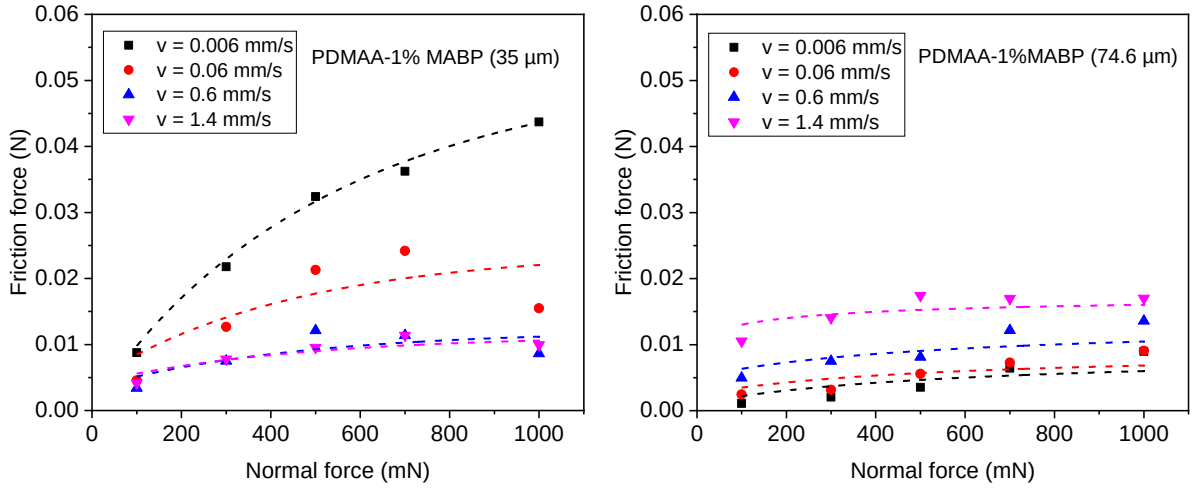

a) b)

Figure 3-28 Friction force versus applied load at different sliding speeds for two samples 35 µm and 74.6 µm.

3.6.2.4 Influence of crosslink density

As it was shown in sections 3.2.2 and 3.4, crosslink density is the factor that controls stiffness, permeability, and water content of the hydrogels through the determination of the network density. To investigate the effect of crosslink density on lubrication of hydrogels, friction tests were carried out on samples with the same wet thickness (≈ 25 µm) for crosslinker densities of 0.5%, 1%, and 5%. In a highly crosslinked polymer network, polymer chains are closely linked, which means the polymer network is denser and, consequently, has lower water content. By increasing the density of the polymer network, the interaction between polymer chains increases. In polymer networks, when we speak about the mesh size and permeability, the size of the water molecule is far smaller than the mesh size. Therefore, under compression, the water has to squeeze out of the network as water is an incompressible fluid. For a highly crosslinked network, the polymer chains are densely crosslinked, so it takes longer for the same volume of water molecules to pass through a network (i.e., longer relaxation time). Therefore, the higher crosslinker density leads to a longer time for water transportation, which we call apparent viscosity of water. It is similar to the case where water in the network has higher viscosity (in comparison to free water) and resistance against the flow.

As the crosslinker density increases, the volume of the water that has to be displaced decreases, however, the resistance of water to flow and adhesion increases at the same time. Although penetration depth is smaller (lower confinement) under the same applied load, the 5% crosslinker density sample is stiffer and more difficult to deform. All these factors lead to higher friction for the higher crosslinker density, as depicted in Figure 3-29. By applying a higher load, the difference in COF caused by the crosslinker density becomes smaller. The small difference implies that at high compression, the friction coefficient might become independent of the crosslinker density since the polymer volume fraction reaches a constant value.

Similar to what is observed in Figure 3-26a, friction is higher at slow sliding speed. An increase in sliding speed results in lower COF. The transition point from the high coefficient of friction clearly changes as the crosslinker density varies. The transition point, where minimum friction happens, depends on the water content (and consequently crosslink density). Minimum COF occurs between 0.3-0.6 mm/s for 5%MABP and between 0.06-0.14 mm/s for the 0.5% MABP.

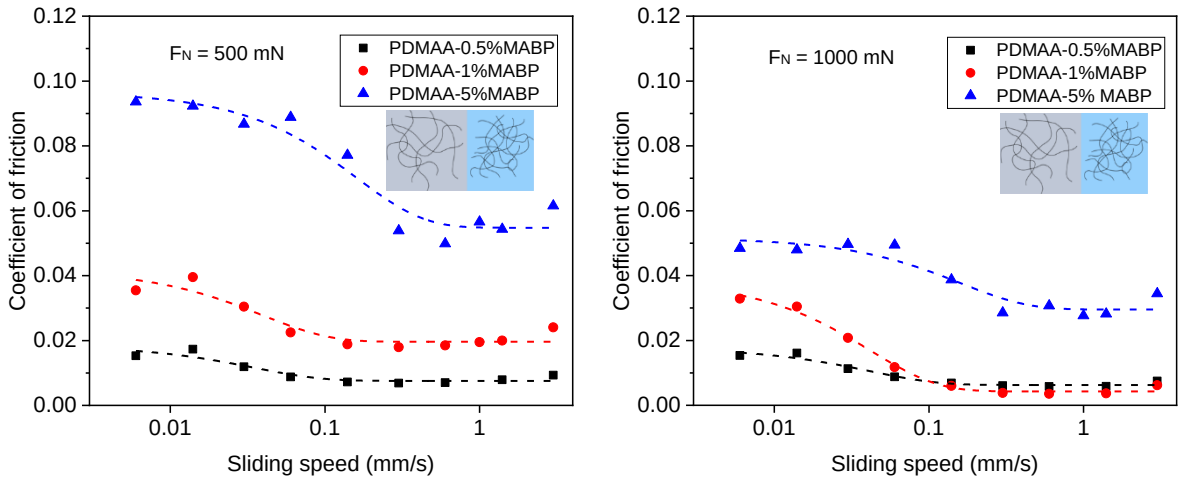

a) b)

Figure 3-29 COF as a function of sliding speed for different crosslinker densities for samples with almost the same wet thickness (≈ 25 µm) under a) 500 mN and b) 1000 mN normal load.

3.6.2.5 Influence of pressure on the frictional behavior

A different representation of the system is obtained when we move from the discussion of the forces to the applied pressures which takes into account the differences in the penetration depth in the different experiments. The maximum pressure is calculated from the applied load and the penetration depth by the Hertz theory (given in eq. (3-8)).

$$p_{max} = \frac{3F_N}{2\pi a^2} \qquad (3\text{-}8)$$

Here F_N is the normal load and a is the contact radius.

In Figure 3-31a and b, the coefficient of friction is presented as a function of the calculated pressure for the thin (35 µm) and thick (74.6 µm) samples, respectively. It is seen in Figure 3-30 that an increase of the applied pressure results in an increase of the friction force, but a decrease of the COF in all cases. In contrast to the thin sample (Figure 3-31a), for which the highest COF belongs to the lower sliding speed, the highest COF appears at high sliding speed for the thick sample (Figure 3-31b). Such a difference denotes a difference in the lubrication mechanism of the two samples.

A constant friction coefficient for the thick sample during slow sliding speed over a range of a few hundred kPa (as seen in Figure 3-31b (black curve)) indicates a relaxed hydrogel layer whose frictional properties are not strongly dominated by water flow. At higher sliding velocities (purple curve), however, the COF decreases very strongly with the applied pressure. On the other hand, the coefficient of friction has higher values at low sliding speed when the thickness is small. The different behavior is already presented in terms of the friction force in Figure 3-28. The parameter that determines friction seems to be the penetration depth which is larger when sliding is slow.

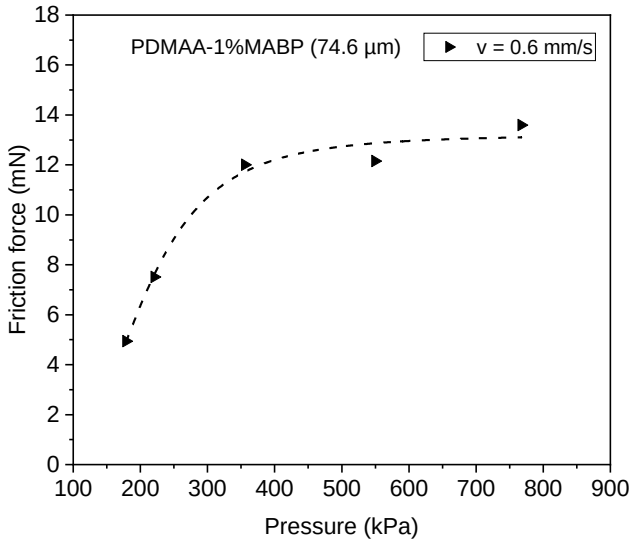

Figure 3-30 Friction force versus pressure for the sample with 74.6 µm thickness at sliding speed v = 0.6 mm/s.

As the applied load becomes larger, the increase in friction force is only rather weak as the penetration depth does not increase much. Therefore, the COF decreases by increasing pressure as a consequence of the non-linear relationship between the friction force and normal force. The non-linear friction force arises from the limited compressibility, which is discussed further in Chapter 4

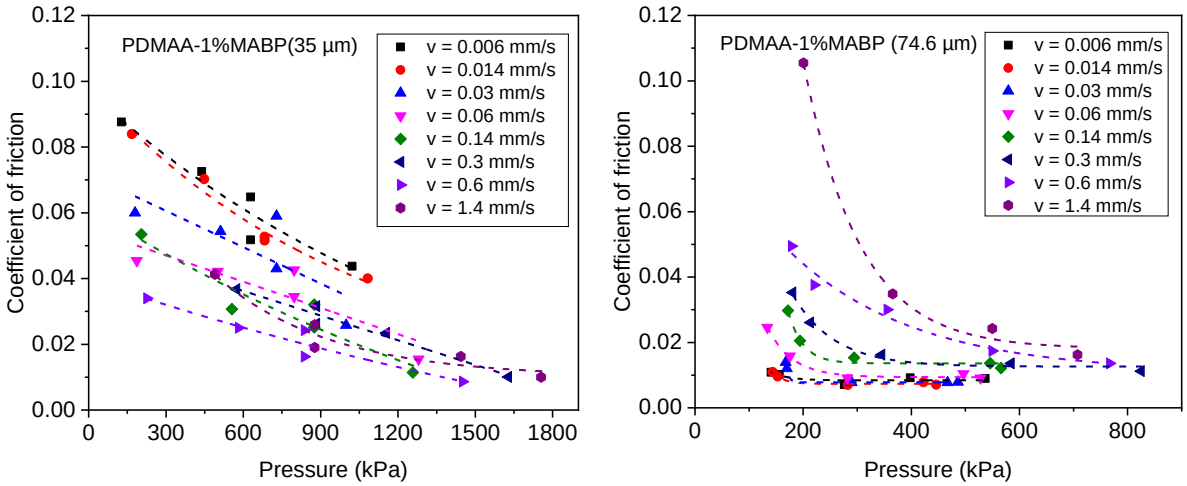

a) b)

Figure 3-31 Coefficient of friction against maximum contact pressure during sliding tests of 35 µm and 74.6 µm thick samples.

4 Physical description of friction

4.1 Friction model

Since hydrogels consist of two components (i.e., water and polymer network), their friction behavior cannot be explained by a conventional Stribeck curve [53], as both the fluid phase and the solid phase contribute to the friction process [116]. Strong stretching of the chains away from the surface due to swelling in such surface-attached systems prevents an interpenetration of the network by chains coming from the outside. Thus the formed energy barrier prevents the attachment of any large molecules such as those contained in the opposing friction partner [111,128]. Surprisingly, at first view, the exclusion of large molecules in surface-attached gels is stronger than the polymer brushes. This is due to the fact that interpenetration occurs only in areas where the segment density is low. While surface-attached brushes exhibit a parabolic profile (for polydisperse systems even with an exponential tail), surface-attached polymer networks swell with delta-like profile. The difference in the segment density profile was shown in section 3.1.1. Therefore, surface-attached polymer networks can be considered as interesting candidates to achieve superlubricity [111,112,114,128].

When two hydrogel-coated surfaces slide against each other, one needs to consider several forces that influence the friction force. Different components of friction force are schematically shown in Figure 4-1. These forces are:

- Adhesion forces between the two surfaces (F_A): Adhesion forces originate from van der Waals forces [154] and entanglement of polymer chains with chains originating from the opposite contact surfaces. As the polymers used in this study do not contain any charges, electrostatic contributions are not discussed. The vdW forces between a sphere and a flat surface can be described as:

$$F_A = -\frac{HR}{6D^2} \qquad (4\text{-}1)$$

  where R is the radius of the spherical slider, H the Hamaker constant and D is the distance between the two surfaces.

Adhesion dominates the frictional properties only when the applied load and penetration depth is very small. Then, the adhesion force will be the only component of the friction force.

- Polymer deformation force (F_p): This component is a function of the penetration depth and assumed to be independent of the sliding and compression velocity. Upon indentation, the polymer chains become stretched. The extent of stretching depends on the depth of indentation and the shape of the slider. This contribution is determined by the difference between the osmotic pressure of the gel (swelling pressure) and the applied pressure (load per contact area). It is (as well as the penetration depth) influenced by the (apparent) elastic modulus, which itself depends on the confinement and crosslinker density. The polymer deformation ability is a thermodynamic property.
- Drag force (F_D) [155]: The water displacement induces a force that resists sliding. Since water is incompressible, with increasing sliding speed, the resistance of water to flow will become stronger. The resistive force depends on the geometry of the slider, the penetration depth/confinement and the viscosity of the water inside of the hydrogel (apparent viscosity) or permeability of the network.

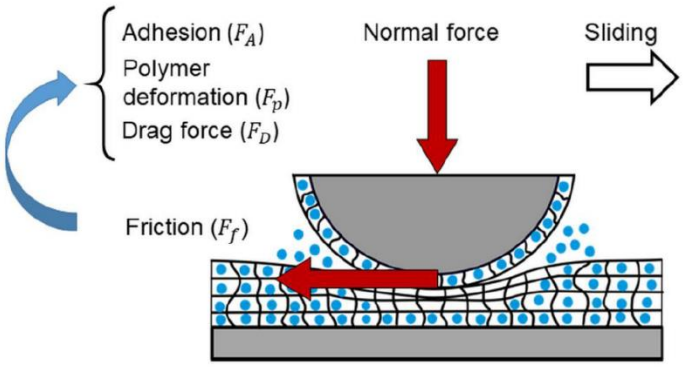

Figure 4-1 Influence of the forces on the friction during sliding of a hydrogel coated slider on a surface-attached hydrogel – Red arrows depict the forces acting on the slider. Blue circles represent schematically water in the polymer network (strongly schematic).

Thus, the friction force can be written as the sum of above mentioned three components:

$$F_f = F_A + F_p + F_D \qquad (4\text{-}2)$$

Previously published publications have reported the occurrence of stick-slip motion, especially at higher sliding speeds [124] or applied loads [156]. Dunn et al. reported an over ten times increase in the coefficient of friction by increasing the applied load. They have related this to the presence of stick-slip phenomena. Since stick-slip behavior occurred at low pressures related to the elastic modulus of the material, they have attributed it to the collapse of the soft hydrogel layer and high polymer concentration [156]. In contrast to these studies, in which the contact was between a solid slider and a hydrogel layer, a substantially different situation is expected for hydrogel-hydrogel contacts. In our experiments, it is observed that the adhesion is very small and does not contribute much to the friction behavior so that at low normal load and low sliding speed, extremely small friction between the hydrogel-coated surfaces is observed. This is due to the fact that the polymer chains in the surface-attached hydrogel layers cannot interpenetrate the opposite layer. In addition, two strongly hydrated layers show only rather weak attractive interactions and thus high lubrication potential. Consequently, the shear force required to separate the two surfaces during sliding and accordingly, the friction is extremely low so that we cannot measure the exact value.

In sliding experiments at higher loads and higher velocities, polymer deformation and drag forces are the main force components contributing to the friction force. Therefore, the two main factors that govern the friction force are the volume of the material displaced by the indentation and the sliding speed. When we compare the penetration depth for applied loads of 100 mN and 1000 mN (Figure 3-27), the penetration depth is only 2-3 times larger for 1000 mN than for the smaller load. This is due to the fact that the compression of the layers makes them stiffer as a result of an increase in the segment density. Additionally, the polymer chains are becoming stretched. However, with increasing penetration of the slider, the chain stretching becomes stronger. At a high extent of stretching, the stress of the chains increases with the strain in a strongly non-linear fashion, hence the penetration becomes strongly limited. Furthermore, the influence of the rigid substrate results in a confinement effect. The latter phenomenon makes the very thin polymer layers almost incompressible at high applied pressures. As the penetration depth is not strongly increasing with load, also the displaced volume of water remains almost constant. Accordingly, the friction force also assumes an almost constant value, as can be seen in Figure 3-28. As a consequence, the COF decreases with increasing normal load and becomes less dependent on the sliding speed, which is reported in Figure 3-26.

When looking at higher sliding speeds, we need to consider the rate of polymer network compression or, in other words, the rate of water transport. The flow of water through the swollen hydrogel, which on a molecular scale resembles a rather concentrated (i.e., 20%) polymer solution, causes a drag force (F_D). The drag force will depend on the viscosity of water flowing through the gel (apparent viscosity of the water inside of the gel) and on the volume of water that needs to be displaced.

4.2 Merging curves of different confinements

In our investigations on the influence of sliding speed in frictional behavior, we have observed how the thickness of the confined sample can lead to different outcomes (shown in Figure 3-26a-d). The four curves obtained for four thicknesses seems to show a continuous behavior, meaning that a master curve may be generated from a series of curves of overlapping data at different confinements. The master curve enables the description of the full behavior over a much wider range of sliding speed than what was accessible with our test setup.

Polymers have been studied widely in terms of their viscoelastic properties and time dependent behavior. The quantitative influence of time and temperature on the viscoelastic behavior is known as the time-temperature superposition [157]. The Williams-Landel-Ferry (WLF) equation is a model used to describe the time-temperature superposition precisely. By means of the WLF equation and time-temperature superposition prediction of the mechanical properties of polymers outside of experimental timescale is possible. In time-temperature superposition, the equivalency between time and temperature allows creating a master curve from linear viscoelastic data by shifting measurements at different temperatures to get a continuous curve at a reference temperature. Glass transition occurs as a result of decreased molecular mobility, and the molecular mobility at any temperature depends on remaining free volume, bulk and shear deformation [4, 5]. In such a case, free volume is the parameter that determines the rate of rearrangement and transport of polymers, consequently their diffusion and viscosity [3]. As the free volume decreases with increasing pressure, mobility on the fractional free volume decreases [3].

Similar to the approach described for the time-temperature superposition, we try to develop an analogous model for our system, not with time and temperature, but with the parameters that control the viscoelastic behavior of hydrogels. The viscoelastic behavior of

polymers is controlled by the mobility of chains, which depends on the free volume. The viscoelastic properties of hydrogels are governed by water transportation. Water transport in hydrogels depends on the volume fraction of the polymer in the network. Therefore, in both polymers and hydrogels, the viscoelastic behavior is determined by how much of the volume is occupied by the chains and how much is free or filled with water. When surface-attached hydrogels are compressed, the volume occupied by water in the network reduces. By increasing the applied pressure, due to the influence of confinement and decreased water volume, the layer becomes less compressible.

For variables affecting the free volume, relations analogous to WLF equations might be written. Therefore, a derived WLF-similar relation can be extended to give the shift a_{12} from state 1 to state 2, in terms of the free volumes f_1 and f_2 in these states [3]:

$$\log a_{12} = \frac{B}{2.303}\left(\frac{1}{f_2} - \frac{1}{f_1}\right) \qquad (4\text{-}3)$$

In this equation, B is an empirical constant.

If state 1 represents the sample compressed by pressure p_0 and 2 refers to the higher pressure p, above equation can be written as below [3] :

$$\log a_p = \frac{B}{2.303}\left(\frac{1}{f_p} - \frac{1}{f_0}\right) \qquad (4\text{-}4)$$

Compressibility is defined as the change in volume in response to the applied pressure ($\beta = -\frac{1}{V}\frac{\Delta V}{\Delta p}$). Free volume influences compressibility, thus, the compression of the free volume and the occupied volume would become more difficult by increasing pressure. If we consider compressibility to be constant in a small range of pressure, then f_p can be written as [3] :

$$f_p = f_0 - \beta(p - p_0) \qquad (4\text{-}5)$$

Substituting f_p in eq. (4-4) will give eq. (4-6):

$$\log a_p = \frac{{}^{B}/_{2.303 f_1}\,(p - p_0)}{{}^{f_0}/_{\beta} - (p - p_0)} \qquad (4\text{-}6)$$

At a first approximation, for one dimensional compression, compressibility can be written as a function of penetration depth and thickness ($\beta = -\frac{1}{h}\frac{\delta}{\Delta p}$).

Substituting $\Delta p = -\frac{\delta}{h\beta}$ in equation (4-6) and assuming $\delta_0 = 0$, gives a relation between the shift and confinement:

$$\log a_p = \frac{-{}^{B}/_{2.303 f_0}\,({}^{\delta}/_{h})}{f_0 + ({}^{\delta}/_{h})} \qquad (4\text{-}7)$$

Thanks to this latter relationship between the shift factor (a_p) and the confinement $({}^{\delta}/_{h})$, we propose to merge the curves similarly as in the time-temperature equivalency principle.

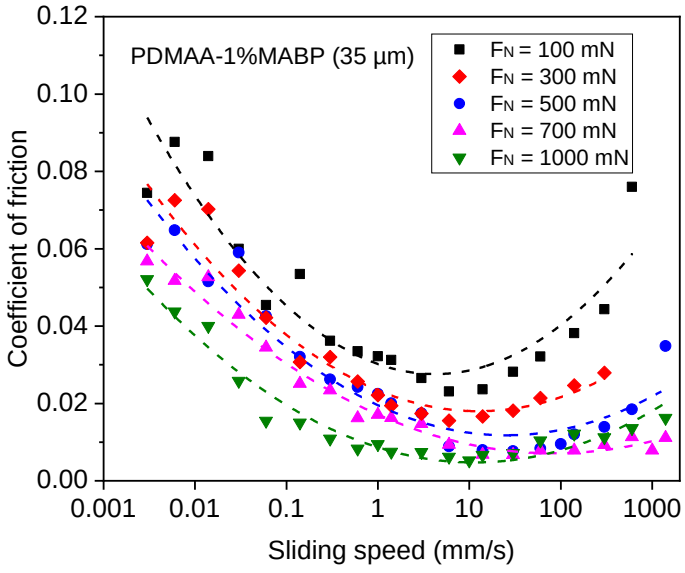

Figure 4-2 Merged curves from friction tests done on four samples with different thicknesses by shifting along the horizontal axis.

The thinnest sample (35 µm) is taken as the reference and the curves measured for the other three samples (47 µm, 52 µm, and 74.6 µm) are shifted to higher sliding speeds in such a way that the individual curves of the coefficient of friction overlap to the greatest possible extent with the corresponding composite curves. In Eq. (4-7), *B* is an empirical constant which is used to find the best fit to the equation which relates confinement, shift factor and water content.

Thus, the obtained value for *B* was different for each sample. Figure 4-2 shows the master curve as a result of shifting the curves of Figure 3-26 along the horizontal axis and superimposing them in regions of overlap. By shifting the curve along the x-axis, we can predict the friction for the 35 µm thick sample at higher sliding speeds that are not achievable with our test setup. After merging the curves for each applied load, it can be seen that there are vertical and horizontal shifts in the curve by increasing the normal load, which is going to be discussed in the next section.

To verify if the curves occurring at different normal loads are parts of one single curve, all the minimum points were brought at the same coordinate. This can be done if the friction force or coefficient of friction is normalized by dividing the value of friction force or COF by the minimum force (F/Fmin) or COF value (COF/COFmin) and sliding speed is divided by the sliding speed corresponding to the minimum friction (v/v_{Fmin}). Apparently, all the curves overlap, tending to show that the behavior is governed by the same phenomena.

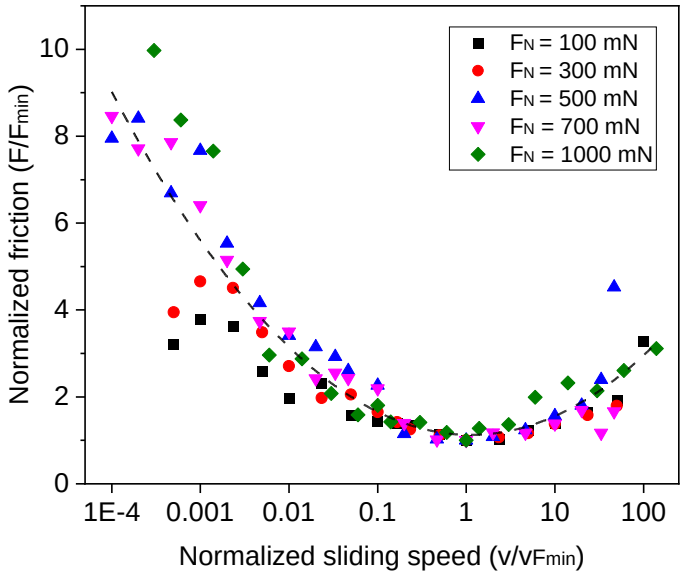

Figure 4-3 Master curve to predict the universal frictional behavior of two surface-attached hydrogel pairs as a function of sliding speed. The given curve is the superposition of 480 experimental measurements that were carried out on four samples.

4.3 Lubrication regimes

When we compare the contact of two soft hydrogel layers, it has to be considered that in a soft contact, asperities can deform easily, and there is no high resistance of asperities against deformation like plowing. Moreover, water as the fluid phase in hydrogels is a low viscosity

liquid, which denotes the probability of having a similar mechanism to the hydrodynamic lubrication is rather low. Hence, the Stribeck curve might not be the proper model to describe the lubrication of hydrogel pairs.

Among different lubrication mechanisms proposed for the cartilage is biphasic lubrication or interstitial lubrication, where the friction force is considered to be the direct consequence of the interaction between an elastic solid phase and an incompressible fluid phase [86,98,99,158]. The fibrillar structure of articular cartilage induces anisotropic properties to this tissue [38]. According to previous studies, articular cartilage is stiffer in tension than compression [38]. Similarly, in our surface-attached hydrogel system, the hydrogel network is difficult to compress due to the influence of the stiff substrate. Moreover, chains are connected to each other in a network and attached to a substrate. Consequently, surface attachment and being in a network limits the compressibility and stretchability of the chains.

According to our experimental results, the friction reduces by increasing the sliding speed, then, it reaches a minimum value and rises after the minimum. In section 4.1, different components of the friction force have been discussed. The friction force consists of components due to elastic stresses and fluid pressure. It was also shown that compared to the friction force, the adhesion is negligible between the surface-attached hydrogel pairs. Thus, the main forces are the forces due to the deformation of the polymer network and the water that has to be displaced.

The lubrication mechanism can be explained in light of these two forces. When the sliding is slow, or the permeability is high, or the sample thickness is small, the water in the network can be displaced easily, so there is not a significant resistance of water against sliding. Therefore, the main force at low sliding speed is the polymer deformation. Polymer deformation force depends on the penetration depth and apparent elastic modulus. As the sliding speed increases, the penetration depth becomes smaller and after a specific sliding speed, it does not change considerably, as shown in Figure 3-27. This reduction in penetration depth leads to smaller friction force (Figure 4-4) and thus smaller coefficient of friction. Penetration depth and thickness of the sample directly affect the contact stiffness or effective elastic modulus of the system. As it was evidenced by our elastic modulus measurements in section 3.2.1, the contact becomes progressively stiffer as the penetration depth to thickness ratio gets larger. Drag force starts to add up to the polymer deformation force as the slider slides faster than the relaxation

time of the compressed zone. So the water cannot be squeezed out of the network completely. The remaining water to displace in the network imposes a resistance against sliding, which results in a higher friction force at higher sliding speed (Figure 4-4). In this regime, presumably, there is no water layer separating the two countersurfaces completely like in hydrodynamic lubrication. Instead, water exists in the interfaces as the hydrogel itself has water inside the network (including the interface) which has not yet squeezed out. This results in a similar effect as hydrodynamic lubrication, although COF does not follow exactly the same power law as in hydrodynamic lubrication ($\mu \sim v^{1/2}$) [116].

As the applied load increases in this regime, the coefficient of friction becomes less speed dependent since the water in the interface reduces. As a result, the lubrication of surface-attached hydrogels occurs in two main regimes that we called polymer deformation controlled regime and drag controlled regime. These two regimes are illustrated in Figure 4-4b. The minimum is shifted as the applied force is increased. The minimum happens at different sliding speeds depending on the permeability and confinement of the system.

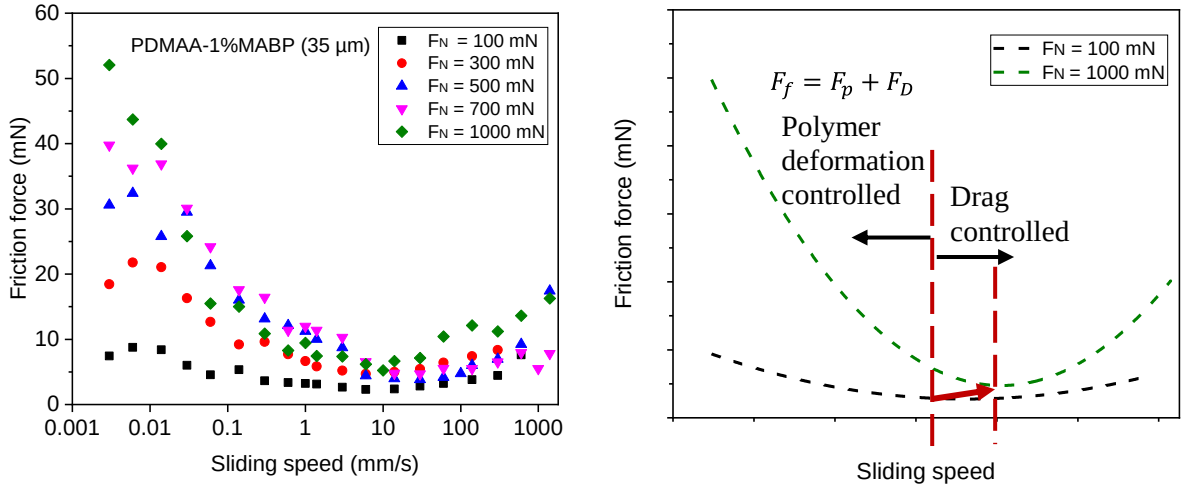

Figure 4-4 a) Friction force obtained from friction tests with the nanoscratch setup at different sliding speeds b) Different lubrication regimes controlled by the two main forces (Polymer deformation force and Drag force). The red arrow shows the shift in minimum by changing the normal load.

Drag force appears only at high speeds, so the two forces can be considered separately. In order to estimate the polymer deformation force, the Hertz theory can be helpful. This theory can predict the force required to compress a material to specific penetration depth. Although surface-attached thin layers deviate from the Hertz theory, we consider the contact stiffness which accounts for the confinement and sliding speed. We propose to write the polymer

deformation force, F_p , as proportional to the normal force component obtained by the Hertz theory, which the layer is under compression by an indenter with radius, R, and penetration depth δ. However, considering that the contact stiffness (E_{eff}) depends on δ/h and v, which results in non-Amontonian frictional behavior.

$$F_p \propto \frac{4}{3} E_{eff}(v, \frac{\delta}{h}) R^{1/2} \delta^{3/2} \quad (4\text{-}8)$$

In this equation, E_{eff} is the effective elastic modulus or contact stiffness which is a function of confinement and sliding speed. Penetration depth is also a function of sliding speed and confinement which is incorporated in the contact stiffness.

The drag force that appears as a result of the fluid phase in the polymer matrix can be estimated by Darcy's law. According to Darcy's law, velocity of flow (v) is directly proportional to the permeability (k), pressure change (dP) and inversely proportional to the path length (dx).

$$\frac{dP}{dx} = \frac{v}{k} \quad (4\text{-}9)$$

As demonstrated in Figure 4-5, if the distance of each streamline from the axis of symmetry assumes to be r with a speed of $\dot{\delta}$ in the compression direction, volume conservation gives the velocity as a function of the starting point, *r*, and angle, θ [159]:

$$v(r, \theta) = \frac{\dot{\delta} r}{a - (a - r)cos\theta} \quad (4\text{-}10)$$

To get the pressure acting on the slider, Darcy's law can be integrated along each streamline [159].

$$P(r) = \int_0^{\pi/2} \frac{\dot{\delta} r (a - r) sin\theta}{k(a - (a - r)cos\theta)} d\theta + \int_0^{\pi/2} \frac{\dot{\delta} r (a - r)}{k(a - (a - r)cos\theta)} d\theta \quad (4\text{-}11)$$

Then, the drag force can be considered proportional to the load supported by the fluid phase in indentation tests as given in the following equation [159]:

$$F_D \propto \frac{4}{3k}\dot{\delta}a^3 \tag{4-12}$$

Replacing $\dot{\delta} = v\delta/a$ for a sliding contact, the drag force will be:

$$F_D \propto \frac{4}{3k}vR\delta^2 \tag{4-13}$$

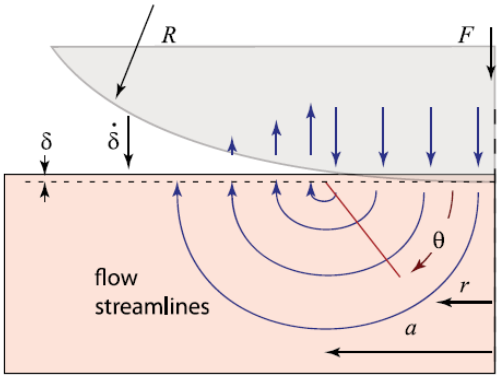

Figure 4-5 Schematic illustration of the contact model for flow-induced force calculation using Darcy's law [159].

Due to the effect of confinement, the equation for the drag force has to be modified. In comparison to a semifinite case, the permeability of the hydrogel will be continuously lowered by further compression. High confinement will result in a higher segment density and therefore, lower effective permeability ($k_{eff}(v,\frac{\delta}{h})$). The drag force can be written as:

$$F_D \propto \frac{4}{3k_{eff}(v,\frac{\delta}{h})}vR\delta^2 \tag{4-14}$$

The ratio of the two forces (F_D and F_p) can give a dimensionless characteristic number to determine the lubrication mechanism (analogous to the Sommerfeld number in the Stribeck curve) [42,53,55]. In some investigations about the lubrication of articular cartilage, the characteristic number has been named Peclet number [38,39,84,159], although the Peclet number describes a different phenomenon. The original Peclet number has been defined as a dimensionless number to describe transport phenomena, or more precisely, the ratio of the rate of advection to the rate of diffusion. To determine whether the interstitial lubrication in articular cartilage is maintained or not, the Peclet number has been used [39]. According to the articular cartilage studies, interstitial lubrication is active when $Pe \gg 1$, however, the load supported by the fluid phase reduces as the fluid transportation out of the tissue occurs. Therefore, most of the load is supported by the solid phase when $Pe \ll 1$ [39].

As we described in Figure 4-4b, the ratio of the two force components can determine the main force component of friction. We have called this ratio as a force characteristic number which is proportional to the Peclet number.

$$\frac{F_D}{F_p} \propto \frac{vR^{1/2}\delta^{1/2}}{k_{eff}(v,\frac{\delta}{h})E_{eff}(v,\frac{\delta}{h})} \tag{4-15}$$

$$Pe = \frac{va}{k_{eff}(v,\frac{\delta}{h})E_{eff}(v,\frac{\delta}{h})} \tag{4-16}$$

The force characteristic number is directly proportional to the sliding speed, contact radius and inversely proportional to permeability and stiffness. This equation explains that if the sliding speed or contact size increases, the drag force is the influential force and lubrication is shifted to the left side of the curve. A decrease in permeability and elastic modulus would lead to a similar effect.

Both permeability and elastic modulus are functions of confinement and sliding speed through the change in penetration depth. When a sample is highly confined, the effective elastic modulus is higher than the sample with low confinement. In contrast, increased polymer fraction leads to lower effective permeability.

In our experiments, the contact stiffness or effective elastic modulus is the parameter that has to be considered. However, in most of the studies, the attempts are to extract the elastic modulus of the thin film from the measured effective elastic modulus obtained by the indentation test. Different analytical, semi-analytical and empirical equations have been suggested as relations connecting the composite elastic modulus, film and substrate elastic moduli, even though, these equations are not applicable for any combination of film and substrate [59,160–162].

In our system, where a thin hydrogel layer is attached to a glass substrate, at a very small penetration depth, close to zero equivalent elastic modulus is equal to the elastic modulus of the hydrogel. When confinement ($\frac{\delta}{h}$) is close to one, the equivalent elastic modulus must be close to the elastic modulus of the substrate, in this case, glass (E_{glass}). Therefore, depending on the confinement, the effective elastic modulus starts from the elastic modulus of the

hydrogel, increases subsequently and finally ends at the elastic modulus of the glass. This behavior is shown schematically in Figure 4-6.

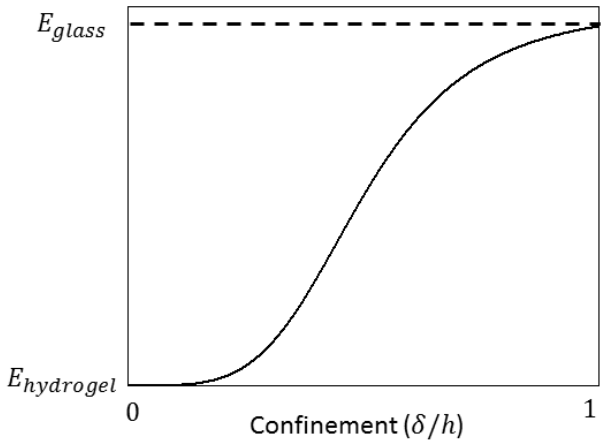

Figure 4-6 Effective elastic modulus, starting from elastic modulus of hydrogel at low confinement and reaching the elastic modulus of glass at high confinqqement.

In section 3.2.1, we have shown the influence of confinement on the effective elastic modulus, however, the range we were able to measure with AFM was very limited and lower than the confinement we are dealing with in our friction tests. Figure 4-7a shows elastic modulus as a function of confinement, which is obtained from the indentation test with the AFM. The effective elastic modulus varies from about 50 kPa to 3.2 MPa as the confinement changes from 0.01 to 0.1. Such a significant change at very low confinement indicates the strong influence of the glass substrate. Experimentally, the range of confinement that was accessible with AFM is limited. Moreover, adjusting the contact point with the nano-indenter, which is crucial in this measurement, is not possible. The elastic modulus of the hydrogel layer is about 50 kPa, whereas the elastic modulus of glass is about 80 GPa. Due to such a huge difference and the limited experimental data range, we have avoided including the elastic modulus of glass in the linear fit. Moreover, we tried to have only one fitting parameter. Therefore, we have estimated the effective elastic modulus by fitting the function given in Eq (4-17) to the experimental data.

$$E_{eff} = E_{hydrogel} + (A - E_{hydrogel})(\frac{\delta}{h}) \qquad (4\text{-}17)$$

In the above equation, A is an empirical constant obtained by the fit. After fitting this equation to the experimental data, A is equal to 25.7 MPa. The R square value of the linear fit is 0.9.

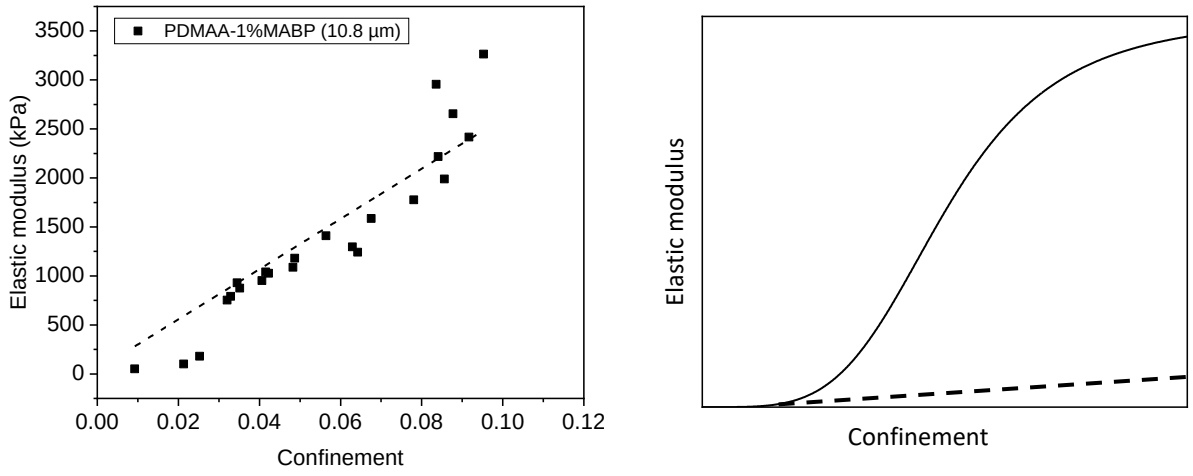

a) b)

Figure 4-7 a) Measured elastic modulus (E_{eff}) as a function of confinement. The dashed line in this plot is a linear fit according to eq. (4-17) b) Black curve shows the expected trend of the effective elastic modulus schematically and the dashed line shows how the linear fit predicts the elastic modulus and deviates at high confinement values.

We acknowledge that the predicted effective elastic modulus with the linear fit underestimates the value of the effective elastic modulus, as depicted in Figure 4-7b schematically. For more precise estimation, the effective elastic modulus has to be measured in higher confinements, which could not be realized by AFM. For this purpose, a different investigation technique has to be utilized.

The force characteristic number is calculated by substituting the sliding speed, penetration depth, radius of the slider, estimated effective elastic modulus, and permeability obtained from the permeation tests. It has to be admitted that effective permeability of the surface-attached layers is also a function of confinement. However, we substituted the constant value measured on a bulk hydrogel. The coefficient of friction is shown against the force characteristic number in Figure 4-8. The minimum COF occurs at values between 1 and 10. Having an unprecise value for the effective elastic modulus and effective permeability is the source of error for our calculations. Thus, the Pe value where minimum friction happens cannot exactly be predicted. Regardless of precise value for the Pe number, we can say that at low Pe value, polymer deformation is the main force and lubrication is at polymer deformation controlled regime. For high Pe number, the lubrication is in drag controlled lubrication regime.

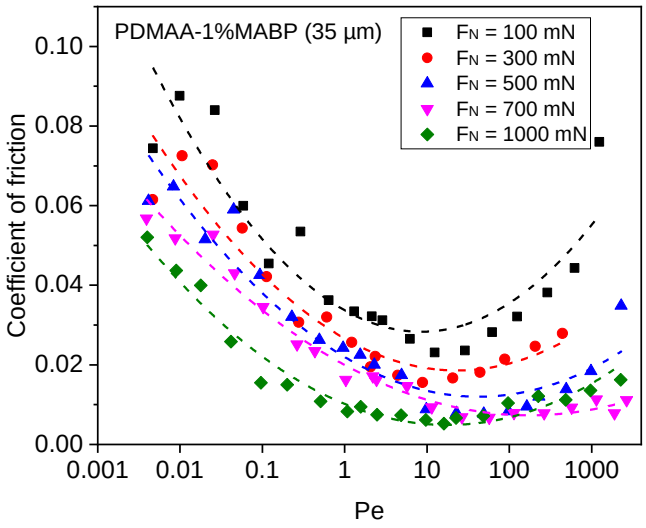

Figure 4-8 Coefficient of friction versus calculated force characteristic number. The force characteristic number can predict the governing lubrication regime of hydrogels.

Finally, we used eq.(4-8) and eq. (4-14) to estimate the drag force and the polymer deformation force. When the confinement is low, the obtained value for the polymer deformation force is in the same order as the value obtained experimentally. For higher confinements, the value of the polymer deformation force is underestimated as a result of the underestimated effective elastic modulus. As it has been discussed, effective permeability for confined hydrogels must be larger than the one obtained experimentally on a bulk sample. Thus, the calculated drag force is two orders of magnitude higher than the experimental values. With effective elastic modulus and permeability, the two equations presented for drag force and polymer deformation force are expected to give a good prediction of the friction force. The proposed model enables the description of the lubrication behavior of the surfaces covered by surface-attached hydrogels. Furthermore, it clearly shows which parameters are the influential parameter on the frictional properties. However, for a precise calculation of the forces further investigations are required.

4.4 Limited compressibility

There are different parameters that can induce nonlinearity to the friction force of hydrogels. These parameters are limited stretchability of chains and the presence of water in the polymer network. For surface-attached hydrogels, there are more parameters such as osmotic pressure and confinement that reduce the compressibility. These parameters are discussed in the upcoming sections.

4.4.1 Influence of chain stretchability and slider geometry on compressibility

When the hydrogel layer is compressed, the polymer network undergoes conformational changes. In a perturbed region, there are chains that are compressed and chains that are stretched as in Figure 4-9.

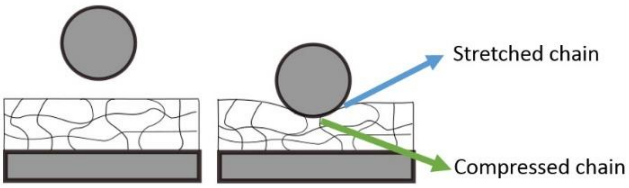

Figure 4-9 Stretched and compressed chains presented schematically as the hydrogel layer is under compression.

As illustrated in Figure 4-10, an ideal chain (where there is no interaction between the monomers) can be considered as a spring [163]. A chain initially possesses a coiled shape. As the chain is stretched, Hooke's law can be considered to be valid where there is a linear relationship between the applied force and the extension of a chain (i.e., small extension) [163]. Then, the force needed to hold two ends of a chain by distance *l* is as follows:

$$F_{ext} = \frac{3k_BT}{Nb^2}\, l \qquad (4\text{-}18)$$

Here $k_b$is the Boltzmann constant, *T* is temperature, *N* is the number of monomers, *b* is the Kuhn length and *l* is the end to end vector. Since in a fully stretched state, the end to end vector will be $l_{max} = Nb$, equation (4-18) can be written as [163]:

$$\frac{l}{l_{max}} = \frac{F_{ext}b}{3k_BT} \qquad (4\text{-}19)$$

Further stretching of the chain leads to nonlinearity of this relation, as given in equation (4-20) [163].

$$\frac{l}{l_{max}} = 1 - \frac{k_BT}{F_{ext}b} \qquad (4\text{-}20)$$

So it can be concluded that even bulk hydrogels might demonstrate a degree of nonlinearity in the friction force under high applied pressures where chains are strongly stretched and compressed.

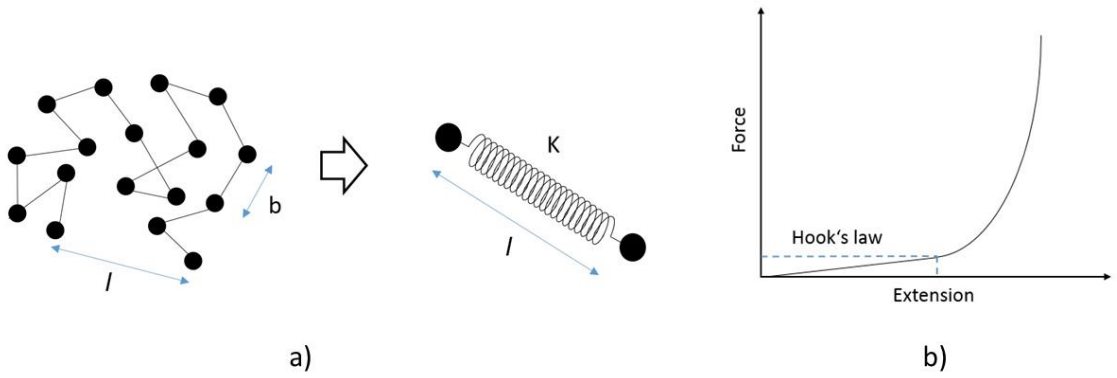

Figure 4-10 a) Assuming a chain as a spring with stiffness K and length *l* b) Linear relationship between force and extension at low extensions and nonlinear behavior at stronger extensions.

Chain extension has been calculated using the penetration depth (δ) that has been recorded during the friction tests by considering the two circle segments (green and blue) presented in Figure 4-11. The blue segment is equivalent to the Hertz theory, in which the contact radius can be calculated by penetration depth and radius of the slider ($a = \sqrt{R\delta}$). The green segment is with the assumption that there is no deformation happening on the indenter. So initial length and stretched length are calculated using penetration depth.

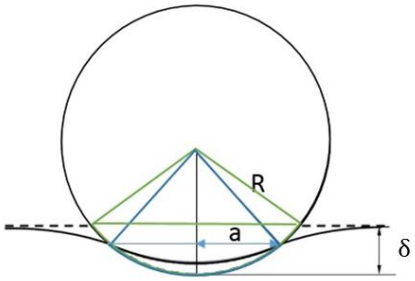

Figure 4-11 Segments of circle that are considered to calculate the chain stretching. Blue segment is with considering the contact radius as in Hertz theory and green segment is the geometrical calculation.

Then, the chain stretching in the blue segment is given by equation (4-21):

$$\frac{\Delta l}{l} = \frac{R(Arcsin\left(\frac{a}{R}\right)) - a}{a} \tag{4-21}$$

Chain stretching for the green segment of the circle is as below:

$$\frac{\Delta l}{l} = \frac{R(Arccos\left(\frac{R-\delta}{R}\right)) - \sqrt{R^2 - (R-\delta)^2}}{\sqrt{R^2 - (R-\delta)^2}} \tag{4-22}$$

In both cases, chain extension (Δl) is ranging between 10^{-8}-10^{-7} m, leading to the strain ($\frac{\Delta l}{l}$) of around 10^{-5} -10^{-4}.

The force to extend a coil-shaped chain can be obtained using Hooke's law. As the strain is very small, we can estimate the force required for such a strain by means of eq. (4-19). Characteristic ratio (C_∞) for poly (acrylamide) is 12.7. The bond length is assumed to be about 1 Å and the bond angle is around 109°. Then the Kuhn length can be obtained using equation (4-23) as follows:

$$b = \frac{C_\infty l}{\cos {}^{\vartheta}/_{2}} \qquad (4\text{-}23)$$

The Kuhn length will be 21.89 Å, which is the segment size of a real polymer chain. The required force for a 10^{-4} extension is 10^{-13}-10^{-12} N, which is much smaller than the applied force and the friction force, therefore, chain extension is negligible in our system. However, chain extension should be strongly dependent on the geometry of the slider. In our experiments, the radius of the slider is relatively large (25.94 mm) which results in a very small extension of the chains. Using a different geometry such as a flat punch or a sphere with a smaller radius can significantly enhance the extension and finally leads to the rupture of the chains. Spherical sliders are not geometrically similar, meaning that the ratio of contact radius to the radius of the slider (a/R) changes by changing the applied load [164,165]. By increasing the applied load, the angle of the chain stretching force becomes larger, thus, the vertical component of chain stretching gets larger. When a slider with a smaller radius is used, this change in the angle happens faster, leading to a stronger chain stretching, as shown schematically in Figure 4-12. The same contact pressure can be obtained when the ratio a/R is constant [165]. On the other hand, in the case of a flat punch, chain stretching is extremely large at the corners due to stress concentration on the sharp edges of the slider. The sharp edge leads to a singularity in the stress field at the edge of the circle of contact [165]. This might result in plastic deformation and rupture of the gel layer.

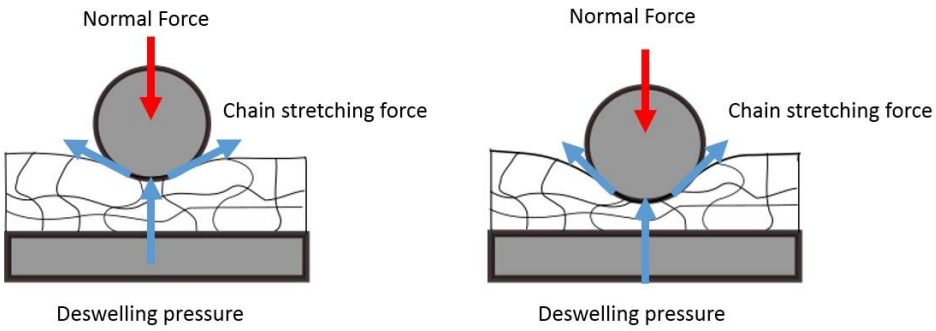

Figure 4-12 Influence of increased penetration depth or smaller slider radius (a/R parameter) shown schematically.

The relation between the applied force and indentation depth might be written in a general form as given below [166]:

$$F_N = XE\delta^n \qquad (4\text{-}24)$$

Here F_N is the applied load, X is the geometry factor, E is the elastic modulus, δ is the penetration and n is the deformation index [166]. Eq. (4-24) is summarized for different shapes of indenters in Table 4-1 [165]. Considering the equations given in Table 4-1, for a flat punch, penetration depth changes linearly with the applied force. The dependence of penetration depth to the applied load increases with a power of two for a conical indenter. Thus, stretching of the chains is strongly dependent on the shape and size of the slider. As a consequence, a change in the geometry of the slider might lead to different observations.

Table 4-1 Relation between the applied load and penetration depth for different slider geometries [164].

Slider geometry	Force and penetration depth relation
Cylindrical flat punch	$F_N = 2Ea\delta$
Spherical slider	$F_N = \frac{4}{3}E\sqrt{R}\delta^{3/2}$
Conical slider (with angle θ)	$F_N = \frac{2}{\pi}E\tan\theta\,\delta^2$

4.4.2 Influence of water and confinement on the compressibility

The presence of water as an incompressible fluid inside the network leads to incompressibility at higher sliding speed as water stays in the network and avoids further penetration, which can clearly be seen in Figure 3-28. At higher sliding speeds, friction force remains almost constant and changes only slightly by changing the normal load. This behavior is the result of almost constant penetration depth as a consequence of residual water in the network.

Similar to the cartilage which shows a time-dependent recovery after the deformation due to interstitial fluid displacement [167,168], it has been observed through contact visualization between a spherical glass slider and a hydrogel sample that the contact shape is velocity dependent [93,124]. Alike a static state (i.e., indentation test) at slow sliding speeds, the observed contact shape was circular [93,124] following the Hertz theory [93,169], although the contact gets smaller and asymmetric at higher sliding velocities. During fast sliding, the rear

edge loses its contact to the slider, while the front edge remains circular similar to viscoelastic material (illustrated in Figure 4-13) [93,124]. The viscoelasticity in hydrogels is essentially induced by the fluid phase in the network which makes the deformation and the recovery afterward time-dependent. Therefore, during fast sliding penetration depth decreases due to the generated lift force by the fluid pressurization. So the rear edge of the contact cannot retain its initial shape and the contact becomes asymmetric. Losing contact and smaller contact area at high sliding speeds can explain the low load dependence of the friction force.

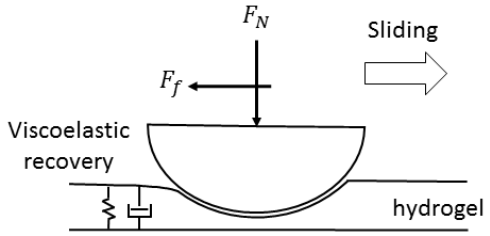

Figure 4-13 Viscoelastic behavior induced by the fluid phase and contact asymmetry at high sliding speeds [93,124].

5 Lubrication of textured hydrogels

5.1 Introductory remarks

In many mechanical components, surface textures such as dimples and grooves are typically introduced to improve the tribological performance [125,170]. Proper selection of patterns and their dimensions can lead to lower friction force and consequently longer lifetime and higher efficiency [171]. For instance, mechanical seals, tires, and journal bearings are designed with controlled surface patterns to change the frictional properties [170,172].

The physics of sliding friction for wet, patterned surfaces is challenging. When the interfaces are soft lubricated surfaces, it is even more complicated due to coupling of solid deformation through normal and shear load and fluid dissipation. Previous studies have revealed that the lubricant film generates fluid pressure that lifts and deforms the solid surfaces on patterned surfaces, resulting in elastohydrodynamic lubrication [170]. It has been shown that geometric shape and orientation affect the load-carrying capacity of contacting surfaces [125].

In this chapter, we aim to investigate the influence of surface texturing on the frictional behavior of surface-attached hydrogels. Hence, grooves have been generated on the surface of surface-attached hydrogel samples. The effect of pattern size and pattern direction has been studied. Presumably, grooves can function as lubricant supplies and also channels to facilitate the flow of lubricant during sliding.

5.2 Generation of textured hydrogels

To generate textured hydrogels, first, silicon wafers are patterned by means of standard lithography to produce the PDMS stamps that are negative replicas of the silicon wafers. The patterning process of silicon wafers is described in detail in the experimental chapter (see chapter 10). The resulting textured surfaces serve as molds for the fabrication of PDMS textured substrates. PDMS textured surfaces are prepared by pouring Sylgard 184 with added curing agent (ratio 10:1 w/w%) onto the wafers and curing at a temperature of 80°C overnight.

In order to prepare the textured hydrogels, 200 µl of the polymer solution (PDMAA 1%MABP dissolved in ethanol with a concentration of 300 mg/ml) is poured on each PDMS stamp. After 15 minutes of degassing in a desiccator, a silanized glass substrate is pressed on the polymer solution and fixed with a tape. For the crosslinking process and simultaneous attachment to the substrate, the glass substrate was irradiated from the backside

with UV light (Oriel) ($\lambda = 365$ nm) with an irradiation dose of 30 J/cm^2. The PDMS stamps were peeled off after keeping the samples in the freezer overnight. The whole process is summarized in Figure 5-1.

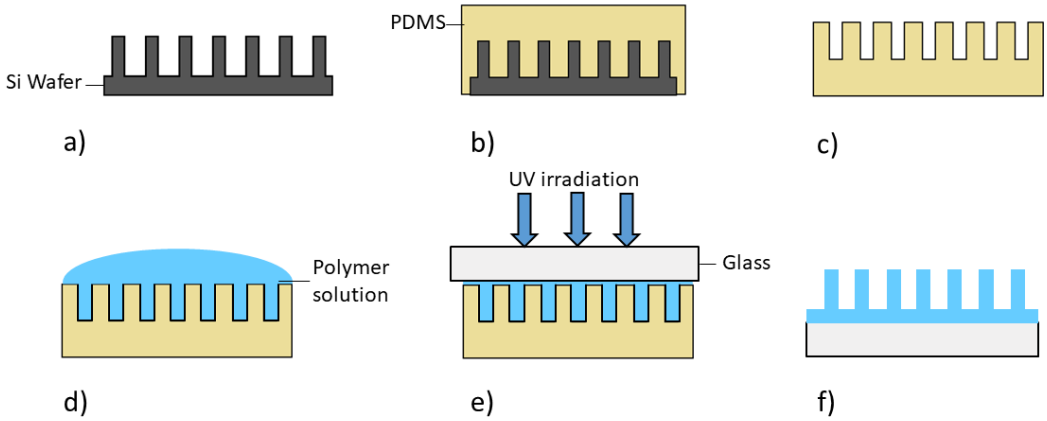

Figure 5-1 Summarized hydrogel texturing process: a) Silanization of master wafer to prevent PDMS/silicon adhesion b) Pouring mixture of silicone and curing agent (10:1) on master wafer, cure overnight at 80 °C c) Peel-off gently master wafer from PDMS stamp d) PDMAA- 1%MABP dissolved in ethanol (300 mg/ml) added on the PDMS stamp e) Press a silanized glass substrate on top and exposure with wavelength of 365 nm and energy of 30 J/cm^2 f) Samples frozen overnight and peeled off.

5.3 Influence of texture size and sliding direction

Surface-attached hydrogel samples containing stripes are produced, as explained in section 5.2. As it is demonstrated in Figure 5-2, the textured surface has stripes with width b, spacing a and height h = 30 µm. Friction tests were carried out between a hydrogel coated slider with a radius of 25.94 mm and a textured hydrogel sample in water. Friction forces were measured for two different normal forces (100 mN and 1000 mN) parallel and perpendicular to the structures as shown in Figure 5-2. The sliding speed was varied from 0.006 mm/s up to 3 mm/s. We have studied two cases: 1) where the structure density is constant, meaning the sum of spacing and structure width (a + b) is a constant value and 2) where structure spacing is kept constant and the strip width was changed. Since the structures are crosslinked in the dry state, the dimensions of the stripes are changed slightly after swelling in water. A flat sample with 35 µm thickness (presented in Chapter 3) is taken as a reference for comparison.

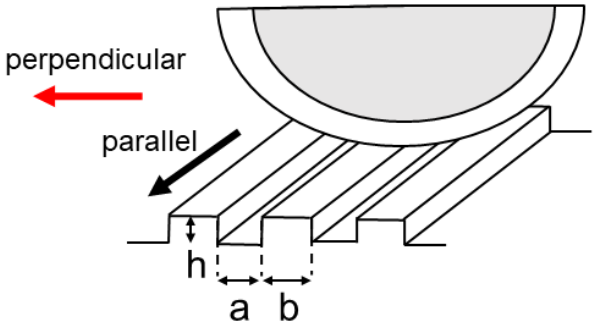

Figure 5-2 Textured hydrogel sample contains strips with width b, spacing a and height h. Friction tests were performed between a hydrogel coated slider and textured hydrogel in two different directions (i.e., parallel and perpendicular to the stripes).

In the first case, the density of the structures is kept constant, which means the number of structures in the contact region is the same under the same applied load. During all friction tests, the recorded penetration depth was below 30 µm, which indicates that the structures are deformed but not completely flattened. For the friction experiments, three samples with the following dimensions were produced: a= 50 µm, 60 µm, and 70 µm. So the stripe width, b, changes from 30 µm to 50 µm. Microscope images of these samples are shown in Figure 5-3 in the dry and in the wet state.

When the spacing between the structures is small, during swelling the structures change to a zigzagged shape, as there is not enough space between the stripes to swell (Figure 5-3b). Such structures are expected to behave like a continuous surface (flat sample), which is presented in section 3.6.2.2. For this sample, by changing the sliding speed, friction changes in a similar manner as that of a flat sample with a similar thickness (Figure 3-26). However, it should be noted that the values of the coefficient of friction are almost double of those the values measured for the flat sample, perhaps due to the many phase boundaries leading to surface irregularities and low cohesion of the material which may change significantly the stress distribution by local relaxation.

As shown in Figure 5-4, a decrease in the contact area by a simultaneous increase of spacing and reduction of structure size results in a friction force that is significantly smaller. This can be attributed to the fact that part of the contact always consists of pure water as a result of entrapment of water between the structures. Water is much easier to shear than the hydrogel itself. Therefore, the friction force will be noticeably lower for such water-lubricated contact.

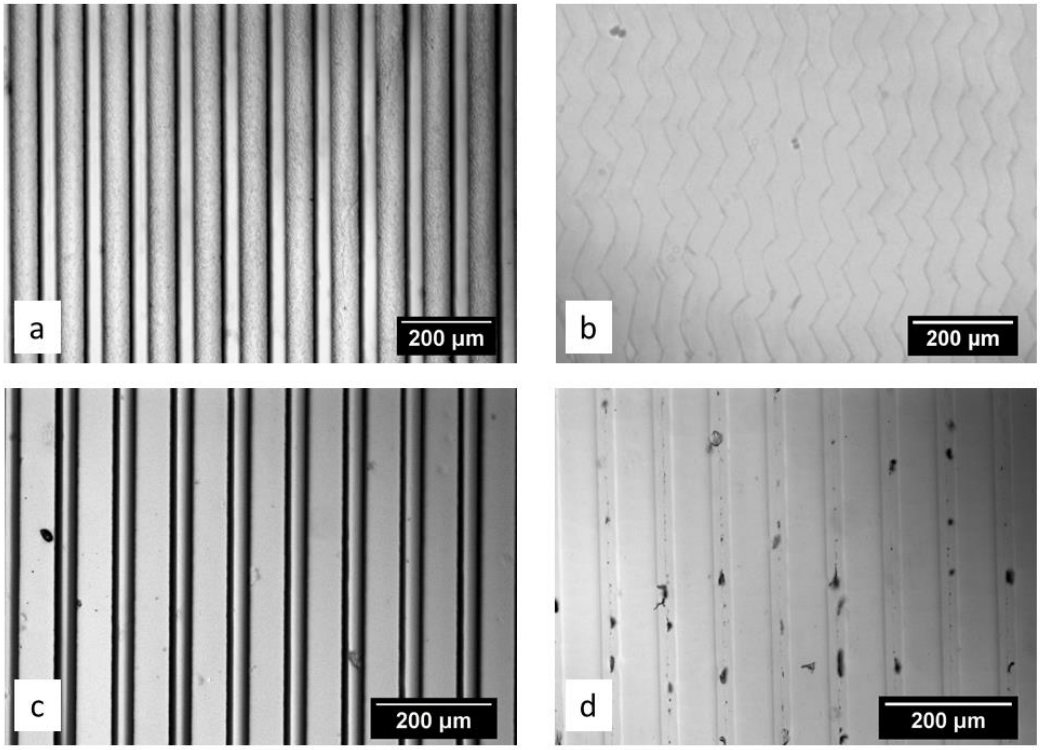

Figure 5-3 Optical microscope image of the samples with the same structure density. a) Dry state a = 50 µm, b =50 µm b) Wet state of sample in (a) c) Dry state a = 60 µm, b =40 µm and d) Wet state of sample in (c).

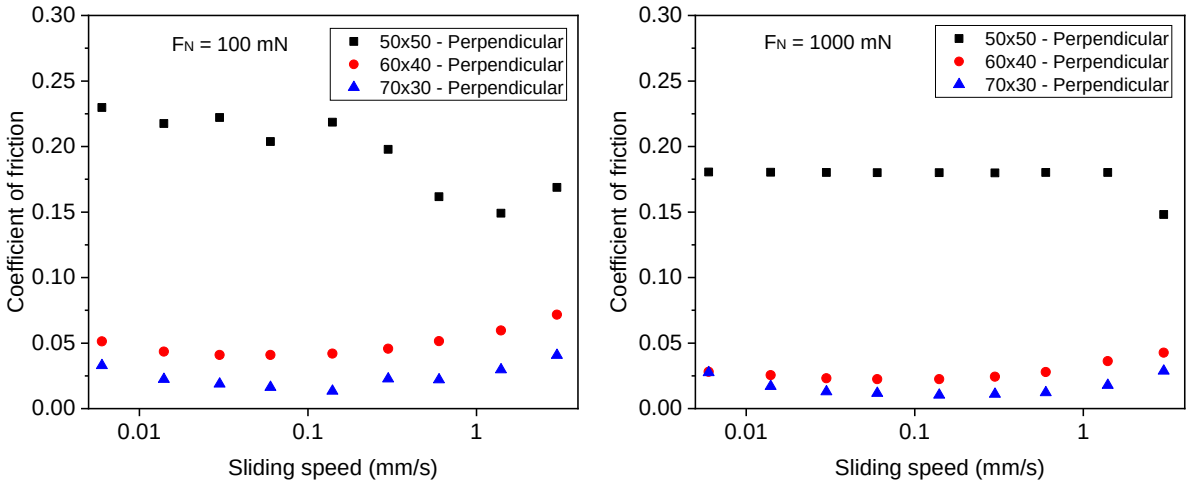

a) b)

Figure 5-4 Influence of reduction in contact area by increasing the spacing from 50 µm to 70 µm and decreasing the structure size at the same time a) F = 100 mN and b) F = 1000 mN.

We observed that the friction behavior is very different when sliding is performed parallel to the structures compared to orthogonal sliding (Figure 5-5). Although the general dependence of the COF on the sliding speed is very similar in the two samples, the absolute values vary by about a factor of two. When patterns are aligned with the sliding direction

(parallel sliding), water can easily be transported through the channels causing low resistance against shearing. The direction dependence of friction can be seen. Perpendicular sliding prevents free drainage of water and its displacement through the channels. It worth to note that in the perpendicular direction, the contact area is varying due to the configuration, whereas in the parallel situation, it is identical although constantly renewed.

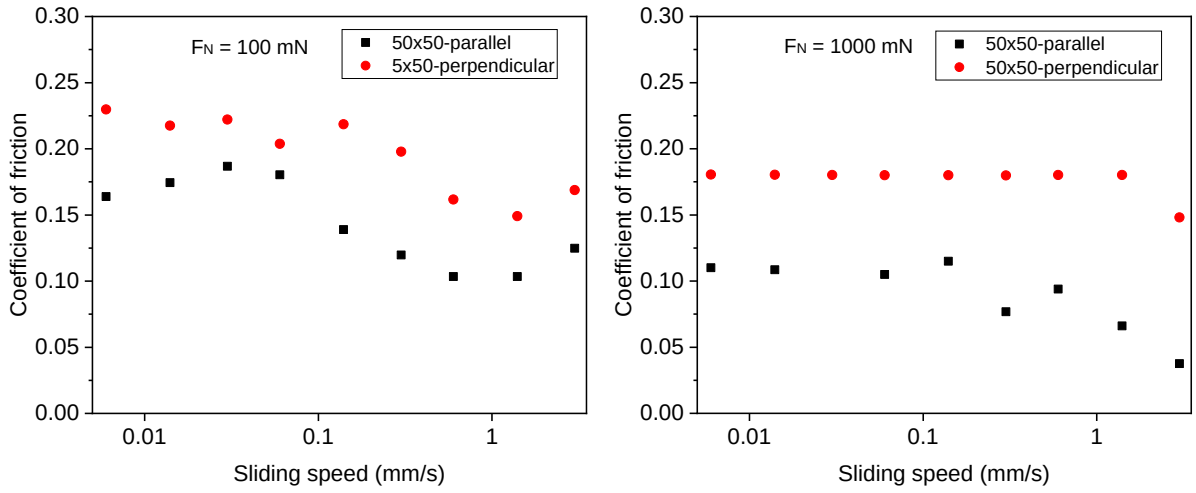

a) b)

Figure 5-5 Effect of sliding direction on the frictional behavior of tribopairs a) a = 50 µm and b = 50 µm b) a = 60 µm and b = 40 µm.

For further investigation of the friction as a function of the contact area, we have kept the spacing constant (a = 100 µm) and altered the pattern width (20 µm ≤ b ≤ 200 µm). Optical microscope images of these samples are depicted in Figure 5-6 in both dry and swollen states. Friction tests were performed parallel to the structures by applying a load of 100 mN and 1000 mN. In one of the previous samples (50 µm × 50 µm), which is shown in Figure 5-3b, the channels are blocked after swelling, thus friction is remarkably higher than the other samples. Moreover, the lubrication behavior resembles that of a flat sample with a similar thickness. However, the spacing is chosen large enough (a = 100 µm) so that there are always channels to direct the flow and keep the water inside the contact area. In Figure 5-7, the friction coefficient is plotted versus sliding speed for four samples with different pattern widths (20 µm, 60 µm, 140 µm, and 200 µm). For all samples, the lubrication is in the drag force controlled regime as water is present in the contact, leading to dependence of friction on the sliding speed. In contrast to our expectations, the lowest friction is observed at the largest structure width (200 µm). For the same contact area, 16 % of the contact is composed of hydrogels for the smallest structure width, while this value is about 66% for the sample with the largest structure width.

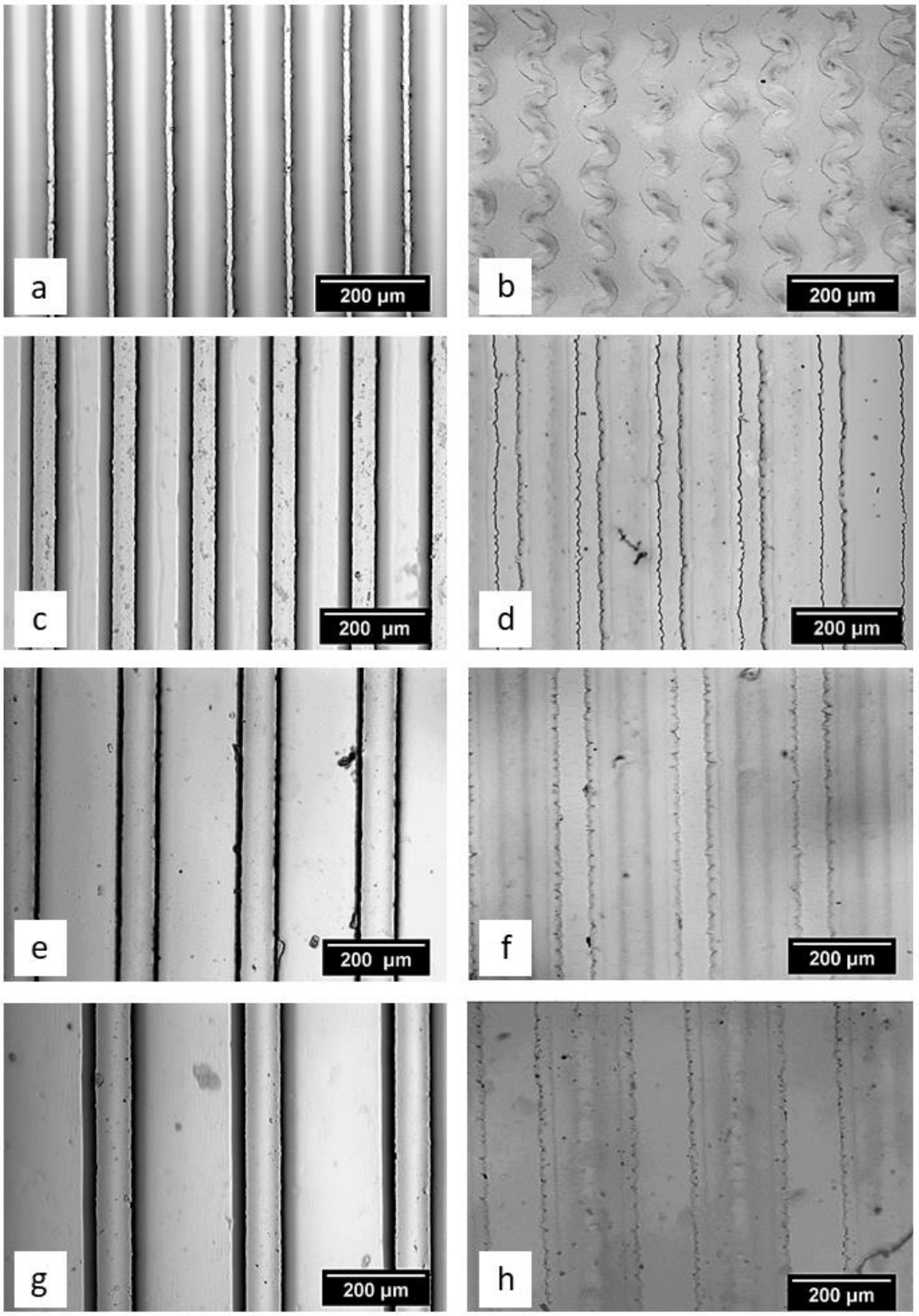

Figure 5-6 Optical microscope image of samples with 100 µm spacing and different pattern sizes in dry and wet state. a) Dry state of sample with a = 100 µm and b = 20 µm b) Wet state of sample (a) c) Dry state of sample with a = 100 µm and b = 60 µm d) Wet state of sample (c) e) Dry state of sample with a = 100 µm and b = 140 µm f) Wet state of sample (e) g) Dry state of sample with a = 100 µm and b = 200 µm h) Wet state of sample (g)

The lower friction for the sample with the largest width can be attributed to the ability of the structures to support the load. When the structures are narrow, they are easily deformed, so the water between the opposing surfaces can more easily be squeezed out. As a result, a lower percentage of the load will be supported by the interfacial water. Therefore, the reduction in the contact size is not the only influential parameter, but the structure width also plays an important role in the determination of the friction.

It can be concluded that in the presence of channels, the width of the channel seems not to have a critical role on the frictional properties, but it is the ability of structures to support the load that becomes the key factor. The sample with the wider structures undergoes smaller deformation, and thus the penetration depth is smaller in comparison to the sample with narrow structures. Therefore, the amount of displaced volume and friction is lower. It has to be noted that by increasing applied load to 1000 mN, the difference in friction force becomes smaller as the structures are largely deformed, and water is also squeezed out partially. Consequently, the introduction of surface patterns can cause a great difference in friction when the patterns are not strongly deformed.

At the lowest sliding speed, the friction force was below the detection limit of the machine at 1000 mN for the sample with 200 µm width patterns. So the value was set to the lowest possible value that can be recorded by the nanoscratch test (COF = 0.001).

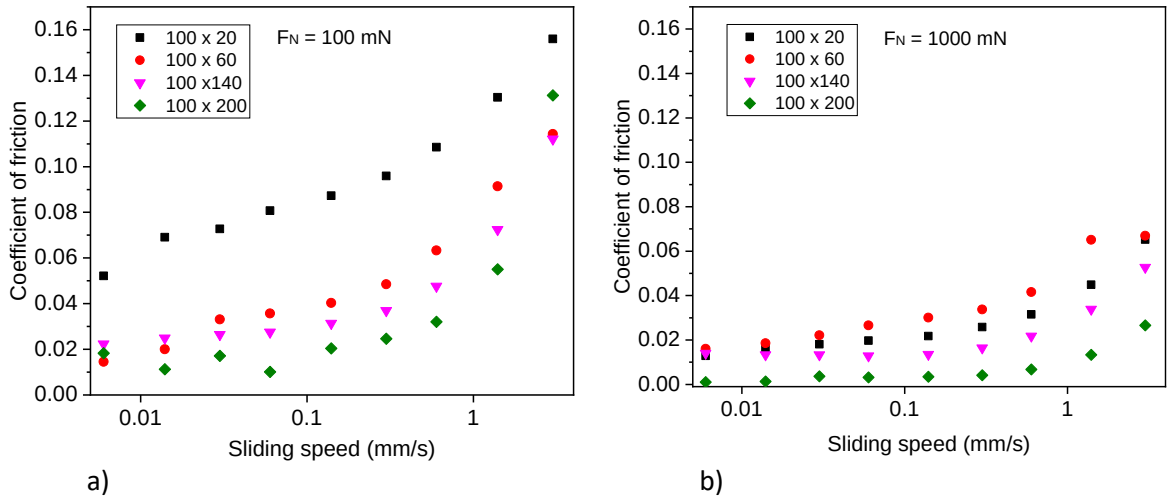

Figure 5-7 Coefficient of friction as a function of sliding speed for pattered surfaces with constant spacing a = 100 µm and different pattern width a) Applied load F = 100 mN b) F = 1000 mN.

To study the effect of pattern shape on the tribological behavior, a sample with dimples have been generated. Dimples on the surface of the sample (Figure 5-8a) are rectangular

cuboids with 100×100×30 μm^3 dimensions. The distance between the dimples is 100 μm. Similar to the channels, the idea of having dimples on the surface is to have them as lubricant supplies. From the microscope image in Figure 5-8b, it is not clear whether the holes are completely blocked after swelling or not. Results from friction tests with the nanoscratch setup are illustrated in Figure 5-9. Friction of this sample follows a similar trend as the samples with the grooves. This implies that the friction does not noticeably depend on the texture shape, as long as the contact is partially covered by water. There might be a change in friction depending on the structure size and shape, but the overall behavior is very similar for patterned hydrogels.

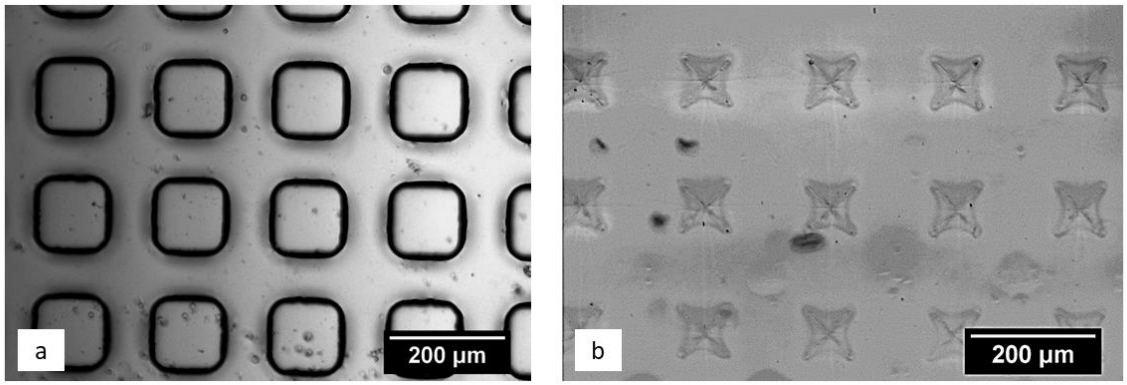

Figure 5-8 Microscope images of sample with cuboid holes (100× 100 × 30 μm^3) a) Dry state b) swollen state.

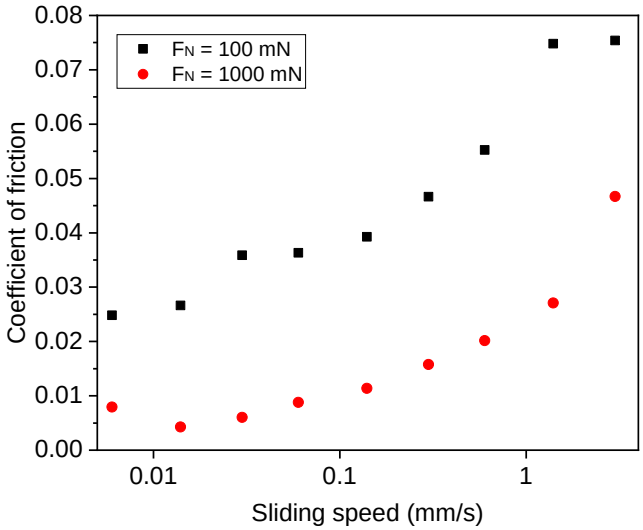

Figure 5-9 Friction coefficient as a function of sliding speed on a sample with cuboid dimples at two different normal loads.

5.4 Friction mechanism

The influence of surface patterns of surface-attached hydrogels on their lubrication can be understood this way: at low speeds, water in the hydrogel network squeezes out partially.

Simultaneously, the squeezed out water flows through the channels, reducing the resistance against sliding, leading to lower friction. As illustrated in Figure 5-10 schematically, water can be squeezed out more easily in the presence of channels as the distance water has to be transported is much shorter than that of the flat sample. As a consequence of the shorter displacement distance, the dependence on sliding speed is also less than that of the flat sample. At high speeds, water cannot be squeezed out, giving rise to the drag force. In all patterned surface-attached hydrogels, when water was present between the countersurfaces, the lubrication was in a drag controlled lubrication regime. Therefore, patterns on soft surfaces can be used to alter lubricated friction and reduce friction considerably.

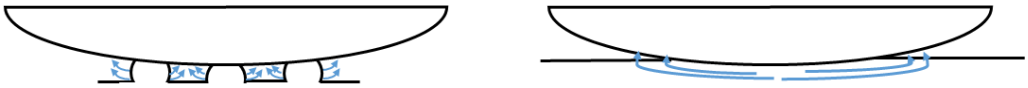

a) b)

Figure 5-10 Comparison of a) stripped sample and b) flat sample. Blue arrows illustrate the water flowing out of the hydrogel. The distance hat water has to be transported for a patterned sample is shorter.

The ability to control friction is of great importance in biomedical applications such as joint implants, where low friction is desired with specific pressures and velocities. In this work, contact visualization was not achieved due to the very close refractive index of hydrogel and water. Therefore, for future studies, contact visualization by adding a fluorescent agent to hydrogels, and using the confocal microscopy is suggested. Contact visualization would help in further understanding of the mechanism by obtaining the real contact area. The influence of sliding speed on the contact size and also the deformation of the patterned hydrogels can be studied more accurately. Further investigations on the influence of pattern shape have to be done to allow more detailed conclusions, notably about potential similar trends as a function of dimension ratio (scale invariance).

6 Surface-attached hydrogels combined with liquid lubricants

Water-based lubricants are not only environmentally friendly but also suitable for biomedical applications such as implants. Researchers achieved superlubricity using phosphatidylcholine liposomes in water. The low friction in such systems has been attributed to a hydration layer that surrounds the charged groups [173,174]. As a result of the attractive forces, water molecules will be more difficult to be squeezed out, so the system can undergo high pressure but still exhibit low friction. Hydrated polymer brushes and amphiphilic surfactants demonstrated similar behavior [66,71]. This lubrication mechanism only applies to charged systems. Additionally, most of these systems were investigated on atomically smooth surfaces, so they are limited in practical applications.

Previous studies have revealed that an absorbed layer of surfactant can reduce friction considerably [175]. The relation between molecular orientation and friction by using specifically structured surfaces has also been investigated. It was found that the effective viscosity decreases as the lubricant molecules become oriented parallel to the shear direction, resulting in friction reduction [126,176]. An induced electric field can also be used as a mechanism to orient the molecules in the same direction as sliding that promotes the frictional properties [177].

Chen *et al*. investigated the frictional behavior of octyl β-D-glucopyranoside (C8) dissolved in water, which is an environmentally friendly substance with an amphiphilic molecular structure. Friction studies were performed using ring plate geometry under oscillating motion using as friction pairs 100Cr6-100Cr6 steel surfaces [126]. They have shown that friction in this system depends on the applied pressure and concentration of C8. They have observed a significant reduction of COF compared to pure water by adding C8. Increasing concentration of the solution from 10 % to 50% gives better lubrication properties caused by the ability of the material to form ordered, i.e., lyotropic, structures. The surfactant C8 is composed of a hydrophilic head group and a hydrophobic alkyl chain and can form an ordered phase under specific concentration, temperature, and pressure conditions [126]. Various structures ranging from micelles, cubic, and lamellar structure can be formed depending on viscosity. The friction in such systems depends strongly on the shear rate. At high shear rates, sliding induce a molecular alignment of the surfactants in the friction gap. This generates an

anisotropic viscosity which allows a high load-carrying capacity and a low viscosity in the shear direction [126]. The thin film lubrication of C8 solution by alignment of structures with the shear direction is shown in Figure 6-1 [126].

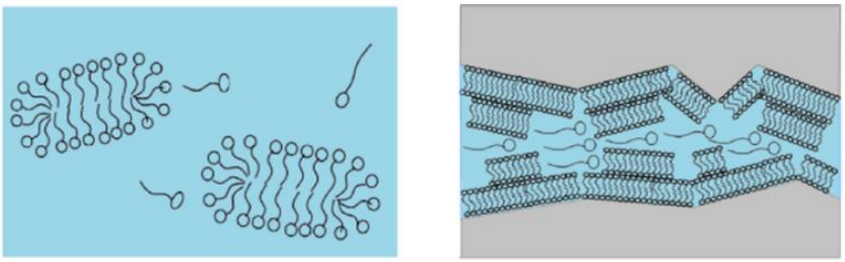

Figure 6-1 Thin film lubrication of C8 presented schematically by the formation of the cylindrical micelles [126].

Since water is the lubricant between hydrogel coated surfaces, modifying water by means of additives might help reduce friction and change the frictional properties. For this purpose, friction tests were performed on a water- swollen sample and the same sample swollen with a 40 % C8 water solution. The thickness of the hydrogel layer in this test is about 65 µm.

The viscosity of the C8 water solution was determined with a rotational rheometer (Anton Paar, Physica MCR 501) with cone-plate geometry (CP: 50-2/TG, diameter: 49.915 mm, angle: 2.001°) at an increasing shear rate of 0.1-1000 s^{-1} at 20 °C. The measured viscosity starts from 80 mPa.s and drops to 29 mPa.s at high shear rates. The C8 solution has shear thinning properties due to the alignment of the structures under shear.

Friction tests were carried out using the nanoscratch setup by changing the sliding speed (0.014 -1.4 mm/s) and normal force ($F_N = 100$ mN and $F_N = 1000$ mN). Friction test results presented in Figure 6-2 show that friction for the sample swollen in pure water decreases slightly by increasing sliding speed and after a minimum occurring at a specific sliding speed, friction starts to rise. This shows the transition from the polymer deformation lubrication regime to the drag controlled regime. When the sample is swollen with the 40% C8, the friction coefficient is remarkably lower. Additionally, it is only weakly dependent on the sliding speed in the studied range. A comparison of penetration depth under the same normal load shows that for sample swollen with C8 the penetration depth is smaller than that when only water is used. By increased viscosity, it is not easy to squeeze out the water/solution completely. The penetration depth for the purely water-swollen gel ranges from 5 to 7 µm, however, for the sample swollen with C8 is between 2 to 5 µm when the normal load is 100 mN. For $F_N =$

1000 mN, penetration depth varies between 16 and 28 µm for the water-swollen sample, whereas penetration depth is in the range of 10-12 µm when the sample is in contact with a C8 solution. Therefore, for the same applied load and sliding speed, friction is much lower with C8. The difference between the friction coefficients even becomes larger as the sliding speed increases. The values for COF at 100 mN for the water swollen sample is between 0.036-0.097, while the range with C8 is 0.024- 0.034. At higher load (1000 mN) the COF varies from 0.027 to 0.079 for the water- swollen sample, where the COF range is extremely smaller (0.006-0.017) for the sample swollen with the C8 solution.

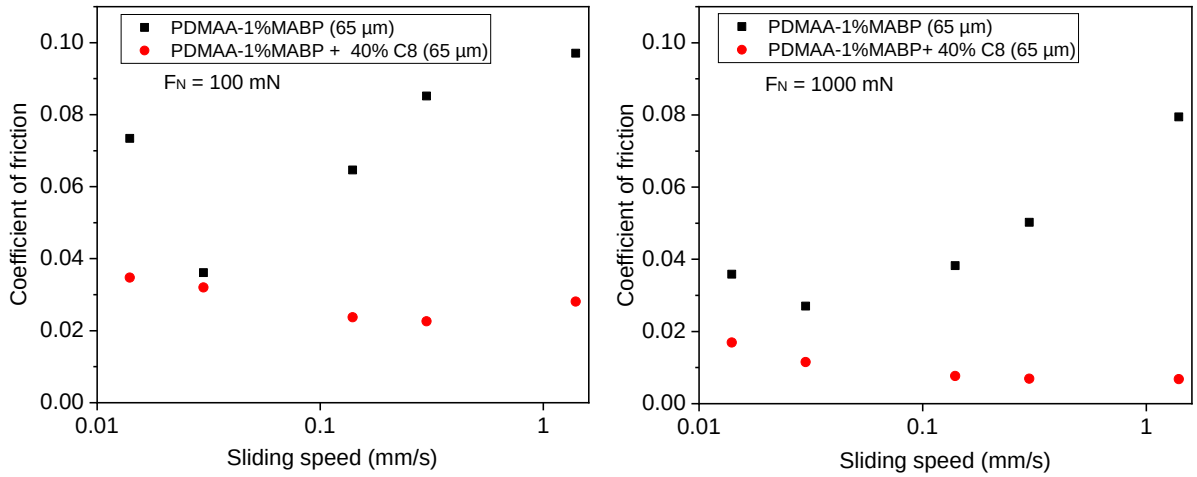

a) b)

Figure 6-2 COF versus sliding speed for water swollen PDMAA- 1% MABP sample with wet thickness of 65 µm and the same sample swollen with 40% C8 solution a) $F_N = 100$ mN and b) $F_N = 1000$ mN.

Furthermore, we performed friction tests by combining the hydrogel friction pairs with a polyvinylpyrrolidone (PVP) solution. PVP is a neutral polymer that can be used to increase the viscosity of water without adding any strong interactions. PVP was dissolved with different concentrations in water and the viscosity of the solutions was measured. According to viscosity measurements, to obtain almost the same viscosity (80 mPa.s at shear rate of 0.1 s^{-1}) as that of the C8 solution, 5.8 % PVP has to be dissolved in water. The results of the friction tests are shown in Figure 6-3. The coefficient of friction is rather similar for the two tests using the C8 and PVP solutions. As can be seen in Figure 6-2 and Figure 6-3, combining hydrogels with PVP or C8 can reduce friction significantly.

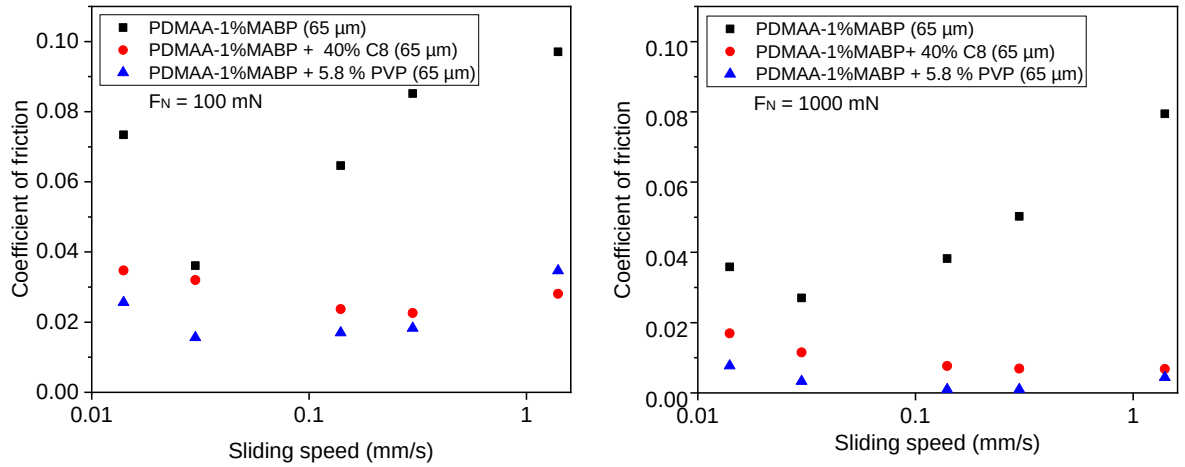

a) b)

Figure 6-3 Friction test results for a sample with 65 µm wet thickness for a water swollen sample, 40% C8 solution and 5.8% PVP solution under two different normal loads a) $F_N =$ 100 mN and b) $F_N = 1000$ mN.

The results show that hydrogels swollen with a C8 or PVP solution can have lower COF than the same hydrogel systems swollen by pure water. In addition, for the C8 or PVP systems, low friction can be maintained in a broader range of sliding speeds. As the viscous solution does not squeeze out of the gel easily, part of the applied load might be supported by the solution inducing a hydrodynamic effect to the system. The solution might even remain in between the opposing sliding surfaces and that avoids direct contact between the two hydrogel layers, which can reduce wear and increase the capability of the system to carry the load. As a result of smaller penetration depth and smaller displaced volume through increased load-bearing capacity, friction is reduced considerably. This validates the previous conclusion on the direct relationship between the friction force and the amount of water that has to be displaced.

Although increasing viscosity to some extent can improve the lubrication, at high sliding velocities, the hydrodynamic lubrication might lead to high friction. In our experiments, the increase in COF by sliding speed is not that significant. Therefore, studying solutions with different viscosities on this system is recommended to find the optimum viscosity. The C8 solution exhibited very promising properties through thin film lubrication [126]. In addition to the high viscosity in comparison to water, anisotropic viscosity of this lubricant at high sliding speeds (shear thinning properties) is expected to improve the lubrication of the surface-attached hydrogel pairs even at higher sliding speeds than measured.

7 Summary and Conclusions

All surfaces in the human body which are frequently in sliding contact with each other are made of soft, permeable tissues. To reduce wear and ensure that they last for a lifetime they evolved to exhibit low friction. The common feature of such interfaces is that they are composed of hydrophilic biopolymers. This has inspired many studies on tribology of tissues, artificial materials, and notably hydrogels. Most of the studies performed so far were conducted using hard sliders and a soft tissue or hydrogel sample as a countersurface, whereas both sides of the contact in the lubricated surfaces in the body are made of soft, permeable surfaces.

It has been proposed that friction of twinned bulk hydrogel samples ("*Gemini*" contact) where the two contacting surfaces are identical is controlled essentially by parameters such as the energy of hydration and the crosslink density (and in case of polyelectrolytes the effective charge density in gel). These parameters govern the polymer network mesh size which in turn determines the permeability and, to some extent, also the stiffness of the hydrogels [104,105,112]. It has been shown that the frictional behavior of "*Gemini*" interfaces changes by varying the sliding speed. The transition in frictional properties is related to the polymer relaxation time and the ratio of the mesh size to the sliding speed [152]. Most of the measurements in the previous studies have been done in a low-pressure range below 100 kPa since the soft hydrogel samples might be damaged under higher pressures.

To ensure the long term stability of the polymeric coatings, it is often desirable to attach the polymers to the surfaces through covalent bonds. Chemically attached polymers are stable even in good solvents and at high ionic strengths, while a physisorbed polymer layer could be dissolved or detached [111].

In this thesis, we investigated the lubrication between the surfaces coated with surface-attached hydrogels. In such a system, interpenetration between the two counter surfaces is prevented due to entropic shielding and size exclusion, which differentiates surface-attached gels from bulk gels. This concept is not unlike that of polymer brushes that have been recently intensely investigated in tribology [73,115,178]. The ultra-low friction between two brush coated surfaces arises from very small interpenetration due to an unfavorable increase in segment-segment repulsions when the polymer brush layers are compressed. Polyelectrolyte brushes, however, are unstable as they are endangered against entropic death [66,71].

Compared to such brushes, the profile density of surface-attached hydrogels decreases sharply within a very small range at the outer periphery of the layer so that the segment density decreases like a delta-function [112]. Thus surface-attached polymer networks exclude chains coming from solution in a much stronger way. Smaller interpenetration, the possibility to create thicker layers and better mechanical stability make surface-attached hydrogels attractive candidates for tribological studies.

Frictional behavior between two hydrogel coated surfaces can basically be described by three main components: forces generated by adhesion, polymer deformation, and drag. Pull-off tests with the AFM and a nano-indenter showed that when two highly hydrated hydrogel coated surfaces were in contact, adhesion was extremely low and it was not recordable with either of the aforementioned techniques. To study the adhesion induced friction, friction tests were carried out in sliding experiments at a very low sliding speed (0.001 mm/s) under a small load (3 mN), where the deformation was mostly zero. These tests with the nanoscratch setup confirmed that adhesion can be considered to have a negligible contribution to friction (COF <0.001). Hence, the main components of the friction force when these layers are strongly compressed are the polymer deformation force and the drag force. The application of a load leads to the squeezing out of the water from the polymer layer and the deformation of the polymer network. The friction force depends on the volume of the water that has to be displaced, which in turn depends on the extent of the water squeeze out. The compressibility of the layers is strongly a function of the thickness of the layer, or in other words, the extent of the layer confinement. Thus, the friction behavior of such hydrogel layers is also highly thickness dependent.

In friction tests, it was observed that the friction force does not depend linearly on the normal load. The deviation from Amanton's law is caused by the limited compressibility of these layers. The limited compressibility leads to a friction force that becomes independent of the applied load at some point, meaning that the COF reduces as the applied load becomes larger. This limited compressibility is the result of several parameters such as nonlinear behavior of polymer chains at high extensions, the incompressible fluid phase in the polymer matrix and the confinement. Furthermore, the compressibility depends strongly on the osmotic pressure in the gel, which in turn depends (for a given chemical composition of the gel) on the crosslink density and the degree of charging of the polymers. By increased osmotic pressure

through charged polymers, the load-bearing capacity of hydrogels is expected to increase. The influence of the charges on the lubrication properties of hydrogels remains to be seen.

The attachment of hydrogels to a stiff substrate not only reduces adhesion between the contact counterparts but also decreases the swelling/increases the segment concentration in the film leading to smaller penetration depth. As the zone, in which complete relaxation can occur, becomes larger than the thickness of the hydrogel layer (strong confinement), the hydrogel layer cannot relax completely. Incomplete relaxation of the sample and high segment density results in a higher effective modulus of the gel layer, a smaller penetration depth and a lower coefficient of friction.

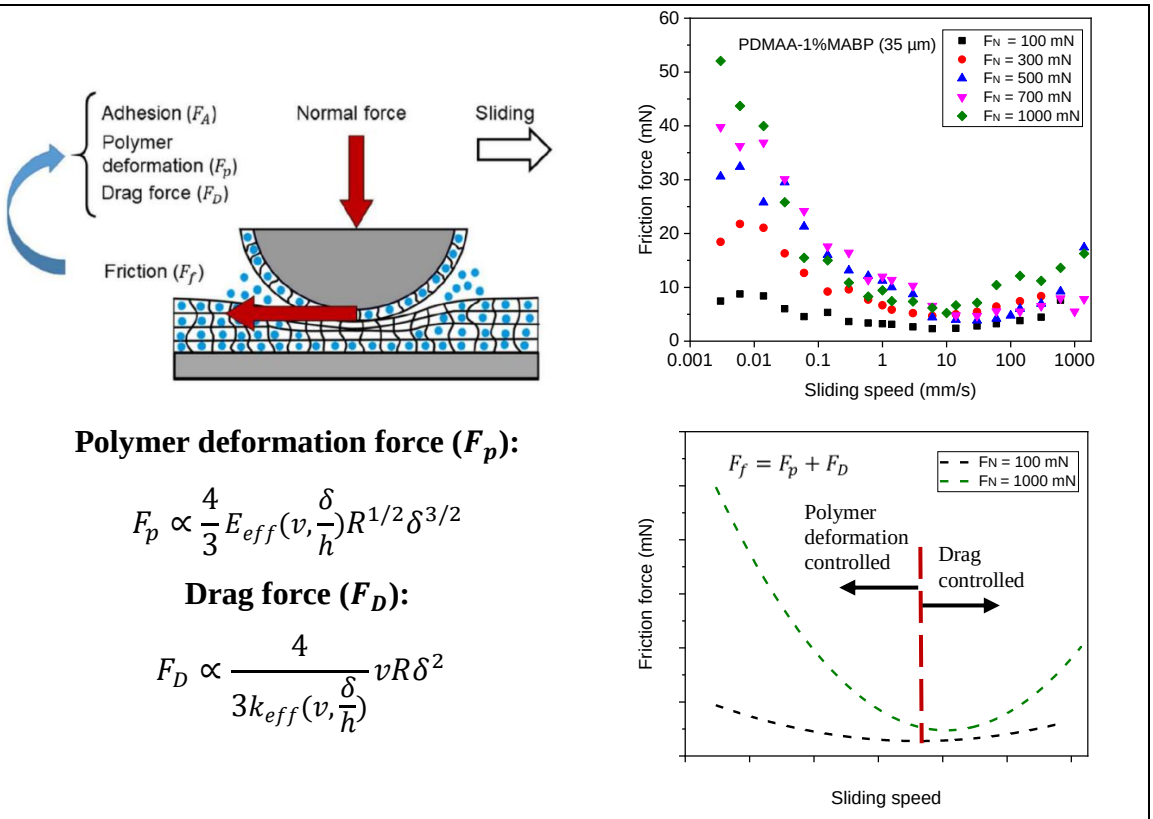

Figure 7-1 Summary of the lubrication mechanism of surface-attached hydrogels considering the forces contributing to the friction force.

Friction tests showed that lubrication of surface-attached hydrogels depends on two parameters: the extent of penetration of the slider into the gel and the drag force induced by the movement of water. The penetration depth decreases with increasing sliding velocity, while the

drag increases – leading in many cases to a minimum in the friction coefficient at intermediate velocities. How pronounced this behavior depends on the degree of confinement, i.e., the layer thickness. Thus the frictional behavior of such hydrogels can be described in two regimes, namely a polymer deformation controlled regime and a drag force controlled regime. Polymer deformation governs the lubrication when the sliding velocity is low. Drag control occurs when most of the fluid is still in the network and does not have enough time to be displaced.

All friction force curves can be superimposed onto each to form a master curve by normalizing the data by a force characteristic number. The force characteristic number is defined as a dimensionless number that is proportional to the sliding speed and the contact radius and it is inversely proportional to the permeability and elastic modulus. In some publications, it is considered as similar to a Peclet number. It has to be pointed out that for the surface-attached gels, as confinement plays an important role in the determination of the contact stiffness and permeability, effective elastic modulus and effective permeability have to be taken into account. The film thickness plays a role when the layers are confined and no complete stress relaxation can occur. High confinement of the polymer (sub)chains in the gel results in a lower penetration (and thus a slightly smaller contact area) and a higher effective modulus, thus leads to a smaller force characteristic number.

When channels are introduced, the system consists of the swollen hydrogel and bulk water inside of the channel. The water squeezed out from the gel can now flow easily through the channels as the viscosity of bulk water is much lower than that of water in a hydrogel. This decreases the water resistance against sliding, especially when the sliding is in the same direction as the channels. The lower friction of the textured hydrogels comparing to the flat layers is due to the fact that the distance through which water has to be transported to be squeezed out is much shorter in the case of the patterned hydrogels. However, decreasing the structure width of patterned hydrogels does not always lead to smaller friction comparing to the ones with wider structures, as narrow and high stripes are more susceptible to large deformation under the same applied load. Thus, the friction force of textured hydrogels depends not only on in the presence of channels but also on the ability of the structures to support the load.

A significant improvement of the friction properties was noticed by combining the hydrogel-hydrogel system with liquid lubricants. Similar behavior was observed when a low molecular weight alkylgluconat or the polymer polyvinylpyrrolidon was used. In both cases, extremely low friction in a broad range of sliding speeds was obtained, indeed so low that the COF could not be measured which means that the COF is lower than 0.001. The penetration

depth of the slider into the gel was smaller with both PVP and C8 in comparison to the purely water-swollen sample. This implies that a part of the applied load is supported by the fluid phase and induces hydrodynamic lubrication

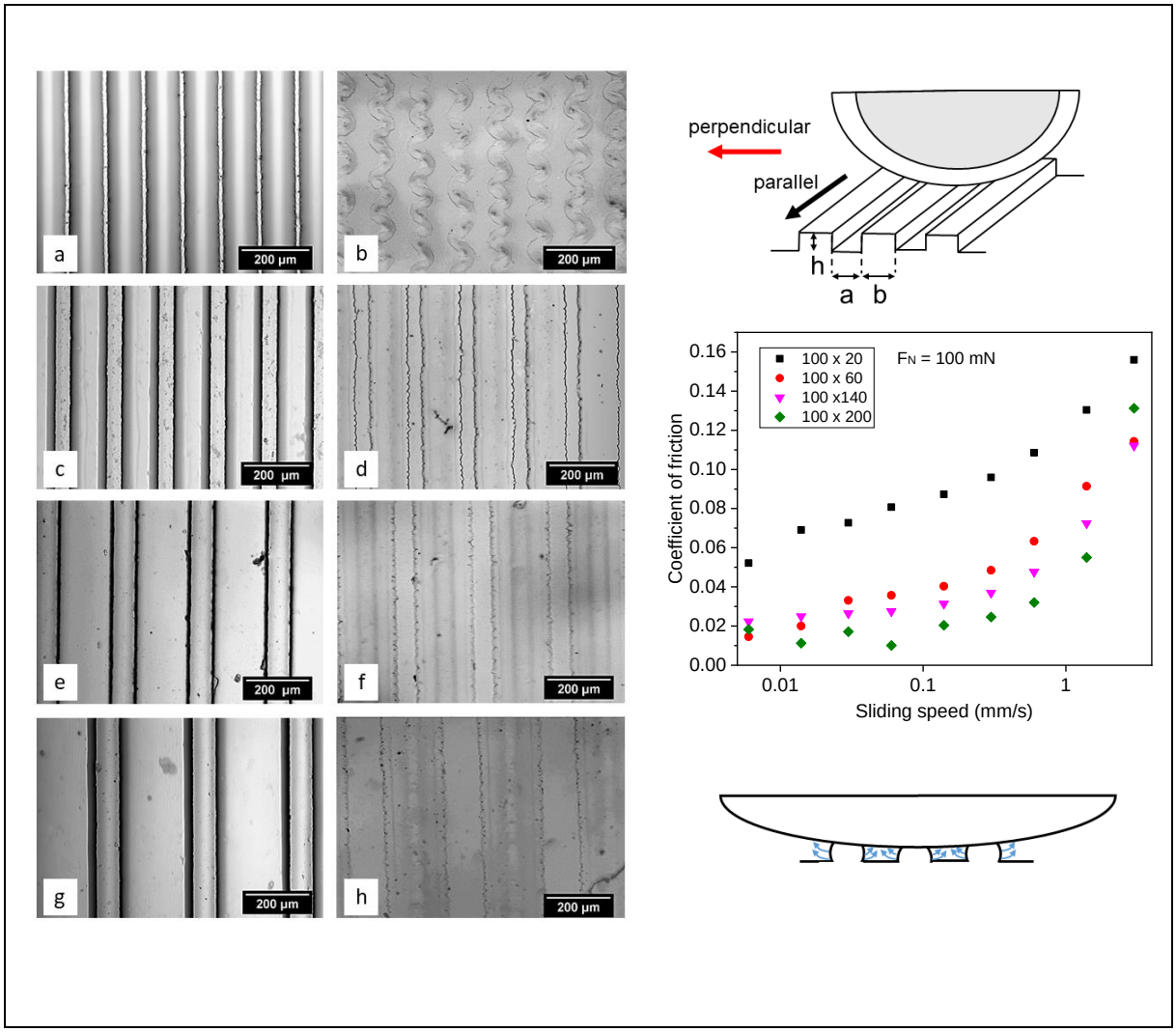

Figure 7-2 Overview on the key findings of the effect of surface patterns on lubrication of surface-attached hydrogels.

Friction systems in which both sides are coated with a hydrogel and are swollen in water are extremely interesting lubricant systems, at least in a pressure range which is roughly the same as that occurring in human joints. The hydrogel-hydrogel systems show extremely low coefficients of friction, which can be even lowered through microstructuring or through the addition of polymeric viscosity enhancers. The COF were among the lowest reported for macroscopic systems so far and even in some cases below the detection limit of the measurement setup (COF < 0.001). The results for textured surface-attached hydrogels and the additivated systems are very attractive and make further investigations in this direction promising.

8 Zusammenfassung und Schlussfolgerungen

Alle Oberflächen im menschlichen Körper, die häufig in Gleitkontakt miteinander stehen, bestehen aus weichem, durchlässigem Gewebe. Um den Verschleiß zu reduzieren und ihre Lebensdauer zu gewährleisten, sind sie so konzipiert, dass sie eine geringe Reibung aufweisen. Die gemeinsame Eigenschaft solcher Grenzflächen ist, dass sie aus hydrophilen Biopolymeren bestehen. Dies hat viele Studien zur Tribologie von Geweben, künstlichen Materialien und Hydrogelen inspiriert. Die meisten der bisher durchgeführten Studien wurden mit harten Gleitern und einer weichen Gewebe- oder Hydrogelprobe als Gegenfläche durchgeführt, wobei beide Seiten des Kontakts in den geschmierten Oberflächen im Körper aus weichen, durchlässigen Oberflächen bestehen.

Es wurde vorgeschlagen, dass die Reibung von verzwillingten Hydrogel-Massenproben ("Zwillings"-Kontakt), bei denen die beiden Kontaktflächen identisch sind, im Wesentlichen durch Parameter wie die Hydratationsenergie und die Vernetzungsdichte (und im Falle von Polyelektrolyten die effektive Ladungsdichte im Gel) gesteuert wird. Diese Parameter bestimmen die Maschenweite des Polymernetzwerks, die wiederum die Permeabilität und teilweise auch die Steifigkeit der Hydrogele bestimmt [102,103,110]. Es hat sich gezeigt, dass sich das Reibungsverhalten von "Gemini"-Grenzflächen durch Variation der Gleitgeschwindigkeit ändert. Der Übergang in den Reibungseigenschaften hängt von der Relaxationszeit des Polymers und dem Verhältnis der Maschengröße zur Gleitgeschwindigkeit ab [148]. Die meisten Messungen in den vorherigen Studien wurden in einem Niederdruckbereich unter 100 kPa durchgeführt, da die weichen Hydrogelproben unter höheren Drücken beschädigt werden könnten.

Um die Langzeitstabilität der Polymerbeschichtungen zu gewährleisten, ist es oft wünschenswert, Polymere chemisch an Oberflächen zu befestigen. Chemisch gebundene Polymere sind auch in guten Lösungsmitteln und bei hohen Ionenstärken stabil, während eine physikalisch gebundene Polymerschicht aufgelöst oder abgelöst werden könnte [109].

In diesem Projekt haben wir die Schmierung zwischen den mit oberflächengebundenen Hydrogelen beschichteten Oberflächen untersucht. In einem solchen System wird die gegenseitige Durchdringung zwischen den beiden Gegenflächen durch entropische Abschirmung und Größenausschluss verhindert, was oberflächengebundene Gele von Bulk-Gelen unterscheidet. Dieses Konzept ist dem Konzept von Polymerbürsten nicht unähnlich, das

in letzter Zeit intensiv in der Tribologie untersucht wurde [73,113,173]. Die ultra-niedrige Reibung zwischen zwei bürstenbeschichteten Oberflächen entsteht durch eine sehr geringe gegenseitige Durchdringung aufgrund einer ungünstigen Zunahme der Segment-Segment-Abstoßungen, wenn die Polymer-Bürstenschichten komprimiert werden. Eine starke gegenseitige Durchdringung tritt jedoch schließlich bei hohem Druck auf und führt zu einer signifikanten Erhöhung der Reibung. Polyelektrolytbürsten sind jedoch instabil, da sie gegen den entropischen Tod gefährdet sind [66,71]. Die Hauptprobleme bei der Anwendung von Bürsten als Schmiermittel sind ihre Stabilität bei hohen Drücken und ihre geringe Dicke.

Vergleicht man die oberflächengebundenen Hydrogel-Netzwerke mit den Bürsten, so bleibt die Profildichte der oberflächengebundenen Hydrogele konstant, und sie nimmt nur an den wenigen Nanometern der Oberfläche ab [110]. Kleinere Interpenetration, die Möglichkeit, dickere Schichten zu erzeugen, und eine bessere mechanische Stabilität machen oberflächengebundene Hydrogele zu faszinierenden Kandidaten für tribologische Untersuchungen.

Das Reibungsverhalten zwischen zwei mit Hydrogel beschichteten Oberflächen lässt sich grundsätzlich durch die zur Reibungskraft beitragenden Kräfte beschreiben. Die Reibungskraft hat drei Hauptkomponenten: Kräfte, die durch Adhäsion erzeugt werden, Polymerverformung und Widerstand. Abzugsversuche mit dem Rasterkraftmikroskop und dem Nanoindenter zeigten, dass die Adhäsion, wenn zwei stark hydratisierte Hydrogel beschichtete Oberflächen in Kontakt waren, extrem gering war und mit keiner der beiden oben genannten Techniken gemessen werden konnte. Zur Untersuchung der adhäsionsinduzierten Reibung wurden Reibungstests bei einer sehr niedrigen Gleitgeschwindigkeit (0,001 mm/s) unter einer niedrigen Last (3 mN) durchgeführt, wobei die Verformung größtenteils Null war. Diese Tests mit dem Nanoscratch-Setup bestätigten, dass die Adhäsion einen vernachlässigbaren Beitrag zur Reibung hat (COF < 0,001). Daher sind die Hauptkomponenten der Reibungskraft –wenn diese Schichten stark komprimiert werden– die Polymerverformungskraft und die Widerstandskraft. Die aufgebrachte Belastung führt zum Herausdrücken des Wassers aus der Polymerschicht und zur Verformung des Polymernetzwerks. Die Reibungskraft hängt von dem Volumen des zu verdrängenden Wassers ab, das wiederum vom Ausmaß des Wasserausdrucks abhängt. Die Kompressibilität der Schichten ist stark abhängig von der Schichtdicke, oder anders gesagt, vom Ausmaß des Schichteinschlusses. Daher ist auch das Reibungsverhalten solcher Hydrogelschichten stark dickenabhängig.

In unseren Reibungsversuchen wurde beobachtet, dass die Reibungskraft nicht linear von der Normalkraft abhängt. Die Abweichung vom Amanton'schen Gesetz wird durch die begrenzte Kompressibilität dieser Schichten verursacht. Die begrenzte Kompressibilität führt zu einer Reibungskraft, die irgendwann unabhängig von der aufgebrachten Belastung wird, was bedeutet, dass die COF mit zunehmender Belastung abnimmt. Diese begrenzte Kompressibilität ist das Ergebnis mehrerer Parameter, wie z.B. des nichtlinearen Verhaltens von Polymerketten bei hohen Dehnungen, der inkompressiblen flüssigen Phase in der Polymermatrix und des Einschlusses. Darüber hinaus hängt die Kompressibilität stark vom osmotischen Druck im Gel ab, der wiederum (bei einer gegebenen chemischen Zusammensetzung des Gels) von der Vernetzungsdichte und dem Ladungsgrad der Polymere abhängt. Durch einen erhöhten osmotischen Druck durch geladene Polymere soll die Belastbarkeit von Hydrogelen erhöht werden. Der Einfluss der Ladungen auf die Schmiereigenschaften von Hydrogelen bleibt abzuwarten.

Die Anbringung von Hydrogelen auf einem steifen Substrat reduziert nicht nur die Haftung zwischen den Kontaktgegenstücken, sondern verringert auch die Quellung bzw. erhöht die Segmentkonzentration im Film, was zu einer geringeren Eindringtiefe führt. Da die Zone, in der eine vollständige Relaxation auftreten kann, größer als die Dicke der Hydrogelschicht wird (starker Einschluss), kann sich die Hydrogelschicht nicht vollständig entspannen. Eine unvollständige Relaxation der Probe und eine hohe Segmentdichte führen zu einem höheren effektiven Elastizitätsmodul der Gelschicht, einer geringeren Eindringtiefe und einem niedrigeren Reibungskoeffizienten.

Reibungstests zeigten, dass die Schmierung von oberflächengebundenen Hydrogelen von zwei Parametern abhängt: dem Ausmaß des Eindringens des Gleiters in das Gel und der durch die Bewegung des Wassers induzierten Zugkraft. Die Eindringtiefe nimmt mit zunehmender Gleitgeschwindigkeit ab, während der Widerstand zunimmt - was in vielen Fällen zu einem Minimum des Reibungskoeffizienten bei mittleren Geschwindigkeiten führt. Wie stark dieses Verhalten ausgeprägt ist, hängt vom Grad des Einschlusses, d.h. der Schichtdicke, ab. Daher kann das Reibungsverhalten solcher Hydrogele in zwei Systeme/Bereiche beschrieben werden, nämlich in einem polymerverformungskontrollierten System/Bereich und einem widerstandskraftkontrollierten System/Bereich. Die Polymerverformung steuert die Schmierung, wenn die Gleitgeschwindigkeit gering ist. Der schleppkraftgesteuerte Bereich tritt

auf, wenn sich der größte Teil der Flüssigkeit noch im Netzwerk befindet und nicht genügend Zeit hat, um verdrängt zu werden.

Alle Kraftkurven können durch Normalisierung der Daten mit einer Kraftkennlinie zu einer Hauptkurve überlagert werden. Die Kraftkennlinie ist als eine dimensionslose Zahl definiert, die proportional zur Gleitgeschwindigkeit und zum Kontaktradius ist und umgekehrt proportional zur Permeabilität und zum Elastizitätsmodul ist. In einigen Veröffentlichungen wird sie als ähnlich wie eine Peclet-Zahl betrachtet. Es muss darauf hingewiesen werden, dass für die oberflächengebundenen Gele, da der Einschluss eine wichtige Rolle bei der Bestimmung der Kontaktsteifigkeit und Permeabilität spielt, der effektive Elastizitätsmodul und die effektive Permeabilität berücksichtigt werden müssen. Auch Ergebnisse für unterschiedliche Schichtdicken können berücksichtigt werden. Ein hoher Einschluss der Polymer(unter)ketten im Gel führt zu einer geringeren Penetration (und damit zu einer etwas kleineren Kontaktfläche) und einem höheren effektiven Elastizitätsmodul, führt also zu einer geringeren Kraftkennlinie.

Die Einführung von Kanälen an der Oberfläche von Hydrogelen erhöht die Wahrscheinlichkeit des Wassereinschlusses zwischen den Kanälen. Darüber hinaus kann das ausgedrückte Wasser leicht durch die Kanäle fließen, da die Viskosität von Schüttwasser viel niedriger ist als die von Wasser in einem Hydrogel. Dies verringert den Wasserwiderstand gegen das Gleiten, insbesondere wenn das Gleiten in der gleichen Richtung wie die Kanäle erfolgt. Die geringere Reibung der texturierten Hydrogele im Vergleich zu den flachen Schichten ist darauf zurückzuführen, dass die Strecke, über die Wasser transportiert werden muss, um ausgepresst zu werden, bei den strukturierten Hydrogelen viel kürzer ist. Die Verringerung der Strukturbreite von strukturierten Hydrogelen führt nicht immer zu einer geringeren Reibung im Vergleich zu denjenigen mit breiteren Strukturen, da die schmalen Streifen unter der gleichen angewandten Belastung anfälliger für große Verformungen sind. Daher wird die Reibungskraft von strukturierten Hydrogelen in Gegenwart von Kanälen hauptsächlich durch die Fähigkeit der Strukturen, die Last zu tragen, bestimmt.

Eine signifikante Verbesserung der Reibungseigenschaften wurde durch die Kombination des Hydrogel-Hydrogel-Systems mit flüssigen Schmiermitteln festgestellt. Ein ähnliches Verhalten wurde beobachtet, wenn ein niedermolekulares Alkylgluconat (C8) oder das Polymer Polyvinylpyrrolidon (PVP) verwendet wurde. In beiden Fällen wurde eine extrem niedrige Reibung in einem breiten Bereich von Gleitgeschwindigkeiten erzielt, und zwar so niedrig, dass der Reibungskoeffizient nicht gemessen werden konnte (COF< 0,001). Die

Eindringtiefe war sowohl bei PVP als auch bei C8 im Vergleich zur rein wassergequollenen Probe geringer. Dies impliziert, dass ein Teil der aufgebrachten Last von der flüssigen Phase getragen wird und eine hydrodynamische Schmierung induziert.

Reibungssysteme, bei denen beide Seiten mit einem Hydrogel beschichtet und in Wasser gequollen sind, sind äußerst interessante Schmiersysteme, zumindest in einem Lastbereich, der in etwa dem der menschlichen Gelenke entspricht. Die Hydrogel-Hydrogelsysteme weisen extrem niedrige Reibungskoeffizienten auf, die durch Mikrostrukturierung oder durch Zugabe von polymeren Viskositätsverbesserern noch gesenkt werden können. Die Reibungskoeffizienten gehörten zu den niedrigsten, die bisher für makroskopische Systeme berichtet wurden, und lagen in einigen Fällen sogar unter der Nachweisgrenze des Messaufbaus (COF < 0,001). Die Ergebnisse für texturierte, oberflächengebundene Hydrogele und die additivierten Systeme sind sehr attraktiv und weitere Untersuchungen in dieser Richtung sind ebenfalls vielversprechend.

9 Résumé et conclusions

Les surfaces du corps humain qui sont en contact glissant les unes par rapport aux autres sont constituées de matière molle et perméable. Afin de réduire leur usure et garantir leur longévité, l'évolution a conféré à ces couples de tissus un faible coefficient de frottement. La caractéristique commune des interfaces concernées est qu'elles sont composées de bio-polymères hydrophiles. Cela a inspiré de nombreuses études sur la tribologie des tissus, des matériaux artificiels, et notamment des hydrogels. La plupart des études réalisées jusqu'à présent ont été menées en mettant en œuvre des frotteurs rigides contre des échantillons de tissu mou ou d'hydrogel, contrairement aux cas rencontrés dans la Nature où les deux surfaces en contact sont molles et perméables.

Il a été proposé que le frottement entre des hydrogels massifs (contact "Gemini") où les deux surfaces en contact sont identiques soit contrôlé essentiellement par des paramètres tels que l'énergie d'hydratation et la densité de réticulation (et dans le cas des poly-électrolytes, la densité de charge effective dans le gel). Ces paramètres régissent la taille caractéristique (*mesh size*) du réseau de polymère qui, à son tour, détermine la perméabilité et, dans une certaine mesure, la rigidité des hydrogels [104,105,112]. Il a été démontré que le comportement au frottement des interfaces "Gemini" dépend du temps de relaxation du polymère ainsi que du rapport entre la taille caractéristique du réseau polymérique et la vitesse de glissement [152]. La plupart des mesures dans les études précédentes ont été effectuées dans une plage de faible pression, inférieure à 100 kPa, car les échantillons d'hydrogel peuvent être endommagés sous des pressions plus élevées.

Pour assurer la stabilité à long terme des revêtements polymères, il est souvent souhaitable de fixer les polymères aux surfaces par des liaisons covalentes. Les polymères fixés chimiquement sont stables même dans de bons solvants à forces ioniques élevées, tandis qu'une couche de polymère physisorbé pourrait être dissoute ou détachée [111].

Dans cette thèse, nous avons étudié la lubrification entre les surfaces revêtues d'hydrogels fixés en surface. Dans un tel système et contrairement aux hydrogels massifs, l'interpénétration entre les deux surfaces antagonistes est empêchée par un effet bouclier entropique et l'exclusion de taille. Ce concept n'est pas différent de celui concernant les brosses de polymères qui ont été récemment intensément étudiées en tribologie [73,115,178]. Le frottement ultra-faible entre deux surfaces recouvertes de brosses résulte d'une très faible

interpénétration des macromolécules du fait de leurs répulsions croissantes à force qu'on les comprime. Les brosses en polyélectrolyte sont cependant instables car menacées de mort entropique [66,71].

Par rapport à ces brosses, la densité du profil des hydrogels fixés en surface diminue fortement proche de la périphérie extérieure de la couche, de sorte que la densité des chaines diminue comme une fonction delta [112]. Ainsi, ces réseaux de polymères fixés en surface excluent beaucoup plus fortement les chaînes présents dans la solution. Une interpénétration plus faible, la possibilité de créer des couches plus épaisses et une meilleure stabilité mécanique font des hydrogels fixés en surface des candidats intéressants pour les études tribologiques.

Le comportement au frottement de deux surfaces revêtues d'hydrogel peut être décrit essentiellement par trois composantes principales : les forces générées par l'adhésion, la déformation du polymère et la traînée engendrée par le déplacement du fluide. Des tests de décollement avec un AFM et un nano-indenteur ont montré que lorsque deux surfaces revêtues d'hydrogel hautement hydraté étaient en contact, l'adhésion était extrêmement faible et qu'elle n'était pas mesurable avec l'une ou l'autre des techniques susmentionnées. Pour étudier le frottement induit par l'adhésion, des essais de frottement ont été réalisés dans des expériences de glissement à une très faible vitesse (0,001 mm/s) sous une charge minimale (3 mN) pour laquelle la déformation était pratiquement nulle. Ces tests réalisés sur le dispositif de nano-rayure ont confirmé que l'adhésion peut être considérée comme ayant une contribution négligeable au frottement (COF < 0,001). Ainsi, les principales contributions au frottement dans ces systèmes en contact sont la force de déformation du polymère et la force de traînée. L'application d'un chargement entraîne la déformation du réseau polymère ainsi que l'expulsion de l'eau de celui-ci. La force de frottement dépend du volume d'eau déplacé, qui dépend lui-même de l'ampleur de l'expulsion de l'eau. La compressibilité des couches est fortement fonction de l'épaisseur de la couche, ou en d'autres termes, du confinement de la couche. Ainsi, le comportement au frottement de ces hydrogels dépend aussi fortement de l'épaisseur. Lors des essais de frottement, il a été observé que la force de frottement ne dépend pas linéairement de la charge normale. L'écart par rapport à la loi d'Amanton est dû à la compressibilité limitée de ces couches qui entraîne dans certaines conditions une diminution du COF à mesure que la charge appliquée augmente.

Cette compressibilité limitée est le résultat de plusieurs paramètres tels que le comportement non linéaire des chaînes polymères lors de larges extensions, la phase fluide incompressible dans la matrice polymère et le confinement. En outre, la compressibilité dépend fortement de la pression osmotique dans le gel, qui à son tour dépend (pour une composition chimique donnée du gel) de la densité de réticulation et du degré de charge des polymères. En augmentant la pression osmotique par le biais des polymères chargés, la capacité de charge des hydrogels devrait augmenter. L'influence des charges sur les propriétés de lubrification des hydrogels reste à explorer.

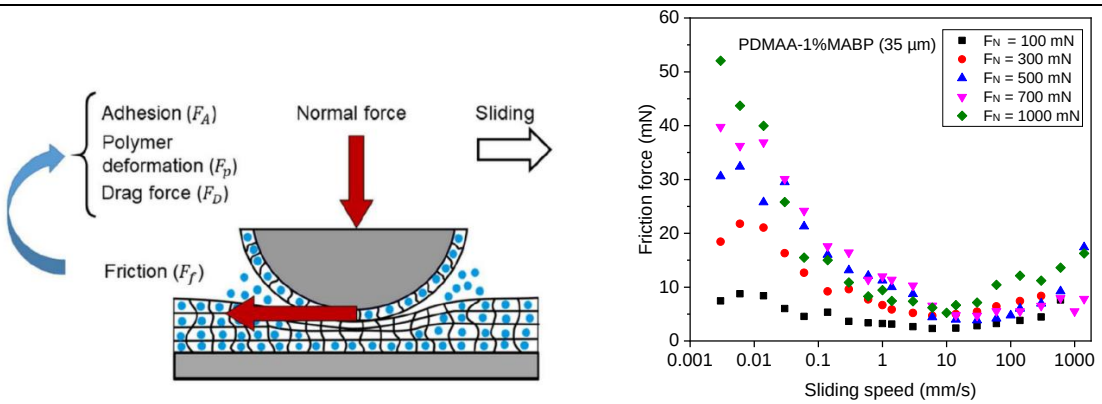

Polymer deformation force (F_p):

$$F_p \propto \frac{4}{3} E_{eff}(v, \frac{\delta}{h}) R^{1/2} \delta^{3/2}$$

Drag force (F_D):

$$F_D \propto \frac{4}{3 k_{eff}(v, \frac{\delta}{h})} vR\delta^2$$

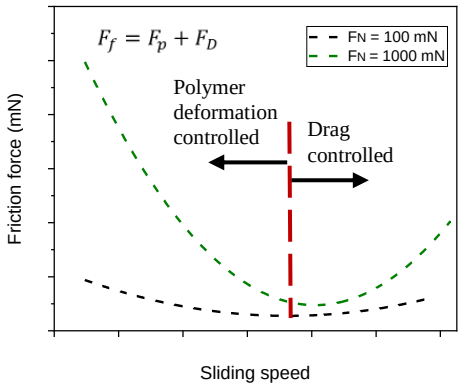

Force characteristic number:

$$\frac{F_D}{F_p} \propto Pe = \frac{va}{k_{eff}(v, \frac{\delta}{h}) E_{eff}(v, \frac{\delta}{h})}$$

Figure 9-1 Résumé du mécanisme de lubrification des hydrogels fixés en surface et description des différentes forces qui contribuent à la force de frottement.

L'accroche des hydrogels à un substrat rigide non seulement réduit l'adhésion entre les surfaces en contact mais aussi diminue le gonflement/augmente la concentration de chaines dans le film, ce qui entraîne une profondeur de pénétration plus faible. Comme la zone nécessaire à une relaxation complète devient plus grande que l'épaisseur de la couche d'hydrogel

(fort confinement), la couche d'hydrogel ne peut pas se relaxer complètement. La relaxation incomplète de l'échantillon et la densité élevée des chaines se traduisent par un module effectif plus élevé, une profondeur de pénétration plus faible et un coefficient de frottement plus faible.

Des tests de frottement ont montré que la lubrification des hydrogels fixés en surface dépend de deux paramètres : le niveau de pénétration du frotteur dans le gel et la force de traînée induite par le mouvement de l'eau. La profondeur de pénétration diminue avec l'augmentation de la vitesse de glissement, tandis que la traînée augmente - ce qui conduit dans de nombreux cas à un coefficient de frottement minimum à des vitesses intermédiaires. L'importance de ce comportement dépend du degré de confinement, c'est-à-dire de l'épaisseur de la couche. Ainsi, le comportement de frottement de ces hydrogels peut être décrit dans deux régimes, à savoir un régime contrôlé par la déformation du polymère et un régime contrôlé par la force de traînée. La déformation des polymères régit la lubrification lorsque la vitesse de glissement est faible. Le régime gouverné par la traînée se produit lorsque la plus grande partie du fluide est encore dans le réseau et n'a pas le temps d'être déplacée.

Toutes les courbes de force de frottement peuvent être superposées pour former une courbe maîtresse en normalisant les données par une quantité caractéristique. Cette quantité caractéristique est définie comme un nombre sans dimension qui est proportionnel à la vitesse de glissement et au rayon de contact et il est inversement proportionnel à la perméabilité et au module d'élasticité. Dans certaines publications, il est considéré comme similaire à un nombre de Peclet. Il faut souligner que pour les gels fixés en surface, comme le confinement joue un rôle important dans la détermination de la rigidité de contact et de la perméabilité, le module d'élasticité effectif et la perméabilité effective doivent être pris en compte. L'épaisseur du film joue un rôle lorsque les couches sont confinées et qu'aucune relaxation complète des contraintes ne peut se produire. Un confinement élevé des (sous-)chaînes polymères dans le gel entraîne une pénétration plus faible (et donc une surface de contact légèrement plus petite) et un module effectif plus élevé, ce qui conduit à une quantité caractéristique plus faible.

Lorsque des canaux sont ajoutés en surface, le système se compose d’hydrogel gonflé et de l'eau est disponible à l'intérieur de ces canaux. L'eau extraite du gel peut alors s'écouler librement à travers les canaux car sa viscosité est beaucoup plus faible que celle apparente de l'eau contenue dans l'hydrogel. Cela diminue la résistance de l'eau au glissement, en particulier lorsque le glissement se fait dans le même sens que les canaux. Le frottement plus faible des hydrogels texturés par rapport aux couches continues est due au fait que la distance à parcourir

pour faire sortir l'eau est beaucoup plus courte dans le cas des hydrogels à motifs. Toutefois, la diminution de la largeur de la structure des hydrogels à motifs n'entraîne pas toujours un frottement plus faible que celle des hydrogels à structures plus larges, car les bandes étroites et hautes sont plus susceptibles de subir une grande déformation sous une même charge appliquée. Ainsi, la force de frottement des hydrogels texturés ne dépend pas seulement de la présence de canaux, mais aussi de la capacité des structures à supporter le chargement.

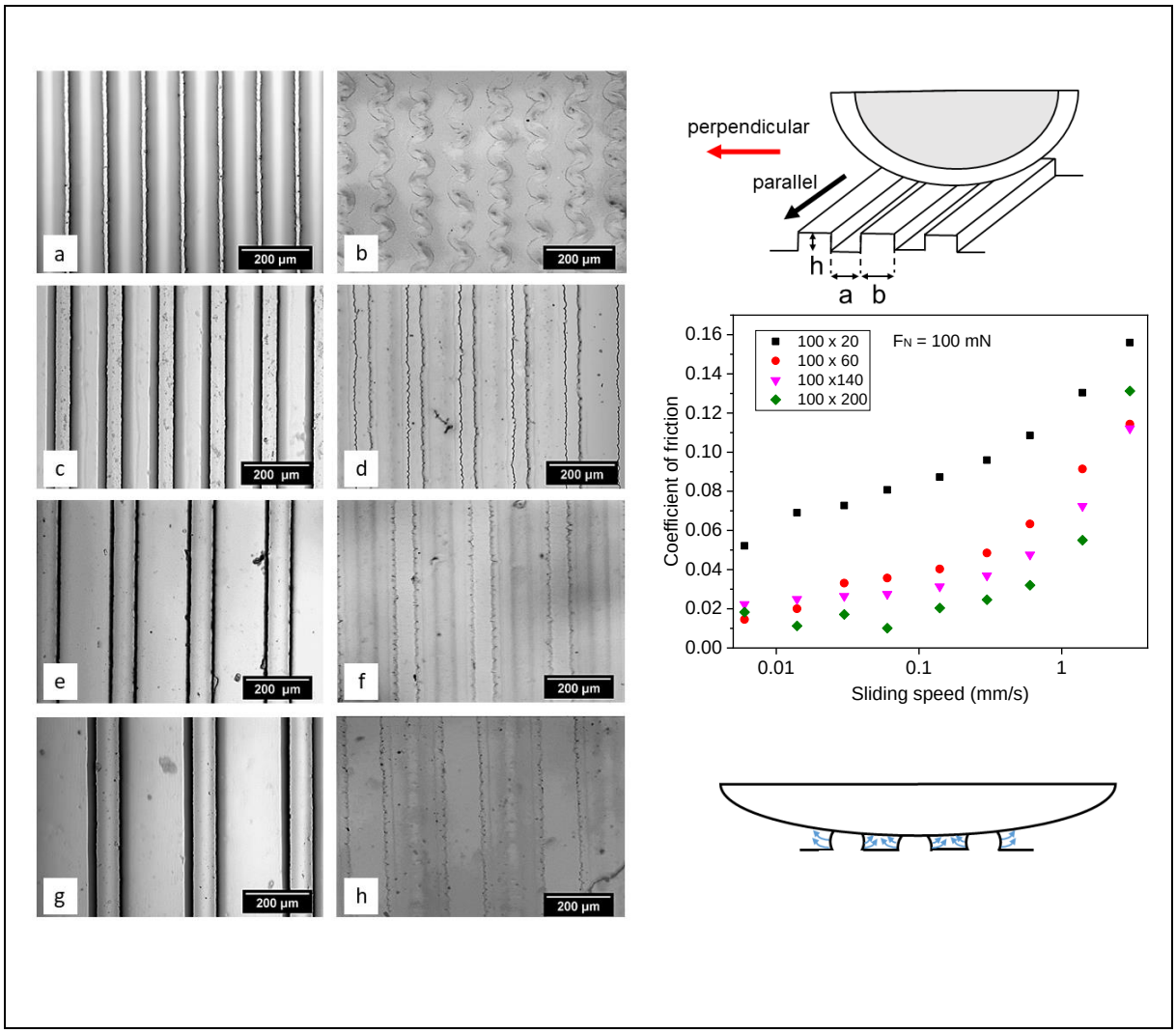

Figure 9-2 Aperçu des principales conclusions associées à l'effet des texturations sur la lubrification des hydrogels fixés en surface.

Une amélioration significative des propriétés de frottement a été constatée en combinant le système hydrogel-hydrogel avec des lubrifiants liquides. Un comportement similaire a été observé lorsqu'un alkylgluconate de faible poids moléculaire ou le polymère polyvinylpyrrolidon a été utilisé. Dans les deux cas, un frottement extrêmement faible dans une large gamme de vitesses de glissement a été obtenue, en fait si faible que le COF n'a pas pu être mesuré, ce qui signifie que le COF est inférieur à 0,001. La profondeur de pénétration du

frotteur dans le gel était plus faible avec le PVP et le C8 par rapport à l'échantillon purement gonflé à l'eau. Cela implique qu'une partie de la charge appliquée est supportée par la phase fluide et induit une lubrification hydrodynamique.

Les systèmes frottants dont les deux surfaces sont revêtues d'un hydrogel et gonflées à l'eau sont des systèmes de lubrification extrêmement intéressants, du moins dans une plage de pression qui est à peu près la même que celle en jeu dans les articulations humaines. Les systèmes hydrogel-hydrogel présentent des coefficients de frottement extrêmement faibles, qui peuvent être encore abaissés grâce à la microstructuration de surface ou à l'ajout de fluidifiants polymériques. Les COF étaient parmi les plus faibles reportés jusqu'à présent pour les systèmes macroscopiques et même dans certains cas, inférieurs à la limite de détection du dispositif de mesure (COF < 0,001). Les résultats obtenus pour les hydrogels texturés fixés en surface et les systèmes additivés sont très prometteurs pour de futures études.

10 Experimental details

10.1 Chemicals

Substances	Provider
Acetone >99.8%	Roth
Acrylamide, >98%	Fluka
Allylbromide, 98%	Sigma Aldrich
Azobis(isobutyronitrile) (AIBN), ≥98%	Sigma Aldrich
Chloroform, p.a.	Roth
Dichloromethane, p.a.	Roth
Diethylether, p.a.	Roth
Dimethylformamide, ≥99.9%	Roth
Ethanol, ≥99.8%	Roth
Hydrochloric acid	Fluka
4-Hydroxybenzophenone	Fluka
methacryloylchloride 97 %	Fluka
Methanol, p.a.	Roth
N, N-dimethylacrylamide, 98%	Roth
n-Hexane(p.a)	Roth
Octyl β-D-glucopyranoside	Sigma Aldrich
Potassium carbonate, ≥ 99%	Roth
2-Propanol (p.a)	Roth
Sodium bicarbonate, > 99.0%	Fluka
Sodium sulfate	Merck
Tetrahydrofuran (THF)	Sigma Aldrich
Toluene, p.a.	Roth
Triethylamine	Roth
Triethoxysilane	Fluka
Water, DI	Millipore

10.2 Other materials

Material	Manufacturer
AFM ACL-W tip	APPNano
AFM tips with spherical bead	NanoandMore
Foil masks (25000 dpi)	Koenen GmbH
Glass lens plano-convex N-K7 KPX025	Edmund optics
Glass slide	Duran
High pressure stainless steel syringe	Cetoni GmbH
PDMS SYLGARD® 184	DOW Corning
Silicon wafer single side polished	Si-Mat, Kaufering

10.3 Instrumentation

Nuclear Magnetic Resonance (NMR) Spectroscopy: NMR spectra were recorded using Avance 250 MHz spectrometer from Bruker. Samples were prepared by dissolving in $CDCl_3$ with the concentration of 20 mg/ml.

Gel Permeation Chromatography (GPC): Molecular weights and molecular weight distributions of copolymer was determined using GPC (model Agilent 1100 series) from polymer standard service (PSS). Polystyrene or poly(methyl methacrylate) standard with the concentration between 1-3 mg/ml in Dimethylformamide or Tetrahydrofuran was applied with the flow rate of 1 ml/min.

Dip Coater: Samples were dip coated using tensile testing machine Zwick Z 2.5 (Zwick GmbH, Germany) with the withdrawal speed of 100 mm/min.

UV Crosslinker: Polymers were irradiated with a UV stratalinker 2400 from Stratagene at λ = 365 nm (I = 2.4 mW/cm^2).

UV-LED Lamp: Polymers were irradiated with a UV-LED lamp at λ = 365 nm from Opsytec Dr. Gröbel GmbH, in which the power can be adjusted from 5% - 100%.

Profilometer: The thickness of polymer film thicker than 10 µm was measured by using profilometer, Dektak 150 from Veeco. The stylus radius was 12.5 µm with 10 mg force. The scan length and duration were 900 µm and 50 sec, respectively.

CSM Nanoscratch/Nano-indenter: The friction force was measured on a CSM NanoScratch Setup by Anton Paar using Scratch 7.1.11 software with a plano-convex N-K7 KPX025 with 6.35 mm diameter glass lens of a radius 25.94 mm from Edmund Optics and coated with the identical polymer. The substrate was moved under the slider at different speeds and normal forces. The samples were scanned on a length of at least 2 mm at different sliding velocities and normal forces. The data acquisition rate was 100 Hz. The mean COF was determined by dividing the measured tangential force and the applied normal force. The first 0.5 mm of the measurement was ignored to avoid any influence of static friction. The swelling factor was measured on the same device using an uncoated glass lens as the opposing surface. Therefore, the dry film was brought in contact with the glass lens at a normal force of 3 mN. The vertical deflection of the cantilever was measured after the addition of deionized water as a function of time until no further swelling was observed.

Atomic force microscopy: The elastic modulus and adhesion of the surface-attached polymer networks in the swollen state were measured using a JPK Nanowizard4 equipped with a CP-CONT-PS-A cantilever by NanoandMore with a polystyrene sphere with 1.98 µm radius at the tip. Measurements were performed in deionized water. The sample and the slider were immersed 30 minutes prior to the measurement to ensure that the hydrogel layer is in a fully swollen state during the tests. At least three measurements on different spots were performed by recording 64 points on an area of 100×100 μm^2. Elastic moduli were calculated by fitting the Hertz equation using JPKSPM data processing software. The height profiles for swelling experiments were recorded in AC mode (non-contact mode) using an ACL silicon cantilever purchased from AppNano in an image size of 100×20 µm and a resolution of 265×51 pixels.

Optical microscopy: The surface of the surface-attached hydrogel samples was investigated in the swollen state after friction measurements to ensure the absence of damages in the area of the friction measurement using an Olympus BX51 light microscope. The wrinkles at the surface of the surface-attached samples were observed using the optical microscope.

Doctor blade: To prepare the thick samples, MTV Messtechnik CX1 doctor blade was used as the coating technique due to its simplicity. Moreover, samples produced by the doctor blade are more homogeneous in comparison to the dip-coated samples. Polymer solution with 250 mg/ml concentration was prepared. The coating speed was set to 5 mm/s. The thickness of the polymer solution coating can be adjusted by tuning the gap between the doctor blade and the substrate.

10.4 Synthesis

10.4.1 Synthesis of Methacryloyloxybenzophenone (MABP)

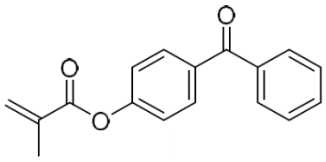

4-Hydroxybenzophenone (9.91 g, 0.05 mol) and triethylamine (5.7 g, 0.056 mol) were dissolved in dichloromethane (100 mL). The mixture was stirred in an ice bath for 1 h to cool the mixture to 0 °C prior to the dropwise addition of a solution of methacryloyl chloride (5.7 g, 0.055 mol) in dichloromethane (50 mL) over a period of 30 minute. The mixture is stirred overnight, filtrated and the residual product in the solid phase extracted with 25 ml of dichloromethane. The combined organic phase was washed with hydrochloric acid (3×150 mL, 0.1 M), deionized water (150 mL) and with saturated sodium bicarbonate solution (150 mL) and finally again with deionized water (3×150 mL). The organic phase was dried over sodium sulfate overnight and the solvent evaporated till a residual volume of around 20 ml remained. The solution was mixed with n-hexane in a ratio of 1:4 and stored in a freezer at -20 °C overnight. The solid was filtrated and dried in high vacuum at 40 °C for five hours to constant weight. The synthesis and the NMR spectroscopy were done by Natalia Schatz.

Yield: 9.42 g

^{1}H-NMR ($CDCl_3$): δ (ppm) = 2.11 (s, 3H, -CH_3), 5.83 (s, 1H, CH_2=C-), 6.42 (s, 1H, CH_2=C-), 7.27-7.92 (m, 9H, $CH_{arom.}$).

10.4.2 Polymer synthesis of P(DMAA)

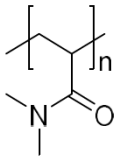

N,N-dimethylacrylamide (12.4 mL, 0.12 mol) and azobis(isobutyronitril) (19.7 mg, 0.12 mmol) were dissolved in dimethylformamide (60 mL). The solution was freeze-thawed three times. The solution was heated over night at 60°C. The polymer was precipitated in diethylether (900 mL). The solid is filtrated and dried under vacuum. The solid was dissolved in chloroform (1 g polymer/5 mL methanol). The polymer was precipitated in diethylether(900 mL). This procedure was repeated twice. The product was dried under vacuum. The whole synthesis procedure and the NMR spectroscopy were carried out by Natalia Schatz.

Yield: 8.75 g

^{1}H-NMR ($CDCl_3$): δ (ppm) = 2.90 (m, 6H, CH_3), 2.63 (m, 1H, -CH-), 1.62-1.28 (m, 2H, -CH_2-)

10.4.3 Synthesis of PDMAA-co-MABP

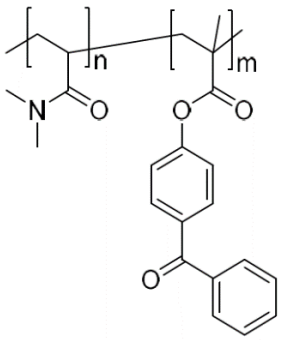

A 100 ml Schlenk tube was dried in vacuum and filled with 9.91 g (0.10 mol) of dimethylacrylamide, 14.0 mg (0.08 mmol) of AIBN and 20 ml of MeOH. The feeding content of MABP differed from 1% to 10% with the respect to dimethylacryamides. Then the schlenk tube was closed carefully and degassed under nitrogen through three freeze and thaw cycles. Polymerization was carried out at 60 °C overnight in a water bath. After completion of polymerization the polymer was precipitated in diethyl ether and repeated for three times.

10.4.4 Synthesis of 4-[3-(triethoxy silyl)propyloxy]benzophenone (Bp-Si)

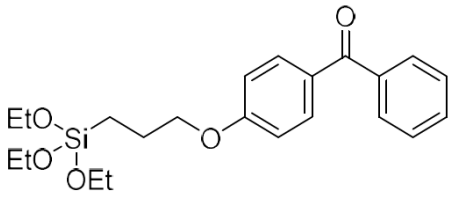

Bp-Si was used to functionalize glass or silicon wafer substrates to create C-H groups on the surface for further CHic reaction. The synthesis of Bp-Si consisted of two steps. In the first step, 4-allyloxybenzophenone was synthesized via Williamson ether synthesis reaction. In a single-necked flask with reflux condenser, 19.8 g (0.1 mol) of 4-hydroxybenzophenone and 13.3 g (0.11 mol) of allylbromide were dissolved in 30 ml anhydrous acetone and 14 g of potassium carbonate was added. The mixture was refluxed for 3 h. After cooling down to room temperature, 50 ml of water was added to the mixture. The resulting solution was extracted with 100 ml of diethylether. The combined ether phases were then washed with dilute NaOH solution (10%). The organic phase was dried over Na_2SO_4, filtered off, and the solvent was removed using a rotary evaporator. Then, it was recrystallized from methanol and used in the next step.

In the second step, 50 mg Pt-C (10% Pt) as a catalyst and 5 g of 4-allyloxybenzophenone were added to 25 ml freshly distilled triethoxysilane. The mixture was refluxed at 60 °C for one hour, and then it was continue refluxed at 120 °C overnight. The mixture was distilled under vacuum at 180 °C to remove excess triethoxysilane and dried under vacuum overnight. Finally, it was diluted in dry toluene and stored in the dark. The synthesis and the NMR spectroscopy of this product were performed by Natalia Schatz.

^{1}H-NMR ($CDCl_3$): δ (ppm) = 0.9 (m, 2H, $SiCH_2$), 1.25 (m, 9H, CH_3), 1.9 (m, 2H, O-CH_2-CH_2-CH_2-Si), 3.9 (m, 8H, OCH_2), 6.9-7.9 (various m, 9H, C-H_{arom}).

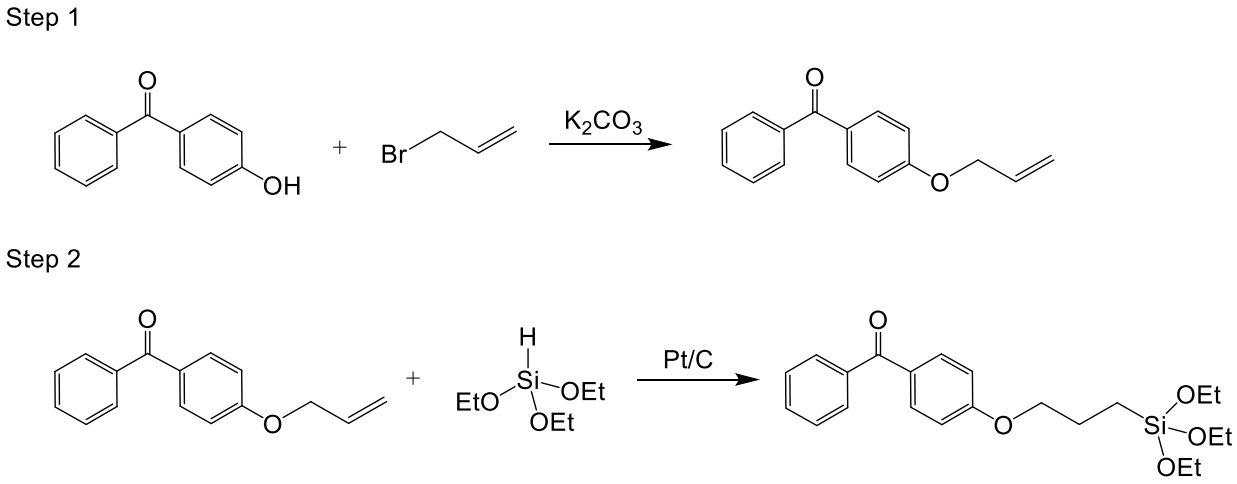

Figure 10-1 Synthesis of 4-[3-(triethoxysilyl)propyloxy]benzophenone (Bp-Si)

10.5 Preparation of surface-attached polymer network samples

10.5.1 Functionalization of glass substrates

In order to produce polymer layers that are chemically bonded to a substrate, the glass substrate has to functionalize. First, the glass microscope slides from Duran Company were thoroughly rinsed with ethanol and dried with dry nitrogen. The slides were functionalized with a monolayer of 3 triethoxy benzophenone silane via dip coating. The substrates were therefore dipped in a 50 mM solution diluted in toluene using a Zwick material testing BZ2.5/TN1S tensile tester and withdrawn from the solution at a rate of 100 mm/min. The substrates were annealed on a hot plate and kept at 120 °C for 30 min before coating the substrates with the desired polymer layer.

10.5.2 Preparation of surface-attached hydrogel networks

The functionalized glass substrates were coated by the polymer solution either by dip coating or by the doctor blade. The maximum concentration used for dip coating was 100 mg/ml, as higher concentrations result in rather inhomogeneous thickness. With the doctor blade, it was possible to use higher concentrations of 200 mg/ml. In both coating methods, the coating had to be done several times to reach the desired thicknesses. The films were dried in between the coating steps under ambient conditions. The slides were subsequently crosslinked in a Stratagene UV Stratalinker 240 UV-chamber at a wavelength of 365 nm for 90 min each from top and bottom at a cumulative intensity of around two times 12 J/cm^2. Subsequently, the

films were immersed in methanol for 24 hours to extract not covalently attached polymer chains from the network. Lenses were coated via dip coating (100 mm/min) using 50 mg/ml polymer solutions.

10.5.3 Bulk sample preparation

Bulk samples for swelling pressure and permeability tests were prepared by pouring a viscous polymer solution (300 mg/ml) to a Teflon mold. Then the samples were kept overnight to let the solvent evaporate. Next, the samples were crosslinked with a Stratagene UV Stratalinker 240 UV-chamber at a wavelength of 365 nm. Before performing the tests, the samples were kept in deionized water for 24 hours. Subsequently, the samples were cut in the desired size for the test.

10.5.4 Fabrication of the microstructured Si Wafer

The master silicon wafers were fabricated by the cleanroom service of the University of Freiburg. The steps followed for this process are briefly explained here.
Silicon wafers were prebaked at 100°C for thirty minutes. After slow colling down to the room temperature, the wafers were spin-coated with AZ-1518 photoresist (MicroChemicals) for 5 s at 800 rpm and 30 s at 4000 rpm to get a thickness of 0.5-1.8 µm. Afterwards, the photoresist was illuminated with UV light (λ = 365 nm, P = 6.5 mW) through a foil mask (Koenen GmbH). The uncrosslinked resist was removed by rinsing the wafer in an AZ-1518 developer (MicroChemicals) for 20 s. Silicon wafers coated with the patterned photoresist were etched according to the ″Process C″ protocol, where etching and passivation occur simultaneously.

10.5.5 Fabrication of PDMS replicas

The PDMS elastomer was mixed with a curing agent in a ratio of 10:1. The solution was poured over the etched Si wafer into an aluminum dish. The solution was kept under vacuum for an hour to remove the bubbles from the solution. The PDMS was heated at 80°C for 24 h. The PDMS was peeled off the Si wafer and cut out.

11 References

[1] Maugis D. Contact, adhesion and rupture of elastic solids. vol. 130. Springer Science & Business Media; 2013.

[2] Johnson K. Contact Mechanics, Cambridge University Press, Cambridge, UK 1985.

[3] Ferry JD. Viscoelastic properties of polymers. New York: Wiley; 1980.

[4] Heepe L, Gorb SN. Biologically Inspired Mushroom-Shaped Adhesive Microstructures. Annu Rev Mater Res 2014;44:173–203. doi:10.1146/annurev-matsci-062910-100458.

[5] Liskiewicz T, Morina A, Neville A. Friction in nature. WIT Trans Ecol Environ 2008;114:263–72. doi:10.2495/DN080271.

[6] Gorb SN, Koch K. From sticky to slippery: Biological and biologically-inspired adhesion and friction. Beilstein J Nanotechnol 2014;5:1450–1. doi:10.3762/bjnano.5.157.

[7] Bohn HF, Federle W. Insect aquaplaning: Nepenthes pitcher plants capture prey with the peristome, a fully wettable water-lubricated anisotropic surface. Proc Natl Acad Sci 2004;101:14138–43. doi:10.1073/pnas.0405885101.

[8] Prüm B, Florian Bohn H, Seidel R, Rubach S, Speck T. Plant surfaces with cuticular folds and their replicas: Influence of microstructuring and surface chemistry on the attachment of a leaf beetle. Acta Biomater 2013;9:6360–8. doi:10.1016/j.actbio.2013.01.030.

[9] Autumn K, Liang YA, Hsieh ST, Zesch W, Chan WP, Kenny TW, et al. Adhesive force of a single gecko foot-hair. Nature 2000;405:681–5. doi:10.1038/35015073.

[10] Manoonpong P, Petersen D, Kovalev A, Wörgötter F, Gorb SN, Spinner M, et al. Enhanced Locomotion Efficiency of a Bio-inspired Walking Robot using Contact Surfaces with Frictional Anisotropy. Sci Rep 2016;6:1–11. doi:10.1038/srep39455.

[11] Mow VC, Ateshian GA, Spilker RL. Biomechanics of Diarthrodial Joints: A Review of Twenty Years of Progress. J Biomech Eng 1993;115:460–7. doi:10.1115/1.2895525.

[12] Dai ZD, Wang WB, Zhang H, Yu M, Ji AH, Tan H, et al. Biomimetics on gecko locomotion. WIT Trans Ecol Environ 2008;114:23–32. doi:10.2495/DN080031.

[13] Oeffner J, Lauder G V. The hydrodynamic function of shark skin and two biomimetic applications. J Exp Biol 2012;215:785–95. doi:10.1242/jeb.063040.

[14] Jin Z, Dowson D. Bio-friction. Friction 2013;1:100–13. doi:10.1007/s40544-013-0004-4.

[15] Hsu S, Ying C, Zhao F. The nature of friction: A critical assessment. Friction 2014;2:1–26. doi:10.1007/s40544-013-0033-z.

[16] Silverman HG, Roberto FF. Understanding marine mussel adhesion. Mar Biotechnol

2007;9:661–81. doi:10.1007/s10126-007-9053-x.

[17] Sun J, Bhushan B. Structure and mechanical properties of beetle wings: A review. RSC Adv 2012;2:12606–23. doi:10.1039/c2ra21276e.

[18] Ditsche P, Summers A. Learning from Northern clingfish (Gobiesox maeandricus): Bioinspired suction cups attach to rough surfaces. Philos Trans R Soc B Biol Sci 2019;374. doi:10.1098/rstb.2019.0204.

[19] Wainwright DK, Kleinteich T, Kleinteich A, Gorb SN, Summers AP. Stick tight: Suction adhesion on irregular surfaces in the northern clingfish. Biol Lett 2013;9. doi:10.1098/rsbl.2013.0234.

[20] Jagota A, Hui CY. Adhesion, friction, and compliance of bio-mimetic and bio-inspired structured interfaces. Mater Sci Eng Reports 2011;72:253–92. doi:10.1016/j.mser.2011.08.001.

[21] Malik IA, Mirkhalaf M, Barthelat F. Bio-inspired "jigsaw"-like interlocking sutures: Modeling, optimization, 3D printing and testing. J Mech Phys Solids 2017;102:224–38. doi:10.1016/j.jmps.2017.03.003.

[22] Bhushan B, Sayer RA. Surface characterization and friction of a bio-inspired reversible adhesive tape. Microsyst Technol 2007;13:71–8. doi:10.1007/s00542-006-0256-2.

[23] Klein J. Molecular mechanisms of synovial joint lubrication. Proc Inst Mech Eng Part J J Eng Tribol 2006;220:691–710. doi:10.1243/13506501JET143.

[24] Wang M. Biolubricants and Biolubrication. Doctoral thesis 2014. KTH Royal Institute of Technology.

[25] Abdel-Aal HA. On surface structure and friction regulation in reptilian limbless locomotion. J Mech Behav Biomed Mater 2013;22:115–35. doi:10.1016/j.jmbbm.2012.09.014.

[26] Baum MJ, Heepe L, Gorb SN. Friction behavior of a microstructured polymer surface inspired by snake skin. Beilstein J Nanotechnol 2014;5:83–97. doi:10.3762/bjnano.5.8.

[27] Dolan G. Bio-tribology of Plant Cell Walls : Measuring the interactive forces between cell wall components Grace Dolan The University of Queensland in 2017 2017.

[28] Wang Y. Tribological Behaviour, Mechanical Properties and Bio-interface Engineering of Bio-inspired Hydrogels. Sch Chem Eng 2018;MEng.

[29] McCutchen CW. The frictional properties of animal joints. Wear 1962;5:1–17. doi:https://doi.org/10.1016/0043-1648(62)90176-X.

[30] Neville A, Morina A, Liskiewicz T, Yan Y. Synovial joint lubrication - Does nature teach more effective engineering lubrication strategies? Proc Inst Mech Eng Part C J Mech Eng Sci 2007;221:1223–30. doi:10.1243/09544062JMES724.

[31] Marieb EN, Hoehn K. Human anatomy & physiology. 2019.

[32] Shepherd DET, Seedhom BB. Thickness of human articular cartilage in joints of the lower limb. Ann Rheum Dis 1999;58:27–34. doi:10.1136/ard.58.1.27.

[33] Sophia Fox AJ, Bedi A, Rodeo SA. The basic science of articular cartilage: Structure, composition, and function. Sports Health 2009;1:461–8. doi:10.1177/1941738109350438.

[34] Katta J, Jin Z, Ingham E, Fisher J. Biotribology of articular cartilage-A review of the recent advances. Med Eng Phys 2008;30:1349–63. doi:10.1016/j.medengphy.2008.09.004.

[35] Caligaris M, Ateshian GA. Effects of sustained interstitial fluid pressurization under migrating contact area and boundary lubrication by synovial fluid on cartilage friction. NIH Public Access 2009;16:1220–7. doi:10.1016/j.joca.2008.02.020.

[36] Murakami T, Sakai N, Yamaguchi T, Yarimitsu S, Nakashima K, Sawae Y, et al. Evaluation of a superior lubrication mechanism with biphasic hydrogels for artificial cartilage. Tribol Int 2015;89:19–26. doi:10.1016/j.triboint.2014.12.013.

[37] Murakami T, Yarimitsu S, Sakai N, Nakashima K, Yamaguchi T, Sawae Y. Importance of adaptive multimode lubrication mechanism in natural synovial joints. Tribol Int 2017;113:306–15. doi:10.1016/j.triboint.2016.12.052.

[38] Moore AC, Burris DL. An Analytical Model for Cartilage Contact Mechanics. Tribol Lubr Technol 2014;70:14+. doi:http://dx.doi.org/10.1177/2049463718796865.

[39] Moore AC, Schrader JL, Ulvila JJ, Burris DL. A review of methods to study hydration effects on cartilage friction. Tribol - Mater Surfaces Interfaces 2017;11:202–14. doi:10.1080/17515831.2017.1397329.

[40] Bonnevie ED, Baro V, Wang L, Burris DL. In-situ studies of cartilage microtribology: roles of speed and contact area. Tribol Lett 2011;41:83–95. doi:10.1007/s11249-010-9687-0.

[41] Klein J, Kumacheva E, Mahalu D, Perahia D, Fetters LJ. Reduction of frictional forces between solid surfaces bearing polymer brushes. Nature 1994;370:634–6. doi:10.1038/370634a0.

[42] Bhushan B. Introduction to Tribology, Second Edition. 2013. doi:10.1002/9781118403259.

[43] Blau PJ. Friction Science and Technology. 2008. doi:10.1201/9781420054101.

[44] Li K. Ultralow friction of confined thin films. Doctoral thesis, 2014. University of Freiburg.

[45] Persson BNJ, Albohr O, Tartaglino U, Volokitin AI, Tosatti E. On the nature of surface roughness with application to contact mechanics, sealing, rubber friction and adhesion. J Phys Condens Matter 2005;17. doi:10.1088/0953-8984/17/1/R01.

[46] Bowden F. P., Tabor D. The Friction and Lubrication of Solids. New York: Oxford Univ.

Press, doi:10.1126/science.113.2938.443-a.

[47] Moore F. The friction and lubrication of elastomers. Wear 1973;23:409. doi:10.1016/0043-1648(73)90027-6.

[48] Ludema KC, Tabor D. Friction and Viscoelastic Properties of Polymeric Solids. Rubber Chem Technol 1968;41:462–76. doi:10.5254/1.3547185.

[49] Arvanitaki A, Briscoe BJ, Adams MJ, Johnson SA. The Friction and Lubrication of elastomers. In: Dowson D, Taylor CM, Childs THC, Dalmaz G, editors. Lubr. Lubr., vol. 30, Elsevier; 1995, p. 503–11. doi:https://doi.org/10.1016/S0167-8922(08)70656-4.

[50] Moore DF. The friction and lubrication of elastomers. vol. 9. Pergamon; 1972.

[51] Shizhu W, Ping H. PRINCIPLES OF TRIBOLOGY PRINCIPLES OF TRIBOLOGY Library of Congress Cataloging-in-Publication Data. n.d.

[52] Stachowiak GW, Batchelor AW. Engineering tribology / Gwidon Stachowiak, Andrew W. Batchelor. Fourth edi. Elsevier Butterworth-Heinemann Amsterdam; 2014.

[53] Stribeck R, Burndy Library. Kugellager für beliebige Belastungen. Berlin: [Buchdruckerei A.W. Schade, Berlin N.]; 1901.

[54] Maru MM, Tanaka DK. Consideration of stribeck diagram parameters in the investigation on wear and friction behavior in lubricated sliding. J Brazilian Soc Mech Sci Eng 2007;29:55–62. doi:10.1590/s1678-58782007000100009.

[55] Woydt M, Wäsche R. The history of the Stribeck curve and ball bearing steels: The role of Adolf Martens. Wear 2010;268:1542–6. doi:10.1016/j.wear.2010.02.015.

[56] Bhushan B. Boundary Lubrication and Lubricants. Introd to Tribol 2013:501–23. doi:10.1002/9781118403259.ch9.

[57] Ma L, Luo J. Thin film lubrication in the past 20 years. Friction 2016;4:280–302. doi:10.1007/s40544-016-0135-5.

[58] Popov VL. Contact mechanics and friction. n.d. doi:DOI 10.1007/978-3-642-10803-7.

[59] Fischer-Cripps AC. Nanoindentation. Springer New York; 2011.

[60] Horn RG, Israelachvili JN, Pribac F. Measurement of the deformation and adhesion of solids in contact. J Colloid Interface Sci 1987;115:480–92. doi:https://doi.org/10.1016/0021-9797(87)90065-8.

[61] Lin DC. Robust Strategies for Automated AFM Force Curve Analysis — II : Adhesion-Influenced Indentation of Soft , Elastic Materials 2016;129. doi:10.1115/1.2800826.

[62] Maugis D. Contact, adhesion and rupture of elastic solids. vol. 130. Springer Science & Business Media; 2013.

[63] Leite FL, Bueno CC, Da Róz AL, Ziemath EC, Oliveira ON. Theoretical models for

surface forces and adhesion and their measurement using atomic force microscopy. vol. 13. 2012. doi:10.3390/ijms131012773.

[64] McKenna A. Mechanical Characterization of Photo-crosslinkable Hydrogels with AFM. Mount Holyoke College, n.d.

[65] Briscoe WH, Titmuss S, Tiberg F, Thomas RK, McGillivray DJ, Klein J. Boundary lubrication under water. Nature 2006;444:191–4. doi:10.1038/nature05196.

[66] Gaisinskaya A, Ma L, Silbert G, Sorkin R, Tairy O, Goldberg R, et al. Hydration lubrication: Exploring a new paradigm. Faraday Discuss 2012;156:217–33. doi:10.1039/c2fd00127f.

[67] Konradi R. Weak Polyacid Brushes: Synthesis, Swelling Behavior, Complex Formation and Micropatterning. Synthesis (Stuttg) 2005.

[68] Li A, Benetti EM, Tranchida D, Clasohm JN, Schönherr H, Spencer ND. Surface-grafted, covalently cross-linked hydrogel brushes with tunable interfacial and bulk properties. Macromolecules 2011;44:5344–51. doi:10.1021/ma2006443.

[69] M C, Wh B, Sp A, J K. Lubrication at physiological pressures by polyzwitterionic brushes. Science (80-) 2009;323:1698–701.

[70] Raviv U, Klein J. Fluidity of bound hydration layers. Science (80-) 2002;297:1540–3. doi:10.1126/science.1074481.

[71] Raviv U, Weizmann Institute of Science R, Giasson S, Kampf N, Gohy JF, Jerome R, et al. Lubrication by charged polymers. Nature 2003;425 n 6954:163–5.

[72] Singh MK, Kang C, Ilg P, Crockett R, Kröger M, Spencer ND. Combined Experimental and Simulation Studies of Cross-Linked Polymer Brushes under Shear. Macromolecules 2018;51:10174–83. doi:10.1021/acs.macromol.8b01363.

[73] Tadmor R, Janik J, Klein J, Fetters LJ. Sliding friction with polymer brushes. Phys Rev Lett 2003;91:2–5. doi:10.1103/PhysRevLett.91.115503.

[74] Tay SP. New strategies towards the next generation of skin-friendly artificial turf surfaces GENERATION OF SKIN-FRIENDLY ARTIFICIAL 2016.

[75] Wilkinson A, Chan H, Hall G. Universities of Leeds , Sheffield and York Contact address : J Comp Psychol 2007;121:412–8.

[76] Milner ST. Polymer Brushes. Science 1991;251:905–14. doi:10.1126/science.251.4996.905.

[77] Goicochea AG, Mayoral E, Klapp J, Pastorino C. Nanotribology of biopolymer brushes in aqueous solution using dissipative particle dynamics simulations: an application to PEG covered liposomes in a theta solvent. Soft Matter 2014;10:166–74. doi:10.1039/C3SM52486H.

[78] Klein J, Raviv U, Perkin S, Kampf N, Chai L, Giasson S. Fluidity of water and of

hydrated ions confined between solid surfaces to molecularly thin films. J Phys Condens Matter 2004;16. doi:10.1088/0953-8984/16/45/008.

[79] Doi M. Gel dynamics. J Phys Soc Japan 2009;78:1–19. doi:10.1143/JPSJ.78.052001.

[80] Okay O. Hydrogel Sensors and Actuators 2010;6:1–15. doi:10.1007/978-3-540-75645-3.

[81] Yang T. Mechanical and Swelling properties of Hydrogels. Doctoral thesis, 2012. University of Freiburg

[82] Gong JP. Friction and lubrication of hydrogels - Its richness and complexity. Soft Matter 2006;2:544–52. doi:10.1039/b603209p.

[83] Freeman ME, Furey MJ, Love BJ, Hampton JM. Friction , wear , and lubrication of hydrogels as synthetic articular cartilage 2000:129–35.

[84] Moore JS, Bauer JM, Yu Q, Liu RH, Devadoss C, Jo B. Functional hydrogel structures for autonomous flow control inside micro fluidic channels. Nature 2000;404.

[85] Ma R, Xiong D, Miao F, Zhang J, Peng Y. Novel PVP / PVA hydrogels for articular cartilage replacement. Mater Sci Eng C 2009;29:1979–83. doi:10.1016/j.msec.2009.03.010.

[86] Milner PE, Parkes M, Puetzer JL, Chapman R, Stevens MM, Cann P, et al. Acta Biomaterialia A low friction , biphasic and boundary lubricating hydrogel for cartilage replacement. Acta Biomater 2018;65:102–11. doi:10.1016/j.actbio.2017.11.002.

[87] Press AIN. An elastic material for cartilage replacement in an arthritic shoulder joint 2006;27:1534–41. doi:10.1016/j.biomaterials. 2005.08.032.

[88] Dunn AC, Sawyer WG, Angelini TE. Gemini interfaces in aqueous lubrication with hydrogels. Tribol Lett 2014;54:59–66. doi:10.1007/s11249-014-0308-1.

[89] Urueña JM, Pitenis AA, Nixon RM, Schulze KD, Angelini TE, Gregory Sawyer W. Mesh Size Control of Polymer Fluctuation Lubrication in Gemini Hydrogels. Biotribology 2015;1–2:24–9. doi:10.1016/j.biotri.2015.03.001.

[90] Dunn AC, Cobb ÆJA, Kantzios ÆAN, Jin ÆS, Sarntinoranont M, Gregory ÆRTÆW. Friction Coefficient Measurement of Hydrogel Materials on Living Epithelial Cells 2008:13–9. doi:10.1007/s11249-008-9306-5.

[91] Vincent J. Basic Elasticity and Viscoelasticity. Struct Biomater 2019:1–28. doi:10.2307/j.ctt7tbgv.4.

[92] Courtney TH. Mechanical behavior of materials. New York: McGraw-Hill; 1990.

[93] McGhee EO, Pitenis AA, Urueña JM, Schulze KD, McGhee AJ, O'Bryan CS, et al. In Situ Measurements of Contact Dynamics in Speed-dependent Hydrogel Friction. Biotribology 2018;13:23–9. doi:10.1016/j.biotri.2017.12.002.

[94] Gutierrez-Lemini D. Engineering viscoelasticity. Eng Viscoelasticity 2014:1–353. doi:10.1007/978-1-4614-8139-3.

[95] Hu Y, Suo Z. Viscoelasticity and Poroelasticity in. Acta Mech Solida Sin 2012;25:441–58. doi:10.1016/S0894-9166(12)60039-1.

[96] Gutierrez-Lemini D. Engineering viscoelasticity. Eng Viscoelasticity 2014:1–353. doi:10.1007/978-1-4614-8139-3.

[97] Kalcioglu ZI, Mahmoodian R, Hu Y, Suo Z, Van Vliet KJ. From macro- to microscale poroelastic characterization of polymeric hydrogels via indentation. Soft Matter 2012;8:3393–8. doi:10.1039/c2sm06825g.

[98] Persson BNJ. Contact mechanics for poroelastic, fluid-filled media, with application to cartilage. J Chem Phys 2016;145. doi:10.1063/1.4972067.

[99] Mow VC, Kuei SC, Lai WM, Armstrong CG. Biphasic Creep and Stress Relaxation of Articular Cartilage in Compression: Theory and Experiments. J Biomech Eng 1980;102:73–84.

[100] Gong J, Osada Y. Gel friction: A model based on surface repulsion and adsorption. J Chem Phys 1998;109:8062–8. doi:10.1063/1.477453.

[101] Gong JP, Osada Y. Surface friction of polymer gels 2002;27.

[102] Spencer ND. Aqueous lubrication: natural and biomimetic approaches. Singapore: World Scientific; 2014.

[103] Tominaga T, Takedomi N, Biederman H, Furukawa H, Osada Y, Gong JP. Effect of substrate adhesion and hydrophobicity on hydrogel friction. Soft Matter 2008;4:1033–40. doi:10.1039/b716465c.

[104] Dunn AC, Pitenis AA, Urueña JM, Schulze KD, Angelini TE, Sawyer WG. Kinetics of aqueous lubrication in the hydrophilic hydrogel Gemini interface. Proc Inst Mech Eng Part H J Eng Med 2015;229:889–94. doi:10.1177/0954411915612819.

[105] Pitenis AA, Manuel Urueña J, Cooper AC, Angelini TE, Gregory Sawyer W. Superlubricity in Gemini Hydrogels. J Tribol 2016;138:042103. doi:10.1115/1.4032890.

[106] Wang L, Zhou Q, Zheng Y, Xu S. Composite structure and properties of the pitcher surface of the carnivorous plant Nepenthes and its influence on the insect attachment system. Prog Nat Sci 2009;19:1657–64. doi:10.1016/j.pnsc.2009.09.005.

[107] Shekhawat VK, Laurent MP, Muehleman C, Wimmer MA. Surface topography of viable articular cartilage measured with scanning white light interferometry. Osteoarthr Cartil 2009;17:1197–203. doi:10.1016/j.joca.2009.03.013.

[108] Yashima S, Takase N, Kurokawa T, Gong JP. Friction of hydrogels with controlled surface roughness on solid flat substrates. Soft Matter 2014;10:3192–9. doi:10.1039/c3sm52883a.

[109] Nemani SK, Annavarapu RK, Mohammadian B, Raiyan A, Heil J, Haque MA, et al. Surface Modification of Polymers: Methods and Applications. Adv Mater Interfaces 2018;5:1–26. doi:10.1002/admi.201801247.

[110] Prucker O, Naumann CA, Rhe J, Knoll W, Frank CW. Photochemical Attachment of Polymer Films to Solid Surfaces via Monolayers of Benzophenone Derivatives Photochemical Attachment of Polymer Films to Solid Surfaces via Monolayers of Benzophenone Derivatives 1999:8766–70. doi:10.1021/ja990962.

[111] Prucker O, Brandstetter T, Rühe J. Surface-attached hydrogel coatings via C,H-insertion crosslinking for biomedical and bioanalytical applications (Review). Biointerphases 2018;13:010801. doi:10.1116/1.4999786.

[112] Pérez-Perrino M, Navarro R, Prucker O, Rühe J. Binding of functionalized polymers to surface-attached polymer networks containing reactive groups. Macromolecules 2014;47:2695–702. doi:10.1021/ma500282b.

[113] Li K, Pandiyarajan CK, Prucker O, Rühe J. On the Lubrication Mechanism of Surfaces Covered with Surface-Attached Hydrogels. Macromol Chem Phys 2016;217:526–36. doi:10.1002/macp.201500243.

[114] Toomey R, Freidank D, Rühe J. Swelling behavior of thin, surface-attached polymer networks. Macromolecules 2004;37:882–7. doi:10.1021/ma034737v.

[115] Chen WL, Menzel M, Watanabe T, Prucker O, Rühe J, Ober CK. Reduced Lateral Confinement and Its Effect on Stability in Patterned Strong Polyelectrolyte Brushes. Langmuir 2017;33:3296–303. doi:10.1021/acs.langmuir.7b00165.

[116] Pitenis AA, Urueña JM, Schulze KD, Nixon RM, Dunn AC, Krick BA, et al. Polymer fluctuation lubrication in hydrogel gemini interfaces. Soft Matter 2014;10:8955–62. doi:10.1039/c4sm01728e.

[117] Kim J, Dunn AC. Soft hydrated sliding interfaces as complex fluids. Soft Matter 2016;12:6536–46. doi:10.1039/c6sm00623j.

[118] Gong J, Iwasaki Y, Osada Y, Kurihara K, Hamai Y. Friction of Gels. 3. Friction on Solid Surfaces. J Phys Chem B 1999;103:6001–6. doi:10.1021/jp9902553.

[119] Pan YS, Xiong DS, Ma RY. A study on the friction properties of poly(vinyl alcohol) hydrogel as articular cartilage against titanium alloy. Wear 2007;262:1021–5. doi:10.1016/j.wear.2006.10.005.

[120] Pitenis AA, Manuel Urueña J, Nixon RM, Bhattacharjee T, Krick BA, Dunn AC, et al. Lubricity from Entangled Polymer Networks on Hydrogels. J Tribol 2016;138:042102. doi:10.1115/1.4032889.

[121] Reale ER, Dunn AC. Poroelasticity-driven lubrication in hydrogel interfaces. Soft Matter 2017;13:428–35. doi:10.1039/c6sm02111e.

[122] Ishikawa Y, Hiratsuka K ichi, Sasada T. Role of water in the lubrication of hydrogel. Wear 2006;261:500–4. doi:10.1016/j.wear.2005.12.001.

[123] Yamamoto T, Kurokawa T, Ahmed J, Kamita G, Yashima S, Furukawa Y, et al. In situ observation of a hydrogel-glass interface during sliding friction. Soft Matter 2014;10:5589–96. doi:10.1039/c4sm00338a.

[124] Delavoipière J, Tran Y, Verneuil E, Heurtefeu B, Hui CY, Chateauminois A. Friction of Poroelastic Contacts with Thin Hydrogel Films. Langmuir 2018;34:9617–26. doi:10.1021/acs.langmuir.8b01466.

[125] Zhou Y, Zhu H, Zhang W, Zuo X, Li Y, Yang J. Influence of surface roughness on the friction property of textured surface. Adv Mech Eng 2015;7:1–9. doi:10.1177/1687814014568500.

[126] Chen W, Amann T, Kailer A, Rühe J. Thin-Film Lubrication in the Water/Octyl β- D -Glucopyranoside System: Macroscopic and Nanoscopic Tribological Behavior. Langmuir 2019;35:7136–45. doi:10.1021/acs.langmuir.9b00383.

[127] Alsadat S, Sahneh A. Phase Transition Behavior and Application of Novel Surface-attached Thermo-responsive Polymer Films Dissertation 2016.

[128] Pandiyarajan CK, Prucker O, Zieger B, Rühe J. Influence of the Molecular Structure of Surface-Attached Poly(N-alkyl Acrylamide) Coatings on the Interaction of Surfaces with Proteins, Cells and Blood Platelets. Macromol Biosci 2013;13:873–84. doi:10.1002/mabi.201200445.

[129] Bouklas N, Huang R. Swelling kinetics of polymer gels: Comparison of linear and nonlinear theories. Soft Matter 2012;8:8194–203. doi:10.1039/c2sm25467k.

[130] Chapter 6 Solid-fluid mixtures and hydrogels ;63:63–72. University of Colorado.

[131] De Kee D, Liu Q, Hinestroza J. Viscoelastic (Non-Fickian) Diffusion. Can J Chem Eng 2008;83:913–29. doi:10.1002/cjce.5450830601.

[132] Zhao Z, Gu J, Zhao Y, Guan Y, Zhu XX, Zhang Y. Hydrogel thin film with swelling-induced wrinkling patterns for high-throughput generation of multicellular spheroids. Biomacromolecules 2014;15:3306–12. doi:10.1021/bm500722g.

[133] Weiss F, Cai S, Hu Y, Kyoo Kang M, Huang R, Suo Z. Creases and wrinkles on the surface of a swollen gel. J Appl Phys 2013;114. doi:10.1063/1.4818943.

[134] Wu Z, Bouklas N, Huang R. Swell-induced surface instability of hydrogel layers with material properties varying in thickness direction. Int J Solids Struct 2013;50:578–87. doi:10.1016/j.ijsolstr.2012.10.022.

[135] Liu Z, Swaddiwudhipong S, Hong W. Pattern formation in plants via instability theory of hydrogels. Soft Matter 2013;9:577–87. doi:10.1039/c2sm26642c.

[136] Schweikart A, Fery A. Controlled wrinkling as a novel method for the fabrication of patterned surfaces. Microchim Acta 2009;165:249–63. doi:10.1007/s00604-009-0153-3.

[137] Jpk. Tech12 / 04 - A practical guide to AFM force spectroscopy and data analysis. JPK Notes 2008;1:1–8.

[138] Wriggers P. Introduction to Contact Mechanics. 2006. doi:10.1007/978-3-540-32609-02.

[139] Dimitriadis EK, Horkay F, Maresca J, Kachar B, Chadwick RS. Determination of elastic moduli of thin layers of soft material using the atomic force microscope. Biophys J 2002;82:2798–810. doi:10.1016/S0006-3495(02)75620-8.

[140] Gennes P-G de. Scaling concepts in polymer physics. Ithaca, NY, NY: Cornell Univ. Press; 2005.

[141] Tsuji Y, Li X, Shibayama M. Evaluation of Mesh Size in Model Polymer Networks Consisting of Tetra-Arm and Linear Poly(ethylene glycol)s. Gels 2018;4:50. doi:10.3390/gels4020050.

[142] Gehrke SH, Fisher JP, Palasis M, Lund ME. Factors Determining Hydrogel Permeability. Ann N Y Acad Sci 2006;831:179–84. doi:10.1111/j.1749-6632.1997.tb52194.x.

[143] Fujiyabu T, Li X, Shibayama M, Chung U Il, Sakai T. Permeation of Water through Hydrogels with Controlled Network Structure. Macromolecules 2017;50:9411–6. doi:10.1021/acs.macromol.7b01807.

[144] Hu Y, Chan EP, Vlassak JJ, Suo Z. Poroelastic relaxation indentation of thin layers of gels. J Appl Phys 2011;110:108–11. doi:10.1063/1.3647758.

[145] Chan EP, Hu Y, Johnson PM, Suo Z, Stafford CM. Spherical indentation testing of poroelastic relaxations in thin hydrogel layers. Soft Matter 2012;8:1492–8. doi:10.1039/c1sm06514a.

[146] Munz M. Force calibration in lateral force microscopy: a review of the experimental methods. J Phys D Appl Phys 2010;43:063001. doi:10.1088/0022-3727/43/6/063001.

[147] Choi D, Hwang W. Measurement of frictional forces in atomic force microscopy. Solid State Phenom 2007;121–123:851–4. doi:10.4028/www.scientific.net/ssp.121-123.851.

[148] Li Q, Kim S, Rydberg A. Lateral force calibration of an atomic force microscope with a diamagnetic levitation spring system 2006;065105. doi:10.1063/1.2209953.

[149] Cannara RJ, Eglin M, Carpick RW. Lateral force calibration in atomic force microscopy : A new lateral force calibration method and general guidelines for optimization calibration method and general guidelines for optimization 2006;053701. doi:10.1063/1.2198768.

[150] Varenberg M, Etsion I, Halperin G. An improved wedge calibration method for lateral force in atomic force microscopy. Rev Sci Instrum 2003;74:3362–7. doi:10.1063/1.1584082.

[151] Wang H, Gee ML. AFM lateral force calibration for an integrated probe using a calibration grating. Ultramicroscopy 2014;136:193–200. doi:10.1016/j.ultramic.2013.10.012.

[152] Urueña JM, McGhee EO, Angelini TE, Dowson D, Sawyer WG, Pitenis AA. Normal load scaling of friction in gemini hydrogels. Biotribology 2018;13:30–5.

[153] Shoaib T, Heintz J, Lopez-berganza JA, Muro-barrios R, Egner SA, Espinosa-marzal RM. Stick − Slip Friction Reveals Hydrogel Lubrication Mechanisms 2018. doi:10.1021/acs.langmuir.7b02834.

[154] Israelachvili JN. Intermolecular and surface forces / Jacob N. Israelachvili. London ; San Diego: Academic Press; 1991.

[155] Falkovich G. Fluid Mechanics. Cambridge: Cambridge University Press; 2011. doi:10.1017/CBO9780511794353.

[156] Dunn AC, Urueña JM, Huo Y, Perry SS, Angelini TE, Sawyer WG. Lubricity of surface hydrogel layers. Tribol Lett 2013;49:371–8. doi:10.1007/s11249-012-0076-8.

[157] Ljubic D, Stamenovic M, Smithson C, Nujkic M, Medjo B, Putic S. Time: Temperature superposition principle: Application of WLF equation in polymer analysis and composites. Zast Mater 2014;55:395–400. doi:10.5937/zasmat1404395l.

[158] Baykal D, Underwood RJ, Mansmann K, Marcolongo M, Kurtz SM. Evaluation of friction properties of hydrogels based on a biphasic cartilage model 2013;28:263–73. doi:10.1016/j.jmbbm.2013.07.022.

[159] Moore AC, Burris DL. An analytical model to predict interstitial lubrication of cartilage in migrating contact areas. J Biomech 2014;47:148–53. doi:10.1016/j.jbiomech.2013.09.020.

[160] Hay J, Crawford B. Measuring substrate-independent modulus of thin films. J Mater Res 2011;26:727–38. doi:10.1557/jmr.2011.8.

[161] Bec S, Tonck A, Loubet JL. A simple guide to determine elastic properties of films on substrate from nanoindentation experiments. Philos Mag 2006;86:5347–58. doi:10.1080/14786430600660856.

[162] Division H, Mechanics AGAO, Stanford SC, Ca JINLEE. Elastic Contact Versus Indentation Modeling of Multi-Layered 1990.

[163] Rubinstein M, Colby RH. Polymer Physics Michael Rubinstein, Ralph H Colby-standand.pdf n.d. doi:10.1145/2024288.2024304.

[164] Fischer-Cripps AC. Nanoindentation / Anthony C. Fischer-Cripps. Springer New York; 2002.

[165] Fischer-Cripps AC. Introduction to contact mechanics / Anthony C. Fischer-Cripps. Springer New York; 2000.

[166] Briscoe BJ, Sebastian KS, Adams MJ. The effect of indenter geometry on the elastic response to indentation. J Phys D Appl Phys 1994;27:1156–62. doi:10.1088/0022-3727/27/6/013.

[167] Mak AF. The apparent viscoelastic behavior of articular cartilage--the contributions from the intrinsic matrix viscoelasticity and interstitial fluid flows. J Biomech Eng 1986;108:123–30.

[168] Hayes WC, Bodine AJ. Flow-independent viscoelastic properties of articular cartilage matrix. J Biomech 1978. doi:10.1016/0021-9290(78)90075-1.

[169] Schulze KD, Hart SM, Marshall SL, O'Bryan CS, Urueña JM, Pitenis AA, et al. Polymer Osmotic Pressure in Hydrogel Contact Mechanics. Biotribology 2017;11:3–7. doi:10.1016/j.biotri.2017.03.004.

[170] Peng Y, Serfass CM, Hill CN, Hsiao LC. Lubricated friction of textured soft substrates , Department of Chemical and Biomolecular Engineering, North Carolina State University, Raleigh, NC 27695.

[171] Pettersson U, Jacobson S. Textured surfaces in sliding boundary lubricated contacts – mechanisms, possibilities and limitations. Tribol - Mater Surfaces Interfaces 2007;1:181–9. doi:10.1179/175158308X300450.

[172] Golloch R, Merker GP, Kessen U, Brinkmann S. Functional properties of microstructured cylinder liner surfaces for internal combustion engines. Tribotest 2005;11:307–24. doi:10.1002/tt.3020110403.

[173] Goldberg R, Klein J. Liposomes as lubricants: Beyond drug delivery. Chem Phys Lipids 2012;165:374–81. doi:10.1016/j.chemphyslip.2011.11.007.

[174] Sorkin R, Dror Y, Kampf N, Klein J. Mechanical stability and lubrication by phosphatidylcholine boundary layers in the vesicular and in the extended lamellar phases. Langmuir 2014;30:5005–14. doi:10.1021/la500420u.

[175] Singer IL, Pollock HM. Fundamentals of friction : macroscopic and microscopic processes, 1992.

[176] Gao Y, Ma L, Luo J. Friction Anisotropy Induced by Oriented Liquid Crystal Molecules. Tribol Lett 2016;61:1–6. doi:10.1007/s11249-016-0645-3.

[177] Gao YF, Xue B, Ma L, Luo J. Effect of liquid crystal molecular orientation controlled by an electric field on friction, 2017.

[178] Raviv U, Giasson S, Kampf N, Gohy JF, Jérôme R, Klein J. Normal and frictional forces between surfaces bearing polyelectrolyte brushes. Langmuir 2008. doi:10.1021/la7039724.

Acknowledgment

First and foremost, I take this opportunity to express my gratitude to both my supervisors Prof. Dr. Jürgen Rühe and Prof. Dr. Vincent Le Houérou, who have supported me throughout my Ph.D. with their patience and guidance. I am thankful to both of them, as they gave me the opportunity to learn and try everything my way. Without their assistance and dedicated involvement in every step, this thesis would not have been completed. One could not wish for better and friendlier supervisors.

This work would not have been possible without the financial support of International Research Training Group (IRTG) “Soft Matter Science”.

I would like to thank Dr. Oswald Prucker and Dr. Thomas Brandstetter for their valuable and constructive suggestions. Their willingness to give their time so generously has been very much appreciated.

I would also like to thank Ms. Petra Wiloth, Ms. Olivia Fellinger, Ms. Jana Husse, and Ms. Birgitta Zovko for their kind assistance with administrative work.

I am particularly grateful for the assistance given by Ms. Natalia Schatz, Mr. Holger Frey, Mr. Martin Schönstein, Ms. Malwina Pajestka, and Mr. Alexander Dietz and the people from MinaMech platform (Damien Favier and Leandro Jacomine), who helped me in handling the instruments, chemicals, and synthesis.

I would like to express my deep gratitude to Sharareh Asiaee and Thananthorn Kanokwijitsilp (Maii), who helped me a lot in the lab at the beginning of my Ph.D..

I would also like to extend my thanks to my very kind and welcoming office mates (Sebastian Anders, Roland Höhnes, Jonas Kost and Mahboubeh Karger) for the enjoyable time we spent together.

I wish to thank Anil Rajak, Moritz Katzmaier and Muhammad Hafiz Noman, the master students, for their contributions to this project. Thanks to Wei Chen for her cooperation on the part of the project related to the combination of hydrogels and liquid lubricants.

I wish to acknowledge all my previous and present CPI colleagues who made CPI the best ever place to work. I may not experience such an amazing and friendly working group in my life. You guys are awesome! Thank you!

I would like to thank all who have indirectly helped me to bring out this dissertation. I would like to offer my special thanks to CPI girls (Britta, Carmen, Katrin, Maii, Sarah, Anna S., Hasti, Anna L., Dan, Nung, Freddy), Mensa group (Sharareh, Crispin, Maii, Zhuoling, Vania, Bidhari), Lunch group in Strasbourg (Charchit, Amparo, Rigoberto, Vishnu, Jean, Randy, Laure, Vaibhav), Lunch group in FIT (DanDan, Anna Piccola, My Maii, Nung, Mahboub), FIT crew (Stefan, Jonas, Patrick, Dennis, Anil, Paula, Dan) for the very fruitful discussions and extracurricular activities we did together. I enjoyed every moment I spent with you guys.

Nobody has been more important to me in the pursuit of my dreams than my family members. I would like to thank my parents, whose love and guidance are with me in whatever I pursue. They taught me throughout my life to follow what I have passion for. They are the ultimate role models. You have always encouraged me and appreciated me. I wish to thank my brothers (Mohsen and Mahdi), my partners in crime, for having my back and being my best friends.

Most importantly, I wish to thank my loving and supportive husband, Vahid, who always believes in me more than I do, and supports me through thick and thin.

Maryam Bahrami

Investigations on the lubrication mechanism of surface-attached hydrogels

Résumé

Les couches d'hydrogel covalentes sont obtenues par une réaction de réticulation par insertion de C-H durant laquelle l'irradiation UV entraîne une réticulation simultanée des chaînes polymères et la fixation du réseau au substrat. Dans ce travail, le comportement tribologique d'interfaces composées de deux couches d'hydrogels fixés en surface a été étudié sous des pressions et des vitesses de glissement relativement élevées. Des travaux récents sur la tribologie des hydrogels fixés en surface ont révélé que l'adhésion est négligeable entre ces couches, car l'interpénétration est prescrite pour des raisons entropiques. Nous avons proposé un modèle qui décrit le comportement en frottement de ces systèmes comme une somme de contributions à la force de frottement, et qui est fonction de plusieurs paramètres influents. En outre, nous avons étudié le rôle du confinement imposé par le substrat rigide sur la lubrification des hydrogels fixés en surface, car le coefficient de frottement extrêmement faible de ces couches semble être la conséquence de confinement élevé. Enfin, l'influence de la microstructure de surface et de l'ajout de tensioactifs sur le comportement en frottement des hydrogels fixés en surface ont été explorés.

Résumé en anglais

Covalently bonded hydrogel layers are generated by C-H insertion crosslinking in which subsequent UV irradiation leads to simultaneous crosslinking of the polymer chains and attachment of the network to the substrate. In this work, tribological behavior of surface-attached hydrogel pairs have been investigated under relatively high pressures and sliding velocities. Recent work on tribology of surface-attached hydrogels revealed that adhesion is a negligible term in such layers, as interpenetration between these layers are avoided due to entropic reasons. We proposed a model that gives insight into the influential parameters in determination of the frictional behavior by considering contribution of the different force components in the friction force. Furthermore, we studied the role of the confinement imposed by the stiff substrate on the lubrication of surface-attached hydrogels, as extremely low coefficient of friction of these layers appears to be the consequence of the high confinement. Finally, the influence of surface micro-structuring and surfactant addition on the frictional behavior of the surface-attached hydrogels was investigated.